Analysis And Design Of Dielectric Multilayers For High-Efficiency Optical Coatings

Roberta De Simone

UNIVERSITY OF SALERNO

DEPARTMENT OF INDUSTRIAL ENGINEERING

Ph.D. Course in Industrial Engineering
Curriculum in Electronic Engineering – XXXV Cycle

ANALYSIS AND DESIGN OF
DIELECTRIC MULTILAYERS FOR
HIGH-EFFICIENCY OPTICAL COATINGS

Supervisor
Prof. Francesco Chiadini

Ph.D. Student
Roberta De Simone

Scientific Referees
Prof. Vincenzo Fiumara
Prof. Vincenzo Pierro

Ph.D. Course Coordinator
Prof. Francesco Donsì

List of Publications

Abbott, R., ... and De Simone, R., *et al.* (LVK Collaboration) (2021*a*), 'All-sky search for continuous gravitational waves from isolated neutron stars in the early O3 LIGO data', *Physical Review D* **104**(8).

Abbott, R., ... and De Simone, R., *et al.* (LVK Collaboration) (2021*b*), 'All-sky search for long-duration gravitational-wave bursts in the third Advanced LIGO and Advanced Virgo run', *Physical Review D* **104**(10).

Abbott, R., ... and De Simone, R., *et al.* (LVK Collaboration) (2021*c*), 'All-sky search for short gravitational-wave bursts in the third Advanced LIGO and Advanced Virgo run', *Physical Review D* **104**(12).

Abbott, R., ... and De Simone, R., *et al.* (LVK Collaboration) (2021*d*), 'All-sky search in early O3 LIGO data for continuous gravitational-wave signals from unknown neutron stars in binary systems', *Physical Review D* **103**(6).

Abbott, R., ... and De Simone, R., *et al.* (LVK Collaboration) (2021*e*), 'Constraints from LIGO O3 Data on Gravitational-wave Emission Due to R-modes in the Glitching Pulsar PSR J0537-6910', *Astrophysical Journal* **922**(1).

Abbott, R., ... and De Simone, R., *et al.* (LVK Collaboration) (2021*f*), 'Constraints on Cosmic Strings Using Data from the Third Advanced LIGO-Virgo Observing Run', *Physical Review Letters* **126**(24).

Abbott, R., ... and De Simone, R., *et al.* (LVK Collaboration) (2021*g*), 'Diving below the Spin-down Limit: Constraints on Gravitational Waves from the Energetic Young Pulsar PSR J0537-6910', *Astrophysical Journal Letters* **913**(2).

Abbott, R., ... and De Simone, R., *et al.* (LVK Collaboration) (2021*h*), 'Observation of Gravitational Waves from Two Neutron Star-Black Hole Coalescences', *Astrophysical Journal Letters* **915**(1).

Abbott, R., ... and De Simone, R., *et al.* (LVK Collaboration) (2021*i*), 'Search for anisotropic gravitational-wave backgrounds using data from Advanced LIGO and Advanced Virgo's first three observing runs', *Physical Review D* **104**(2).

Abbott, R., ... and De Simone, R., *et al.* (LVK Collaboration) (2021*j*), 'Searches for continuous gravitational waves from young supernova remnants in the early third observing run of advanced LIGO and Virgo', *Astrophysical Journal* **921**(1).

Abbott, R., ... and De Simone, R., *et al.* (LVK Collaboration) (2021*k*), 'Upper limits on the isotropic gravitational-wave background from Advanced LIGO and Advanced Virgo's third observing run', *Physical Review D* **104**(2).

Abbott, R., ... and De Simone, R., *et al.* (LVK Collaboration) (2022*a*), 'All-sky, all-frequency directional search for persistent gravitational waves from Advanced LIGO's and Advanced Virgo's first three observing runs', *Physical Review D* **105**(12).

Abbott, R., ... and De Simone, R., *et al.* (LVK Collaboration) (2022*b*), 'All-sky search for continuous gravitational waves from isolated neutron stars using Advanced LIGO and Advanced Virgo O3 data', *Physical Review D* **106**(10).

Abbott, R., ... and De Simone, R., *et al.* (LVK Collaboration) (2022*c*), 'All-sky search for gravitational wave emission from scalar boson clouds around spinning black holes in LIGO O3 data', *Physical Review D* **105**(10).

Abbott, R., ... and De Simone, R., *et al.* (LVK Collaboration) (2022*d*), 'Constraints on dark photon dark matter using data from LIGO's and Virgo's third observing run', *Physical Review D* **105**(6).

Abbott, R., ... and De Simone, R., *et al.* (LVK Collaboration) (2022*e*), 'First joint observation by the underground gravitational-wave detector KAGRA with GEO 600', *Progress of Theoretical and Experimental Physics* **2022**(6).

Abbott, R., ... and De Simone, R., *et al.* (LVK Collaboration) (2022*f*), 'Model-based Cross-correlation Search for Gravitational Waves from the Low-mass X-Ray Binary Scorpius X-1 in LIGO O3 Data', *Astrophysical Journal Letters* **941**(2).

Abbott, R., ... and De Simone, R., *et al.* (LVK Collaboration) (2022*g*), 'Narrowband Searches for Continuous and Long-duration Transient Gravitational Waves from Known Pulsars in the LIGO-Virgo Third Observing Run', *Astrophysical Journal* **932**(2).

Abbott, R., ... and De Simone, R., *et al.* (LVK Collaboration) (2022*h*), 'Search for continuous gravitational wave emission from the Milky Way center in O3 LIGO-Virgo data', *Physical Review D* **106**(4).

Abbott, R., ... and De Simone, R., *et al.* (LVK Collaboration) (2022*i*), 'Search for continuous gravitational waves from 20 accreting millisecond x-ray pulsars in O3 LIGO data', *Physical Review D* **105**(2).

Abbott, R., ... and De Simone, R., *et al.* (LVK Collaboration) (2022*j*), 'Search for gravitational waves from Scorpius X-1 with a hidden Markov model in O3 LIGO data', *Physical Review D* **106**(6).

Abbott, R., ... and De Simone, R., *et al.* (LVK Collaboration) (2022*k*), 'Search for intermediate-mass black hole binaries in the third observing run of Advanced LIGO and Advanced Virgo', *Astronomy and Astrophysics* **659**.

Abbott, R., ... and De Simone, R., *et al.* (LVK Collaboration) (2022*l*), 'Search for Subsolar-Mass Binaries in the First Half of Advanced LIGO's and Advanced Virgo's Third Observing Run', *Physical Review Letters* **129**(6).

Abbott, R., ... and De Simone, R., *et al.* (LVK Collaboration) (2022*m*), 'Search of the early O3 LIGO data for continuous gravitational waves from the Cassiopeia A and Vela Jr. supernova remnants', *Physical Review D* **105**(8).

Abbott, R., ... and De Simone, R., *et al.* (LVK Collaboration) (2022*n*), 'Searches for Gravitational Waves from Known Pulsars at Two Harmonics in the Second and Third LIGO-Virgo Observing Runs', *Astrophysical Journal* **935**(1).

Abbott, R., ... and De Simone, R., *et al.* (LVK Collaboration) (2023), 'Population of Merging Compact Binaries Inferred Using Gravitational Waves through GWTC-3', *Physical Review X* **13**(1).

Acernese, F., ... and De Simone, R., *et al.* (LVK Collaboration) (2021), 'Search for Lensing Signatures in the Gravitational-Wave Observations from the First Half of LIGO-Virgo's Third Observing Run', *The Astrophysical Journal* **923**(1), 1401–1424.

Acernese, F., ... and De Simone, R., *et al.* (LVK Collaboration) (2022*a*), 'Calibration of advanced Virgo and reconstruction of the detector strain h(t) during the observing run O3', *Classical and Quantum Gravity* **39**(4).

Acernese, F., ... and De Simone, R., *et al.* (LVK Collaboration) (2022*b*), 'Search for Gravitational Waves Associated with Gamma-Ray Bursts Detected by Fermi and Swift during the LIGO-Virgo Run O3b', *The Astrophysical Journal* **928**(2), 18601–18620.

Acernese, F., ... and De Simone, R., *et al.* (LVK Collaboration) (2022*c*), 'The Virgo O3 run and the impact of the environment', *Classical and Quantum Gravity* **39**(23).

Acernese, F., ... and De Simone, R., *et al.* (LVK Collaboration) (2023*a*), Advanced Virgo Plus: Future Perspectives, Vol. 2429.

Acernese, F., ... and De Simone, R., *et al.* (LVK Collaboration) (2023*b*), 'The Advanced Virgo+ status', *Journal of Physics: Conference Series* **2429**(1), 01203901–01203912.

Calloni, E., ... and De Simone, R., *et al.* (LVK Collaboration) (2021), 'High-bandwidth beam balance for vacuum-weight experiment and Newtonian noise subtraction', *European Physical Journal Plus* **136**(3).

Chiadini, F., De Simone, R., Fiumara, V. & Scaglione, A. (2019*a*), 'Fractal defected ground microstrips', *ICECOM 2019 - 23rd International Conference on Applied Electromagnetics and Communications, Proceedings* .

Chiadini, F., De Simone, R., Fiumara, V. & Scaglione, A. (2019*b*), 'Temperature Dependent Defect Modes at Terahertz Regime', *ICECOM 2019 - 23rd International Conference on Applied Electromagnetics and Communications, Proceedings* .

De Simone, R., Chiadini, F., Scaglione, A. & Fiumara, V. (2020), 'Temperature-mediated excitation of defect modes in a periodic structure at terahertz frequencies', *Microwave and Optical Technology Letters* **62**(12), 3677–3681.

Durante, O., ... and De Simone, R., *et al.* (2023), 'Role of oxygen vacancies in the structural phase transformations of granular tio2 thin films', *Surfaces and Interfaces* **37**.

Contents

List of Figures

List of Tables

Abstract

The past decade has seen the ramp-up of the second-generation ('Advanced') earth-based gravitational-wave (GW) detectors. Design improvements and technological upgrades have paved the way to the first direct detection of GWs by the global network made up of the two aLIGO instruments (LIGO Scientific Collaboration 2015) (located in the USA: Hanford, WA and Livingston, LA) and of the Advanced Virgo detector (Acernese, F. *et al.* 2015*a*) (located in Cascina, Italy). The main results achieved by the LIGO Scientific Collaboration and the Virgo Collaboration – recently joined by the KAGRA Collaboration (located in Kamioka, Japan, under the Ikenoue mountain) – include the first detection of a binary black hole merger (GW150914 (Abbott, R. *et al.* (LVK Collaboration) 2016)); the first detection of a binary neutron star (BNS) merger (GW170817 (Abbott, R. *et al.* (LVK Collaboration) 2017)) that lead to the birth of multi-messenger astronomy with GW (Hartley 2017); and now dozens of detections of compact binary mergers that add up in a GW Transient Catalogue regularly updated (Abbott, R. *et al.* (LVK Collaboration) 2019)-(Abbott, R., ... and De Simone, R., *et al.* (LVK Collaboration) 2021). These detections contribute to opening a new window onto the Universe by providing insights to the populations of compact objects and the binary merger rates (Abbott, R. *et al.* (LVK Collaboration) 2021*b*); they also allow scientists to perform stringent tests of general relativity (Abbott, R. *et al.* (LVK Collaboration) 2021*c*) in a new regime of gravitation never probed before. Advanced Virgo is a power-recycled Michelson interferometer with Fabry-Perot cavities in its 3 km-long arms. By measuring interferometric figure due to the length differences between mirrors in the arms interferometer, gravitational waves are identified. There-

fore, very sensitive interferometers that accurately measure the separation between suspended test masses coated to function as highly reflecting mirrors have been designed in order to detect gravitational waves. A core challenge is the optimization of the mirrors for GW detectors. It is important to discover a mirror configuration that produces the least amount of additional (thermal) noise on the detection channel in addition to the typical mirror optimization design request of achieving high reflectance in a given frequency and angular range. It is well known that high reflectance mirrors typically consist of multilayers of alternating low and high refractive index materials, where each layer is quarter wave thick at the operating frequency. As a result, a simple formulation of the coating optimization problem for the design of low noise dielectric mirrors can involve looking for the sequence of thicknesses of the selected materials that make up the mirrors that minimizes the thermal noise while maintaining the transmittance below a specified threshold value. To improve the multilayers structures performance, it has been formulated and solved another design that consist in discovering (synthesizing and optimizing) improved materials that have increased optical contrast, fewer optical and mechanical losses and enabling the achievement of a specified transmittance with fewer layers, resulting into thinner coatings and lower noise and giving up the constraint of having only two constituent materials and, then, introducing new ternary multimaterial design. A check of the robustness against the inaccuracy of the deposition process has been also carried out. Furthermore, none of the materials present in nature and studied at this time qualifies as a straight substitute for the materials currently in use with the highest optical losses (TiO_2-doped Ta_2O_5 in current setups), but a few of them are better in terms of some properties (e.g., optical density, and/or mechanical losses), while unfortunately worse regarding others. The optimal material can be synthesized by using *Nanolayered structure* (NL) with thickness and equivalent refractive index that must be chosen ad hoc to fulfill the imposed conditions: at this scope it has been introduced a novelty homogenization procedure based on an established technique, the *Abelès method*. The technique proposed albeit presents some theoretical glitches has been verified that works well under

certain assumptions. In addition, this technique has the advantage of being easy to implement in a laboratory, with the drawback of being able to apply it to a single wavelength. We are now exploring an innovative approach in order to build a very sensitive detection scheme using differential interferometry able to carry out high precision measurements: Quadrature Differential Phase Interferometer.

Introduction and Motivation

The past decade has seen the ramp-up of the second-generation ('Advanced') earth-based gravitational-wave (GW) detectors. Design improvements and technological upgrades have paved the way to the first direct detection of GWs by the global network made up of the two aLIGO instruments (LIGO Scientific Collaboration 2015) (located in the USA: Hanford, WA and Livingston, LA) and of the Advanced Virgo detector (Acernese, F. *et al.* 2015*a*) (located in Cascina, Italy). The main results achieved by the LIGO Scientific Collaboration and the Virgo Collaboration – recently joined by the KAGRA Collaboration (located in Kamioka, Japan, under the Ikenoue mountain) – include the first detection of a binary black hole merger (GW150914 (Abbott, R. *et al.* (LVK Collaboration) 2016)); the first detection of a binary neutron star (BNS) merger (GW170817 (Abbott, R. *et al.* (LVK Collaboration) 2017)) that lead to the birth of multi-messenger astronomy with GW (Hartley 2017); and now dozens of detections of compact binary mergers that add up in a GW Transient Catalogue regularly updated (Abbott, R. *et al.* (LVK Collaboration) 2019)-(Abbott, R., ... and De Simone, R., *et al.* (LVK Collaboration) 2021). These detections contribute to opening a new window onto the Universe by providing insights to the populations of compact objects and the binary merger rates (Abbott, R. *et al.* (LVK Collaboration) 2021*b*); they also allow scientists to perform stringent tests of general relativity (Abbott, R. *et al.* (LVK Collaboration) 2021*c*) in a new regime of gravitation never probed before. Advanced Virgo is a power-recycled Michelson interferometer with Fabry-Perot cavities in its 3 km-long arms. By measuring length

differences between mirrors in the arms interferometer, gravitational waves are identified. Therefore, very sensitive interferometers that accurately measure the separation between suspended test masses coated to function as highly reflecting mirrors have been designed in order to detect gravitational waves. Any change in the distance between the mirrors results in a very little shift in the beams' phases, and so a changes in the intensity of the light, which depends on the wave's amplitude. A core challenge is the optimization of the mirrors for GW detectors. It is important to discover a mirror configuration that produces the least amount of additional (thermal) noise on the detection channel in addition to the typical mirror optimization design request of achieving high reflectance in a given frequency and angular range. It is well known that high reflectance mirrors typically consist of multilayers of alternating low and high refractive index materials, where each layer is quarter wave thick at the operating frequency. As a result, a simple formulation of the coating optimization problem for the design of low noise dielectric mirrors can involve looking for the sequence of thicknesses of the selected materials that make up the mirrors that minimizes the thermal noise while maintaining the transmittance below a specified threshold value. To improve the multilayers structures performance, it has been formulated and solved another design that consist in discovering (synthesizing and optimizing) improved materials that have increased optical contrast, fewer optical and mechanical losses and enabling the achievement of a specified transmittance with fewer layers, resulting into thinner coatings and lower noise and giving up the constraint of having only two constituent materials and, then, introducing new ternary multimaterial design. A check of the robustness against the inaccuracy of the deposition process has been also carried out. Furthermore, none of the materials present in nature and studied at this time qualifies as a straight substitute for the materials currently in use with the highest optical losses (TiO_2-doped Ta_2O_5 in current setups), but a few of them are better in terms of some properties (e.g., optical density, and/or mechanical losses), while unfortunately worse regarding others. The optimal material can be synthesized by using *Nanolayered structure* (NL) with thickness and equivalent refractive index that must

be chosen ad hoc to fulfill the imposed conditions: at this scope it has been introduced a novelty homogenization procedure based on an established technique, the *Abelès method*. The Abelès method is based on the physical phenomenon for which p-polarized light will not be reflected if the angle of incidence is the Brewster's angle. Hence, at this angle, the reflection coefficient at the Air-film interface is zero and the total reflection coefficient of our system is equal to the reflection coefficient at the Air-Substrate interface. So, it was possible to obtain the refractive index of the film by first measuring the reflectance of the substrate (Air-Substrate interface alone) and measuring the reflectance of the system composed of Air-Film-Substrate afterwards. Then, the two curves of the reflectance were superimposed finding the intersection between the two curves, which occurs precisely in correspondence of the Brewster angle. Finally, by exploiting the inverse equation of the definition of the Brewster angle, it was possible to know the refractive index of the film under test. Therefore, considering that the thickness of each layer is far less than the wavelength of the incident ray, all the various overlapped films have been modeled as a homogeneous film characterized by an equivalent refractive index and with a thickness equal to the sum of all the film thicknesses. The technique proposed albeit presents some theoretical glitches has been verified that works well under certain assumptions and has been experimentally validated as well. In addition, this technique has the advantage of being easy to implement in a characterization laboratory, with the drawback of being able to apply it to a single wavelength. We are now exploring an innovative approach in order to build a very sensitive detection scheme using differential interferometry. To increase the input range of wavelength and to carry out high precision measurements, Quadrature Differential Phase Interferometer is under construction.

The thesis is organized as follows. Chapter 1 is dedicated to the introduction at the GWs: what are gravitational waves, what sources do they come from, how to monitor them, the first interferometers and their improvements. Chapter 2 describes the basic theory for the study of dielectric multilayers for high-efficiency optical coatings

Chapter 3 provides an analysis of the impact of noises on the

detector. Chapter 4 studies the improvement of the sensitivity of the mirror, and so the optimization of multilayer coatings and the introduction of the nanolayered structures. Chapter 5 introduces the techniques currently used for the characterization of these structures. The results of the work and a discussion of these are reported in Chapter 6. Then, Chapter 7 concludes this thesis by opening outlooks to the future innovative approach of a very sensitive detection measurements with a QDPI. Finally, Appendix A provides an overview about the technique of deposition of the multilayer samples characterized and Appendix B show a novel temperature dependent multilayer structure at Terahertz frequencies range.

Chapter 1

Gravitational Waves

At the beginning of the 20th century, Albert Einstein revolutionized physics and astrophysics with the theories of Special and General Relativity, establishing the discipline of cosmology and offering a new framework for comprehending the cosmos on a grand scale (*LIGO website* n.d.).

The idea of a universal speed of light took the place of absolute universal length, absolute universal time and simultaneity.

Space and time are no longer independent but have been united in a singular "spacetime"; so that observers moving across space with respect to one another must experience a different flow of time.

General Relativity redefined gravity as curvature in spacetime resulting from the presence of mass and energy within that spacetime and, therefore, the existence of waves in spacetime, known as gravitational waves, was the key to this prediction. Gravitational waves were a natural consequence of Einstein's equations describing them as infinitely weak whispers in the geometric structure of the cosmos with a wavy pattern, namely ripples in the fabric of space-time that propagate at the speed of light, triggered by the acceleration of bodies, or by extremely violent cosmic cataclysms in the early Universe, supernova explosions, collisions of black holes and neutron stars.

But Einstein predicted that these waves were too weak to ever be detected by humanity, so that he produced only a theoretical framework also doubting their existence, as he himself ad-

mitted during the presentation on the "*Nonexistence of gravitational waves*". Discussed at Princeton University in New Jersey, the presentation ended with the statement (Cervantes-Cota *et al.* 2016) with which Einstein leaked his skepticism about gravitational waves:

"If you ask me whether there are gravitational waves or not, I must answer that I don't know. But it is a highly interesting problem."

The evanescent nature of gravitational waves and their weak interaction with matter makes these cosmic ripples (which turn out to be 10,000 times smaller than a proton) extremely difficult to detect. Therefore, it has aroused in the scientific community interest in advancing technologically with the intent not to leave Einstein's predictions to mere theoretical concepts. A first, albeit indirect, step towards the detection of gravitational waves was taken in 1974. In that year, Joseph Hooten Taylor and Alan Russell Hulse observed, for the first time, a binary system of neutron stars 21,000 light-years away from Earth. Using the parabola of the Arecibo radio telescope, located in Puerto Rico, the two US physicists were able to track the radio emissions of a star of the binary system. What was possible to notice was a reduction in the time interval it took for the stars in the system to orbit elliptically around their common center of mass. The recorded time reduction coincided with that estimated by Einstein, in the Theory of General Relativity, in the event that two stars were radiating gravitational waves. However, although this observation was one of the most important discoveries in the astrophysical field (involving the two US physicists the Nobel Prize in Physics in 1993) it did not involve a direct detection of gravitational waves even if it has certainly ascertained their existence. This has increased the interest of physicists, mathematicians and engineers in studying the design of gravitational interferometers considered efficient detection methodologies in the observation of gravitational waves.

In fact, on September 14, 2015, exactly one hundred years after Einstein's prediction, gravitational waves were detected for the first time through the collaboration of LIGO-Virgo kilometer-scale interferometers. For the date on which it was detected, the signal picked up was named GW150914 and is the result of the collision

of two black holes in mutual orbit before coalescence (Abbott, R. *et al.* (LVK Collaboration) 2016).

Since then, a global network of second-generation detectors has been developed and Advanced LIGO's and Advanced Virgo's (LIGO Scientific Collaboration 2015), (Acernese, F. *et al.* 2015*a*) sensitivity to gravitational waves has increased even further, resulting in, six years after the first observation, about one hundred detections (Abbott, R. *et al.* (LVK Collaboration) 2019), (Abbott, R. *et al.* (LVK Collaboration) 2021*a*).

Among them, the Gravitational Wave (GW) signal detected by two colliding neutron stars in August 2017 (GW170817) (Abbott, R. *et al.* (LVK Collaboration) 2017), marked the first time a cosmic event has been viewed in both gravitational and electromagnetic windows.

1.1 Gravitational waves: what are they?

Gravitational waves, as mentioned, are sometimes referred to as a "ripple" in spacetime. Heavy objects interact with spacetime as they travel through the universe, causing it to bend and distort neighboring objects' motions through it. We can imagine the texture of space-time as a sheet of rubber. If we place a mass on it, the elastic sheet will be deformed and anything that moves on it will follow its curvature (Figure 1.1).

So, spacetime curvature around this orbit gets highly powerful and changes very quickly if two very massive objects start circling one another very swiftly. In the form of oscillating spacetime, a considerable quantity of energy in the fluctuating spacetime travels to infinity.

We therefore define gravitational waves as the wave manifestation of propagation of a fundamental force of nature. However, gravity is a much weaker force than electromagnetism and its "electric charge" is mass, which can only be positive. Furthermore, it can only emit quadrupolar radiation, as opposed to the dipole radiation of electromagnetism.

In general relativity, Einstein's field equations connect the cur-

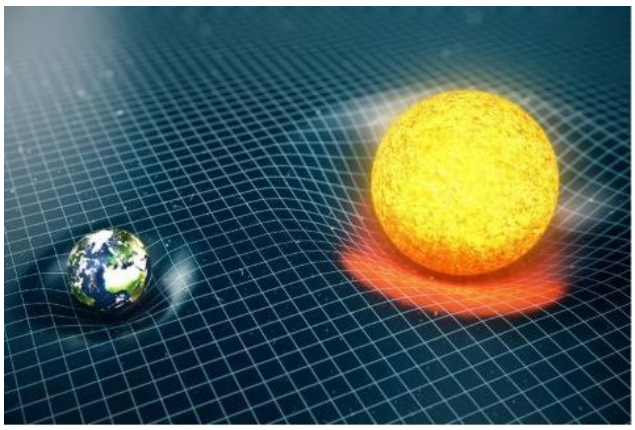

Figure 1.1: Space-time fabric deformed by the curvature of very massive bodies such as the Earth and the Sun.

Figure 1.2: Numerical simulation of two black holes close to collision

vature of spacetime to the energy and matter contained therein:

$$G_{\mu\nu} - \Lambda g_{\mu\nu} = \kappa T_{\mu\nu} \tag{1.1}$$

where $G_{\mu\nu}$ is the Einstein tensor describing spacetime curvature, Λ is the cosmological constant, $g_{\mu\nu}$ is the local spacetime metric, $\kappa = 8\pi G/c^4$ is the Einstein gravitational constant governing energy coupling to spacetime curvature, and $T_{\mu\nu}$ describes the matter and energy contained inside a spacetime as a stress-energy tensor..

In the weak-field limit, where there is no matter or energy, the stress-energy tensor $T_{\mu\nu} = 0$. Then the Einstein equations can be reduced to a wave equation and solved for small perturbations in spacetime. These solutions to Einstein's equations are known as gravitational waves. The stress-energy tensor $T_{\mu\nu} = 0$ at the weak-field limit, where there is no matter or energy. The Einstein equations may then be converted into a wave equation and solved for slight spacetime alterations. Gravitational waves are the solutions to Einstein's equations.

The gravitational wave tensor $h_{\mu\nu}$ for a wave moving in the z direction is

$$h_{\mu\nu} = \begin{pmatrix} 0 & 0 & 0 & 0 \\ 0 & h_+ & h_x & 0 \\ 0 & h_x & -h_+ & 0 \\ 0 & 0 & 0 & 0 \end{pmatrix} \tag{1.2}$$

The two polarizations of gravitational waves are represented by the coefficients h_+ and h_x, which describe how spacetime is affected by them.

A gravitational wave's impact may be observed in how it affects the distances between two objects at two points in spacetime with the sign of the change depending on the polarization and orientation with respect to the wave. For two points at distance L, the change in length ΔL is

$$\Delta L = hL \tag{1.3}$$

Where h is the gravitational wave *strain*.

In Figure 1.3 it is described the basic principle of gravitational wave detectors, where it is observed the impact of a gravitational wave with strain $h \sim 0.5$ on two test masses in terms of differential length change.

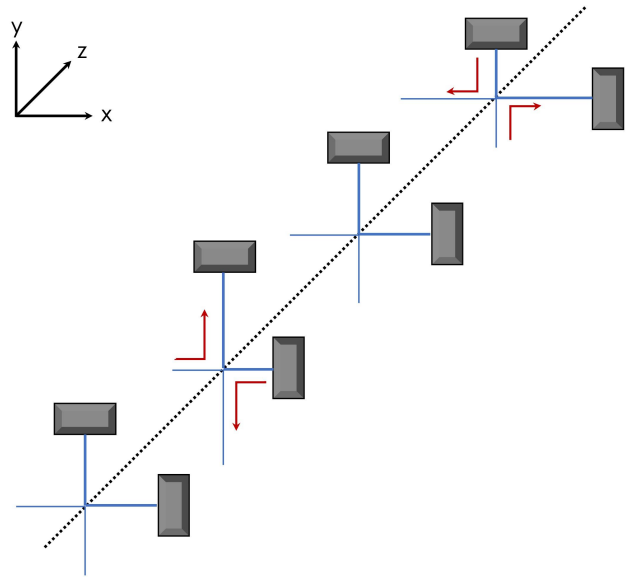

Figure 1.3: Effect on two test masses on the $x-$ and $y-$axes of a linearly polarized h_+ gravitational wave moving in the z direction. One axis is "stretched" and the other is "squeezed" in the frame to create an effective differential length change.

When any mass accelerates across spacetime, such as in the orbit of two objects, gravitational waves are created. In reality, gravity is a "weak" force, and spacetime is a "stiff" medium. Only the universe's most massive objects can significantly alter spacetime, and only the most massive, energetic orbits can produce notable gravitational waves.

As they propagate away from their source throughout space, gravitational waves lose amplitude in a manner that is inversely proportionate to their distance. Propagating at the speed of light, gravitational waves interact very weakly with matter and so the strongest gravitational waves that reach Earth are all from extremely distant, rare, ultra-powerful astrophysical collisions.

If for example, we take a supernovae explosion (the strongest gravitational waves reaching Earth) at Virgo cluster (15 Mpc) in which energy equivalent to $10^{-4}M$ is produced, produces gravitational waves of 100 Hz and the signal duration is 1 msec, the amplitude of the gravitational wave on earth will be $\sim 10^{-21}$.

Gravitational waves incident on L=4 km long detectors will be

$$\Delta l = h \cdot l = 10^{-22} \cdot 4km \sim 10^{-18}m$$

which is 1000 times smaller than the diameter of a proton. For reference, a human cell is $10^{-4}m$, the size of an atom $10^{-10}m$, the size of the nucleus of that atom is $10^{-15}m$.

Therefore, the Advanced LIGO and Advanced VIRGO detectors' sensitivity to gravitational waves is a remarkable technological achievement, and the gravitational wave data represents an important new source of knowledge about the depths of the universe.

This characteristic means that detecting gravitational waves may offer a relatively unhindered view of the Universe, a view that is inaccessible to electromagnetic radiation-based astronomy.

In fact, unlike EM radiation, which can be absorbed, reflected, refracted or bent, GWs travel through the Universe practically without obstacles, giving a clear view of the Universe of gravitational waves. Waves carry information about their origin that is free of distortions or alterations suffered by EM radiation as it passes through intergalactic space.

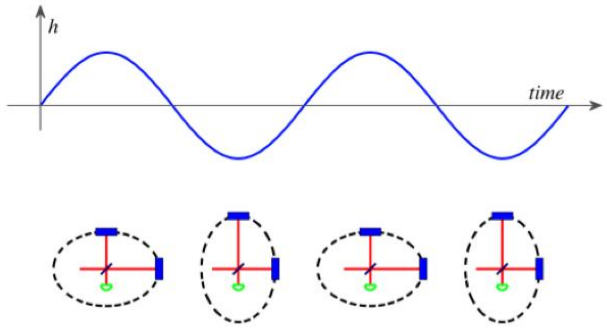

Figure 1.4: A GW that is traveling perpendicular to the diagram's plane has a strain amplitude of h. The ring of particles is bent by the wave into an ellipse, which is lengthened in one direction during one half of the wave's cycle and in the opposite direction during the next half.

For example, it allows the possibility of gaining insights from the formation of the Universe from 10^{-36} seconds after the Big Bang, or approximately 300000 years earlier than electromagnetic-based astronomy is capable of (Maggiore 2000), as well as dynamics of Supernovae core collapses (Logue, J. *et al.* 2012). Furthermore, gravitational waves are generated from these phenomena directly, thus carry direct information about the characteristics of these objects/events (Flanagan & Hughes 1998).

1.2 Sources of gravitational waves

A novel, unique source of knowledge about the universe's darkest, most massive objects, and most intense events is provided by gravitational waves. Except for the gravitational wave signal they leave behind, events that are typically inaccessible by light, such as binary black hole mergers, supernovae core bounces, or the Big Bang, are utterly unseen to observers on Earth. Therefore, GWs may be used to directly monitor these occurrences.

Four categories of gravitational waves have been defined based on what generates them and therefore on the basis of the characteristic set of signals that the LIGO-VIRGO-KAGRA interferom-

eters can sense: Continuous, Compact Binary Inspiral, Stochastic and Burst.

1.2.1 Continuous gravitational waves

Continuous gravitational waves are thought to be produced by a single massive rotating object such as a neutron star whose rotation speed following collisions or imperfections in the spherical shape while remaining constant generates GWs which are also constant (continuous frequency and amplitude).

1.2.2 Compact Binary Inspiral Gravitational Waves

So far, all of the objects detected by LIGO-VIRGO fall into this category. Compact binary inspiral gravitational waves are produced by orbiting pairs of massive and dense ("compact") objects like white dwarf stars, black holes, and neutron stars. There are three subclasses of "compact binary" systems in this category of gravitational-wave generators:

- Binary Neutron Star (BNS)
- Binary Black Hole (BBH)
- Neutron Star-Black Hole Binary (NSBH)

Each binary pair creates a unique pattern of gravitational waves, generated by the same mechanism called "inspiral".

Inspiral occurs over millions of years when pairs of compact and dense objects rotate around each other emitting gravitational waves that take away some of the orbital energy of the system. As a result, objects orbit closer and closer to each other, which increases the speed and thus causes them to emit stronger gravitational waves and therefore to a greater total energy loss of the system. Objects are doomed, inevitably stuck in a spiral embrace that accelerates on the run.

This process triggers an unstoppable sequence of events that can only end with the collision of the two objects.

Interferometers are designed to detect a specific frequency range of gravitational waves. This means that they are unable to detect objects in orbit at speeds that do not fall within this frequency range (too low or too high). However, as the orbiting objects approach, they will begin to orbit each other fast enough that the gravitational waves they emit fall within the sensitivity range. But the time they spend in orbit in that frequency range is typically very brief.

The first pair of merging black holes detected produced a signal only two tenths of a second long; in contrast, the first neutron star merger detected in August 2017 generated a signal over 100 seconds long in the instruments. This is due to the fact that heavy objects, such as black holes, move through their final inhalation phase much faster than "lighter" objects, such as neutron stars, and, therefore, the masses of the objects involved determine how long they emit detectable gravitational waves.

1.2.3 Stochastic Gravitational Waves

Astronomers do not foresee the possibility that more than one gravitational wave will pass through the Earth at the same time and therefore confusing signals will occur in the detectors since there are few significant sources of continuous or binary inspiral gravitational waves in the Universe. However, it is assumed that many small gravitational waves continuously pass through the Universe and that they are mixed together at random forming what is called a "Stochastic Signal" from which they are called stochastic gravitational waves. These will be the smallest and most difficult to detect gravitational waves, waves that contribute to cosmic background noise and that continuously and randomly cross the Universe, but this stochastic signal could have some connection to the Big Bang, at least in part. We will be able to look further back in the history of the Universe than ever before thanks to the discovery of gravitational wave remnants from the Big Bang. .

1.2.4 Burst Gravitational Waves

The search for "burst gravitational waves" is called a search for the unexpected, both because they have yet to be detected, and because there are many unknowns about the physics of the system to predict how gravitational waves from that source will look. The most promising sources are presently considered to be coalescent binaries, with several events per year according to recent encouraging studies. Moreover, the evolution of the signals can be well modeled, so that a matching filter technique can be applied.

1.3 Origin Of Gravitational Interferometers

Historically, the study of the Universe has always been entrusted mainly to observations made by electromagnetic radiation, i.e. radio waves, microwaves, X-rays but also by subatomic particles, including neutrinos and cosmic rays. (*LIGO website* n.d.) These types of signals have been detected by the scientific community as a result of the use of telescopes and observatories present both on Earth and in orbit on satellites, as in the case of the Hubble Space Telescope. Launched into Earth orbit in 1990, since that year has been used for observation in the near ultraviolet, visible and near infrared, managing to complete in 97 minutes a rotation around the Earth. For the study of gravitational waves, physicists and astrophysicists have worked, since the first theorization of Einstein, to design a technology capable of detecting such imperceptible fluctuations. In 1966, Joseph Weber, made an antenna based on the idea that gravitational waves could be detected by measuring induced vibrations in a mechanical system (Cervantes-Cota *et al.* 2016). The design of the antenna, Figure 1.5, included an aluminum cylinder weighing three tons hooked, through a steel cable, to a support whose purpose was to isolate the system from the noise of the surrounding environment. Isolation was further ensured by placing the prototype inside a chamber designed to isolate the antenna from external noise and vibration. According to Weber, the detection of gravitational waves would have taken

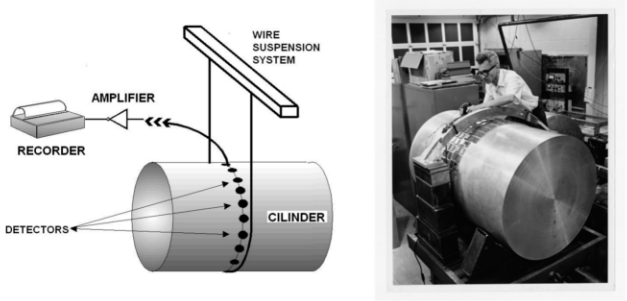

Figure 1.5: Weber's prototype antenna

place thanks to the addition of detectors made with piezoelectric crystals. Positioned to surround the cylinder, the purpose of piezoelectric crystals was to pick up vibrations induced in the antenna by the presence of gravitational waves and to convert mechanical vibrations into electrical impulses. Weber's prototype has never convinced the scientific community as the measurements carried out have always been compromised by spurious vibrations, electromagnetic interference and background noise. Although Weber is still considered a pioneer inthe study of gravitational waves, the measurements made with his antenna have never produced results that confirm the existence of gravitational waves. For this reason, scientists, engineers and astrophysicists have invested their interest in the gravitational interferometer.

Typically, an interferometer is an instrument for investigating small variations in microorganisms, cosmic gas structure and gravitational waves. All interferometers are characterized by the overlapping of light rays from which an interference pattern called "fringes" is determined (comparable, for example, to ripples on a stretch of water that intersect with each other) to be measured and analyzed to know the information of the object of interest.

Some scientists began the study of the interferometer between the middle and the end of the 1800s but it will be necessary to wait until 1971 to have the realization of the first prototype of the interferometer. In fact, the model of this tool is extremely complex because, in order to be able to make extremely small measurements, it is necessary to take into account three fundamental aspects:

- *the amplitude*, gravitational waves are extremely weak when they finally reach the Earth;
- *variability over time*, when the fluctuation coincides with the matter generates a wave whose intensity is not constant throughout the time of the wave-mass interaction;
- *the source*, the gravitational waves differ according to the source from which they were generated.

From the above considerations, various macroscale devices have been developed over the years for detecting gravitational waves. The first one is essentially a Michelson interferometer with some important modifications, suspended mirrors (Saulson 1994) illuminated by a monochromatic laser source, which was then the basis from which to realize subsequent interferometers, of the first and second generation, more complex but more reliable and with considerably increased sensitivity.

Today the realization of interferometers has reached the third generation. An example is the Einstein Telescope, which is a triangular interferometer of remarkable size buried at a depth ranging from 100 meters to 300 meters in order to ensure isolation from seismic waves.

1.3.1 Michelson Interferometers

The Michelson interferometer, made by the American physicist Albert Abraham Michelson, is the simplest and most widespread interferometer. In 1887 this instrument was successful in proving the existence of ether; it is only in the 60s that Michelson's interferometer was identified as an ideal means for the detection of gravitational waves. The operation of this instrument is triggered when a single beam of monochromatic light is emitted from the source, represented by a laser, which allows to have a high-precision interference pattern. The beam of light affecting a *beam splitter*, which assumes an angular position of 45 deg, splits into two separate beams that propagate perpendicular to two mirrors used as reflective surfaces. The *beam splitter* is an optical device that can be made with two prisms, glued together, and positioned so as to

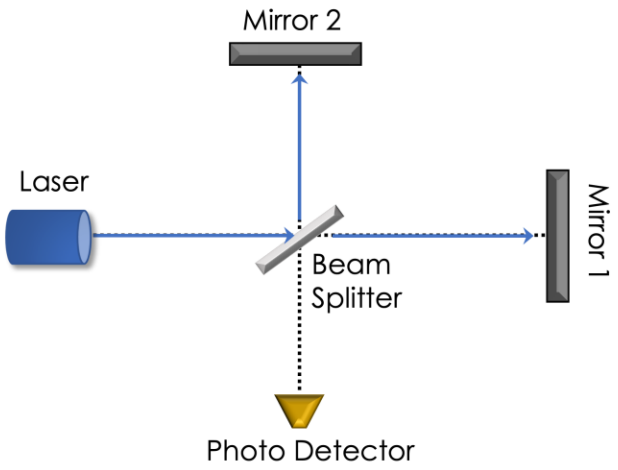

Figure 1.6: Light beam emitted by the laser and split by the beam splitter into two beams incident on the mirrors

take on a cubic shape, or with a glass plate covered with a thin semi-silver coating. In this case we are talking about plate beam dividers and it is the type of beam splitter used in the Michelson interferometer. This optical component not only has the ability to split the beam of light that affects its surface into two beams but is also able to combine two beams of light into a single beam. The optical and mechanical properties of mirrors play a crucial role in detecting gravitational waves. They are characterized by a spherical shape and the weight and thickness depend on the power carried by the signal in the interferometer. These are very often referred to as retro-reflectors or tri-rectangular prisms that reflect the incident radiation beam in the same direction of origin. Figure 1.6 show the beam of light emitted by the source that incise on the surface of the beam splitter; the two rays are reflected from the semi-reflective surface of the beam splitter in such a way that the first radius, called reference, affects the mirror placed at the top of the light beam separator and the second ray, called measurement, affects the mirror parallel to the separator. Referring to Figure 1.7, it is clear how the two rays are reflected by the two mirrors to rejoin again in a single beam, through the beam splitter, to be channeled in the direction of the photosensitive element. When

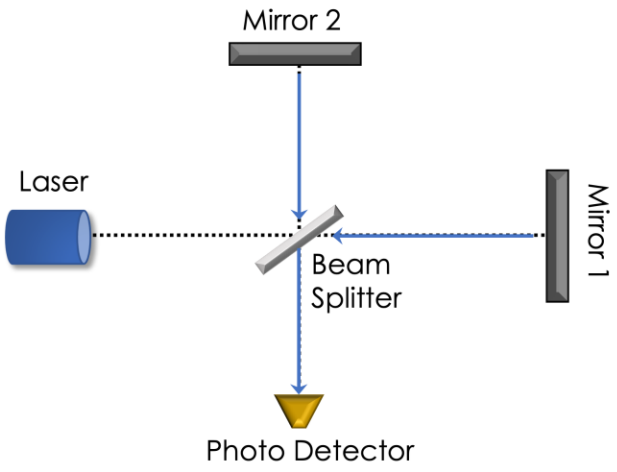

Figure 1.7: The two beams of light reflected by the mirrors and recombined into a single beam, from the beam splitter, to engrave the photo detector

the beams rejoin in a single beam, they interfere with each other in a destructive or constructive way. In fact, there is constructive interference when the two light beams are in phase resulting in a bright fringe. Conversely, when the two beams are not in phase with each other, there is a destructive interference that instead involves a "*dark fringe*". In general, Michelson gravitational interferometers achieve maximum sensitivity by working in the dark fringe in such a way that most of the light beam is reflected. In this way the interferometer is indifferent to any fluctuations in power that are therefore not mistakenly interpreted as a consequence of the passage of a gravitational wave.

The interferences that are created determine a variation in intensity with respect to the beam of light that is initially emitted by the source. In fact, the power P_{out} measured by the light beam obtained is proportional to the power P_{in} relative to the initial beam according to the equation:

$$P_{out} \propto P_{in} \sin^2 \left(k \left(L_y - L_x \right) \right) = P_{in \sin^2(\delta\phi)} \tag{1.4}$$

where $k = \frac{2\pi}{\lambda}$ is the wavenumber of the light emitted by the laser while L_y and L_x indicating the length of the interferometric arms

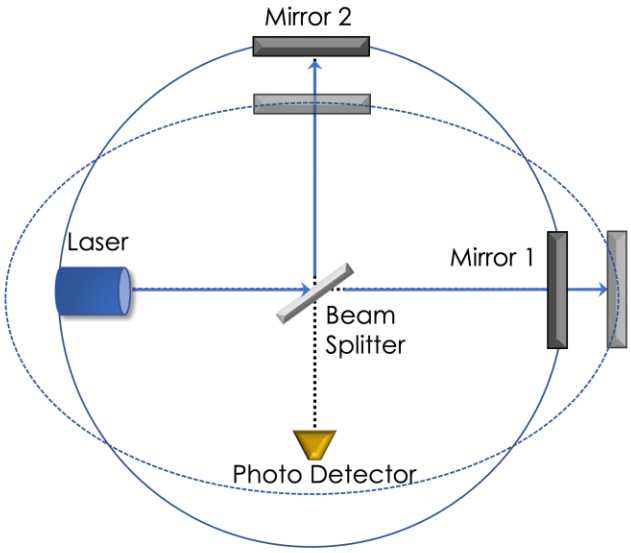

Figure 1.8: A Michelson Interferometer acting as a gravitational wave detector. The interference pattern is created at the output port when GW passes, which causes one arm to shrink while the other lengthens.

and $\delta\phi$ is the phase. The latter is a parameter given by the sum of a contribution, ϕ_{gw}, relating to the phase shift that occurs following the passage of the gravitational wave, with respect to a contribution, ϕ_0, with which the interferometer works at maximum performance:

$$\delta\phi = \phi_0 + \phi_{gw} \tag{1.5}$$

Measuring the change in intensity is essential to determine the possible presence of gravitational waves. When the light radiation takes the same time to travel the two interferometric distances, there are no changes in intensity compared to the light beam initially emitted by the laser. In this way it is concluded that there were no passages of gravitational waves through the interferometer. Conversely, when you are in the presence of gravitational waves there is a variation in the distance that connects the mirrors with the light beam separator (ie a variation in lengths L_y and L_x), Figure 1.8.

This causes, as can be seen from the Equation 1.4, a variation

in the phase $\delta\phi$ with consequent variation of the measured power. It is therefore established the passage of the gravitational wave. In fact, if the gravitational wave passes through the interferometer, the distance of a mirror increases with respect to the position in which the beam splitter is placed, unlike the second mirror whose position is closer to the beam separator. This trend repeats alternately and persists for as long as the gravitational wave crosses.

To estimate the intensity of the light beam and its possible modification, consider the dimensionless parameter "h" which depends on the frequency, polarization and direction of incidence of the gravitational wave. As already seen, the parameter of the order of 10^{22} defines the expected force of the wave and is essential when designing the interferometer: two masses placed at a distance L from each other, after the incidence of gravitational waves, they are perturbed assuming a new position that is at a distance ΔL from the initial location. The displacement, which the two masses undergo due to the incidence of gravitational waves, can be measured with the help not only of the initial position but also of this parameter h:

$$\Delta L = \frac{hL}{2} \tag{1.6}$$

If we consider the masses of the example as the mirrors of the interferometer and L as the length of the arm of the latter it is possible to understand, from the Equation 1.6 , that the variation in the length of the interferometer arm depends on the parameter h and therefore on the intensity of the gravitational wave. In general, the ideal value of the distance L must be such as to correspond to the frequency of the gravitational wave you want to detect. This is because, again referring to Equation 1.4, ΔL it is all the greater the length of the interferometric arm (since they are in a relation of direct proportionality).

The extremely simple design of Michelson's interferometer is not sufficient to make the detector sensitive to the expected GW signals. It was therefore necessary to apply particular techniques in the development of the interferometers described below making its model the basis from which they were designed.

1.4 Advanced Gravitational Interferometers

The main problem in Michelson's interferometer lies in the fact that the distance that separates the mirrors from the beam splitter is in the order of meters (about 1.3 meters), making it too short for a gravitational wave detection. This inadequacy of the interferometer also survives by modifying the support structure of the test masses, passing from a rigidly fixed system to one that emulates a pendulum in order to have an interferometric arm several kilometers long.

1.4.1 First Generation Interferometer

This interferometer represents a new type of instrument classified as a first-generation gravitational wave detector and is generally referred to as the Fabry-Perot Michelson recycled power interferometer. The novelty lies in the addition of two new mirrors, defined as initial or *input mirrors*, in the interferometric arms. The initial mirrors are placed to be very close to the *beam splitter* and at a distance of a couple of kilometers from the mirrors present in the final part of the interferometric arm. For this reason these mirrors are called final mirrors or *output mirrors*. With this new structure, what is created is a Fabry-Perot cavity, Figure . The etalon, an alternative terminology used to indicate the Fabry-Perot cavity, is the simplest optical resonator. It is bounded by two dielectric mirrors, equal and parallel to each other, whose partially reflective surface allows and multiple reflections of light within the cavity.

The beam of light is emitted by a laser diode which amplifies, in four steps, its power and perfects its wavelength to a high level of precision. Initially the laser diode (800 times more powerful than classic laser pointers) emits a 4-watt beam which is sent into a crystal. This is called a non-planar ring oscillator, from which the emission of a ray, called seed, of 2 watts and a wavelength of 1064nm is stimulated. The seed undergoes two amplification processes, through a high-power oscillator, in order to have a 200-watt signal ready to be fed into the interferometer. The signal propa-

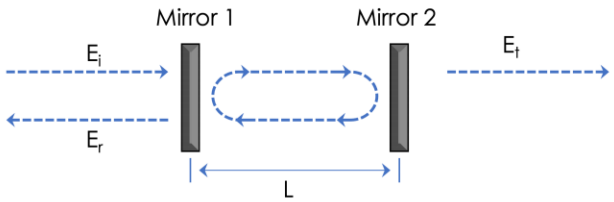

Figure 1.9: Fabry Perot cavity. Two mirrors placed at a distance of L. Let Mirror 1 be the front mirror and Mirror 2 be end mirror.

gates to affect the beam splitter from which two distinct rays are obtained, as happens in the classic Michelson interferometer. However, with the Fabry-Perot cavity formed by the addition of *mirror inputs*, the beam propagates by bouncing between the initial and final mirror at least 300 times before joining the beam of the second arm. This involves the accumulation of light and an increase in power inside the instrument with a consequent increase in the distance, of the order of thousands of kilometers, covered by the two beams of light. Working at high power is an advantage both because the fringes, that is the interference pattern, measured with the photosensitive element are sharper and because there is a reduction in noise. In fact, shot noise is spoken of as the main type of noise coming from light and consequently from photons (i.e., from how many energy discretes). For this reason, in addition to the input mirrors, an additional mirror called PRM, also known as *Power Recycling Mirror*, is added, as can be deduced from Figure 1.10. This additional mirror is placed between the laser and the beam splitter. Its task is to continuously reflect the light (this is why we talk about energy recycling) in order to increase the power, of the order of a few watts deriving from the laser, to a value of the order of MW in the Fabry Perot cavities. . Furthermore, the mirrors are made to have a weight of at least 40kg so as not to confuse the fluctuations produced by the shot noise with the actual gravitational waves. An example of a first generation gravitational interferometer is the one used in the US LIGO observatory, also known as the Laser Interferometer Gravitational wave Observatory. It is a terrestrial research facility in which the interferometer is used for detecting the vibrations of gravitational

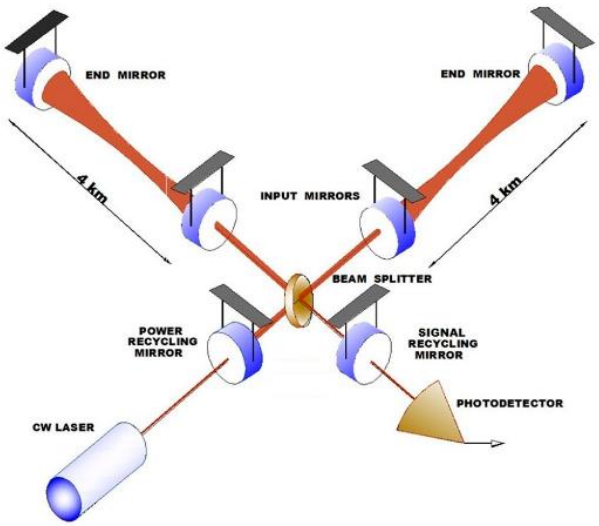

Figure 1.10: LIGO Interferometer

Figure 1.11: LIGO Hanford and LIGO Livingston (*LIGO website* n.d.)

waves in a frequency range ranging from 10Hz to 2kHz. In fact, two interferometers are employed making this research facility the largest in the world. The two interferometers are located one in the state of Washington, precisely in Hanford, and another three thousand kilometers away, precisely in Livingston in the state of Louisiana. The LIGO interferometers are the largest ever made by presenting interferometric arms 4 kilometers long, as shown in Figure 1.10. This, as is well known, involves an increase in the sensitivity of the instrument capable of measuring even the smallest changes. The two arms of each LIGO detector are arranged at right angles and are covered in concrete that acts as a protection against disturbances originating in the external environment.

Other measures have been applied to ensure that the operation of the interferometer is optimal, trying to remove the main causes of noise which will be explored in the next chapter. First, a technology has been designed that can remove the smallest unwanted vibrations (e.g. earthquakes or motor vehicles on nearby roads) that could obscure the passage of gravitational fluctuations. To achieve this, two techniques have been developed:

- **active damping**, which intervenes at the forefront to block all unwanted oscillations. It is defined ISI, or internal seismic isolation, and consists of a set of devices, such as sensors, for detecting vibrations from the ground and the environment at different frequencies. These are eliminated by applying movements opposite to those generated by the oscillations that one wants to cancel;

- **passive damping**, wich intervenes to extinguish all those movements that the active damping has not been able to cancel. This damping is achieved with a structure with four pendulums (called *quad*) with which the test masses are suspended, an alternative terminology used to indicate interferometric mirrors.

Another way that allows you to perfect the interferometer is the use of *vacuum systems*. In fact, due to the Brownian motion, the air particles, subject to a temperature above absolute zero, move with thermal energy. This means that when the air molecules collide with a mirror, a variation in the length of the interferometric arm is recorded which can be mistakenly confused as proof of the passage of the gravitational wave. Another consequence is that air can act as a lens by varying the propagation path of light, producing an interference pattern that could incorrectly suggest the passage of a gravitational wave. In addition to air molecules, dust can also be a source of problems because it is another cause for which the light beam can propagate in a direction other than that imposed by the interferometer. LIGO has an elaborate IT infrastructure including supercomputers located at MIT, *Massachusetts Institute of Technology*, and other institutions. This is because the gravitational interferometer must be able to measure a movement

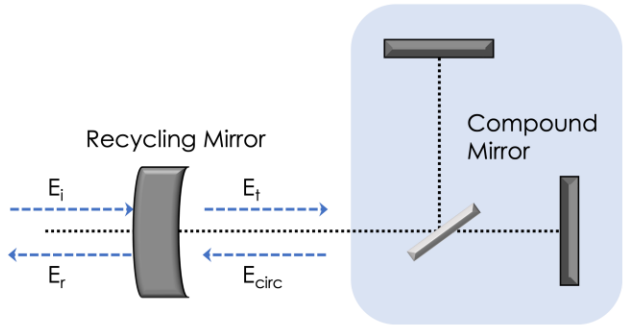

Figure 1.12: Recycling cavity formed by a recycling mirror and a compuond mirror

thousands of times smaller than a proton and this involves collecting and managing a large amount of extremely complex data. The first-generation interferometer has a main problem, namely noise not only related to the surrounding environment but also to fluctuations inherent in the laser itself. Despite the precautions taken with active and passive insulation systems, first-generation interferometer detections can still be compromised. The technological developments obtained above all in terms of noise reduction have led to a design that includes new *features*.

1.4.2 Second Generation Interferometer

The Second-Generation Interferometer, also called *Advanced*, can be considered as a refinement of the first generation one with the advantage of having an increase in sensitivity of at least ten times greater. Firstly, the test-masses, i.e., the mirrors, are suspended no longer with steel cables but with fused silica fibers with a diameter of 0.4 mm. Between the *beam splitter* and the photo detector has been placed a new semi-reflective mirror called *signal recycling mirror* (SRM). If PRC, *Power Recycling Cavity*, is used either in the first-generation structure to increase the power of the light radiation in the interferometric arm, the signal recycling mirror (SRM) allows to extend the frequency range and thus maximize the sensitivity of the interferometer. Looking at Figure 1.13, you can spot other additional elements to the previous model. Currently available lasers are not adequate to emit a beam of light

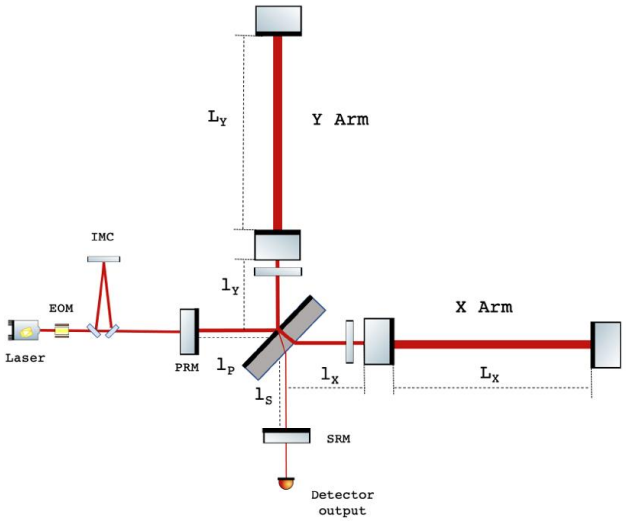

Figure 1.13: Second Generation Interferometer

directly into the interferometer. For this reason, to improve the quality of the laser beam, once the light beam is produced and amplified, the signal passes through three optical cavities:

- PMC, *Pre-Mode Cleaner*;
- IMC, *Input Mode Cleaner*;
- RFC, *Reference Frequency Cavity.*

This instrument is called the Michelson Fabry-Perot double recycling interferometer. An example is given by the European interferometer Advanced Virgo. The name comes from the Virgo Cluster or from the richest agglomeration of galaxies that is estimated to be composed of more than 2000 members, covering a distance of 60 million light years. Located in the rural area of Tuscany, the Advanced Virgo interferometer is part of the global network of detectors that since 2007 has been involved in the observation of the passage of gravitational waves. In fact, in 2017 this interferometer detected the first gravitational wave, classified as GW170817, emitted by the coalescence of a binary neutron star (Nardecchia 2022). Advanced Virgo has two perpendicular

Figure 1.14: Advanced Virgo Interferometer

paths, namely the interferometric arms, with a length of 3 kilometers. So, as well as for the LIGO interferometer also in this case the laser path is bent hundreds of times before the light recombines to the beam splitter (*VIRGO website* n.d.). The two mirrors of the interferometer have a weight of 42kg each and are placed one near the beam splitter and the other 3km away. Performance is improved by atomically polishing the mirrors, which have a coating on the surface that allows almost all light to be reflected. To reduce the impact of unwanted vibrations, a special support system for the test masses has been developed. The mirrors, in fact, are almost completely suspended as they are connected with four silic fibers and cast with two steel dais called puppets. The support system in total is called *payload* and consists of the *Marionette*-mirror assembly, to the ears (to which the silica fibers are attached to support the mirror) and the anchors that fix the ears to the test masses, as can be seen from the Figure 1.15 below: All the technological innovations developed over the years that have invested precision lasers, vacuum technology and advanced optical and mechanical systems made it possible, on September 14, 2015, to detect the first gravitational wave. In fact, the remarkable engineering behind interferometers such as Advanced Virgo and LIGO, has allowed the achievement of a sensitivity capable of detecting infinitely small cosmic signals. These faint fluctuations have also been converted into an audible sound, called chirping,

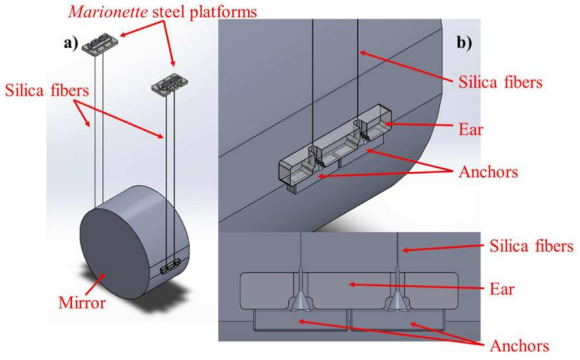

Figure 1.15: Monolithic suspension design, with highlighted details (Acernese, F. *et al.* 2015*a*)

and are relative to the last few seconds before the coalescence of black holes. In fact, it has been estimated that the signal detected on September 14 is the result of the energy dissipated by the rotation of two black holes (with masses of 36 and 29 times that of the sun) around the common center of mass. The important discovery of 2015 was then followed by an even more important survey, which took place in 2017, relating to the gravitational wave deriving from a binary system of neutron stars. These important results have made it possible to remove a veil of mystery about the Universe by inaugurating new research to improve the detections of gravitational waves.

Chapter 2

Theoretical Framework

2.1 Maxwell's Equations and Plane Electromagnetic Waves

The study of the phenomena related to the propagation of an electromagnetic field in a multilayer thin film is based on a set of well-known equations which are called *Maxwell's equations*. These, jointly with the constitutive material equations, establish spatio-temporal relationships between the vectors of the field and the sources and can take different forms depending on the mathematical operators involved. In isotropic media, these are:

$$\nabla \times \boldsymbol{E} = -\jmath\omega\boldsymbol{B} \tag{2.1a}$$

$$\nabla \times \boldsymbol{H} = \jmath\omega\boldsymbol{d} + \boldsymbol{J} + \boldsymbol{J}_0 \tag{2.1b}$$

$$\nabla \cdot \boldsymbol{D} = \rho \tag{2.1c}$$

$$\nabla \cdot \boldsymbol{B} = 0 \tag{2.1d}$$

$$\boldsymbol{J} = \sigma\boldsymbol{E} \tag{2.2}$$

$$\boldsymbol{D} = \varepsilon\boldsymbol{E} \tag{2.3}$$

$$\boldsymbol{B} = \mu\boldsymbol{H} \tag{2.4}$$

where

$\boldsymbol{E}$ is the electric field strength (V/m)

$\boldsymbol{H}$ is the magnetic field strength (A/m)

$\boldsymbol{D}$ is the electric displacement (C/m^2)

$\boldsymbol{B}$ is the magnetic flux density or magnetic induction (Wb/m^2)

$\boldsymbol{J}$ is the electric current density (A/m^2)

$\boldsymbol{J}_0$ is the source current density (A/m^2)

ρ is the electric charge density (C/m^3)

σ is the electric conductivity (S/m)

ε is the permittivity (F/m)

μ is the permeability (H/m)

The permittivity and permeability can be expressed by

$$\varepsilon = \varepsilon_r \varepsilon_0 \tag{2.5}$$

$$\mu = \mu_r \mu_0 \tag{2.6}$$

$$\varepsilon = 1/(\mu_0 c^2) \tag{2.7}$$

where ε_r and μ_r are the relative permittivity and permeability, respectively; ε_0 and μ_0 are the permittivity and permeability of free space, c is a constant that can be identified as the velocity of light in free space. The value of this constant are given in (Tabella 2.1)

Symbol	**Free-space Physical Quantity**	**Value**
c	Velocity of light	$2.997925 \times 10^8 (m/s)$
μ_0	Permeability	$1.256637 \times 10^{-6} (H/m)$
ε_0	Permittivity $= 1/(\mu_0 c^2)$	$8.854185 \times 10^{-12} (F/m)$

Table 2.1: Values of c, ε_0 and μ_0

The refractive index is also defined as the ratio between the speed of light in free space c and the speed of light in the medium v:

$$\sqrt{\varepsilon} = c/v = n - \imath k \tag{2.8}$$

it is often called complex refractive index and it is always a function of λ, while n real refractive index (or simply refractive index) and k extinction coefficient. The term k is related to the absorption coefficient α by the relation:

$$\alpha = 4\pi k/\lambda \tag{2.9}$$

Light waves are solutions of Maxwell's equations and therefore are electromagnetic fields. The light wave is a homogeneous, plane, linearly polarized harmonic (or monochromatic) wave and can be described in terms of electric and magnetic fields propagating along the z-axis in the form

$$\boldsymbol{E} = \boldsymbol{E}_0 \exp\left[i\omega t - \left(2\pi\sqrt{\varepsilon}/\lambda\right) z + \varphi\right] \tag{2.10}$$

$$\boldsymbol{H} = \boldsymbol{H}_0 \exp\left[i\omega t - \left(2\pi\sqrt{\varepsilon}/\lambda\right) z + \varphi'\right] \tag{2.11}$$

where $\boldsymbol{E}_0$ and $\boldsymbol{H}_0$ is the electric amplitude, z is the distance along the direction of propagation, and φ is an arbitrary phase.

Therefore, crossing a distance d in the medium, the wave undergoes a phase variation and a reduction in amplitude.

Likewise, a wave propagating in a direction given by direction coefficient (α, β, γ) of the vector

$$\hat{\boldsymbol{s}} = \alpha\boldsymbol{i} + \beta\boldsymbol{j} + \gamma\boldsymbol{k} \tag{2.12}$$

with $\boldsymbol{i}$, $\boldsymbol{j}$ and $\boldsymbol{k}$ unit vectors along x, y and z axes, respectively, can be described by

$$\boldsymbol{E} = \boldsymbol{E}_0 \exp\left[i\omega t - \left(2\pi\sqrt{\varepsilon}/\lambda\right)(\alpha x + \beta y + \gamma z)\right] \tag{2.13}$$

This is the easiest type of wave in an absorbing medium. In a multilayer structure of absorbing thin films, the wave expression will be somewhat more complicated.

Some important relationships can be derived from Maxwell's equations, such as the optical admittance which is defined as the complex ratio of the magnetic and electric fields

$$y = H/E \tag{2.14}$$

In free space, y is real and is denoted by Y_0.

$$Y_0 = (\varepsilon_0/\mu_0)^{1/2} = 2.6544 \times 10^{-3} S \tag{2.15}$$

At optical frequencies μ_r is unitary since the direct magnetic interactions are quite tiny and being $\mu = \mu_r \mu_0$, it is possible to write

$$y = (n - \imath k) Y_0 \tag{2.16}$$

2.1.1 The Poynting Vector

The fact that electromagnetic radiation is a form of energy transport is a crucial characteristic, and the instantaneous rate of flow of energy across unit area is given by the Poynting vector

$$\boldsymbol{S} = \boldsymbol{E} \times \boldsymbol{H} \tag{2.17}$$

The direction of the energy flow corresponds to the direction of the vector. The mean rate of flow of energy per unit area carried by the wave, is defined as the irradiance of the light

$$I = \frac{1}{2} \operatorname{Re}(EH^*) \tag{2.18}$$

where * denotes complex conjugate. For a homogeneous and harmonic wave seen in Equation (2.13):

$$\boldsymbol{H} = y\,(\hat{\boldsymbol{s}} \times \boldsymbol{E}) \tag{2.19}$$

so that

$$\boldsymbol{I} = \operatorname{Re}\left(\frac{1}{2} y \boldsymbol{E}\boldsymbol{E}^* \hat{\boldsymbol{s}}\right) = \frac{1}{2} n Y_0 \boldsymbol{E}\boldsymbol{E}^* \hat{\boldsymbol{s}} \tag{2.20}$$

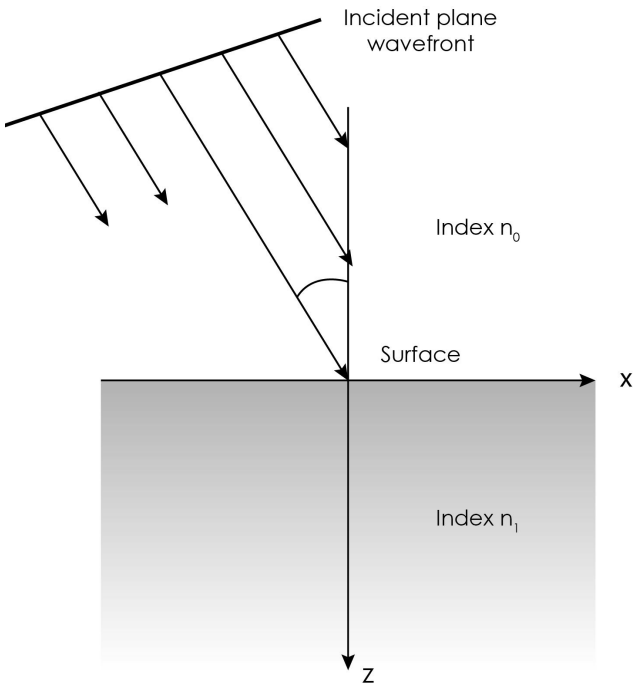

Figure 2.1: Plane wave front incident on a single surface.

2.2 The Simple Boundary

The majority of thin-film filters are made up of interfaces between distinct homogeneous materials, and the simplest case is that of the single boundary. As can be seen in Figure 2.1, a plane harmonic wave is incident at the separation interface between two media. The incident wave is reflected in the first medium and transmitted in the second. The *plane of incidence* is defined as the plane comprising the normal to the surface and the wave's direction of propagation. It is considered the x-axis to be normal to the incident wave and belonging to the plane of incidence and the z-axis to be normal into the surface in the direction of incidence. The components along the boundary of $\boldsymbol{E}$ and $\boldsymbol{H}$, tangential components, are continuous across it.

The aim is the determination of the relative parameters of the incident, reflected, and transmitted waves. The boundary condi-

tions will be employed to create a set of equations from which the relevant relations may be derived. There will be variations in the phase factors since the reflected wave will travel differently from the others. The boundary is specified by $z = 0$, which removes the z component from the phase factors at the boundary. In such case, all values of x, y, and t must result in continuous tangential components. Let $(\alpha_t, \beta_t, \gamma_t)$ and $(\alpha_r, \beta_r, \gamma_r)$, respectively represent the direction cosines of the $\hat{\boldsymbol{s}}$ vectors of the transmitted and reflected waves. As a result, the phase factors may be written as follows:

- Incident wave: $\exp\{\imath\left[\omega t - (2\pi n_0 \lambda_i)\left(x \sin\vartheta_0 + z\cos\vartheta_0\right)\right]\}$
- Reflected wave: $\exp\{\imath\left[\omega t - (2\pi n_0 \lambda_r)\left(\alpha_r x + \beta_r y + \gamma_r z\right)\right]\}$
- Transmitted wave: $\exp\{\imath\left[\omega t - (2\pi n_1 \lambda_t)\left(\alpha_t x + \beta_t y + \gamma_t z\right)\right]\}$

The complex amplitudes of these waves contain their relative phases. The assumption that phase factors satisfying the boundary requirements for all x, y, t at $z = 0$, involve that the coefficients of these variables must be independently identically equal. The plane of incidence is the only place where the directions of the reflected, transmitted, or refracted beams can be.

$$0 \equiv n_0\beta_r \equiv n_t\beta_t \tag{2.21}$$

The direction cosines of the transmitted and reflected waves then take the following form:

$$\alpha = \sin\vartheta \qquad \gamma = \cos\vartheta \tag{2.22}$$

Also

$$n_0 \sin\vartheta_0 \equiv n_0\alpha_r \equiv n_1\alpha_t \tag{2.23}$$

so the angle of reflection ϑ_r and the angle of incidence are equal

$$\vartheta_0 = \vartheta_r \tag{2.24}$$

and

$$n_0 \sin\vartheta_0 = n_1 \sin\vartheta_t \tag{2.25}$$

or, for simmetry, we can write

$$n_0 \sin \vartheta_0 = n_1 \sin \vartheta_1 \tag{2.26}$$

This relationship are well-known as Snell's law. Then, γ_r and γ_t are given by

$$\alpha_r^2 + \gamma_r^2 = 1 \qquad \alpha_t^2 + \gamma_t^2 = 1 \tag{2.27}$$

Let us consider the general case of oblique incidence in presence of medium without absorption. The use of boundary conditions results in complex and challenging formulas for the vector amplitudes of the transmitted and reflected waves for any general direction of the vector amplitude of the incident wave. Two incident wave orientations, nevertheless, result in computations that are very simple:

- the electric vector aligned in the plane of incidence (i.e., the xy plane of Figure 2.1), and this wave is known as *p-polarized* (p stands for parallel) or as *TM* (for *transverse magnetic*)
- the electric vector aligned normal to the plane of incidence (i.e., parallel to the y-axis in Figure 2.1); wave known, instead, as *s-polarized* (s derived from the German senkrecht) or *TE* (for *transverse electric*).

The transmitted and reflected vector amplitudes in each of these occurrences have the same directions as the incident wave. Therefore, any incoming wave with any polarization may be divided into two halves with these straightforward orientations. For each direction, the transmitted and reflected components may be computed independently and combined to provide the resultant.

It must be selected the different vector reference directions from which to compute any phase differences before moving on to the computation of the reflected and transmitted amplitudes. The conventions that it will be used are illustrated in Figure 2.2.

2.2.0.1 p-Polarized Light

In the case of p-Polarized Light we have that the electric and magnetic component are parallel the boundary and continuous through it:

$$\boldsymbol{E}_i \cos \vartheta_0 + \boldsymbol{E}_r \cos \vartheta_0 = \boldsymbol{E}_t \cos \vartheta_1 \tag{2.28}$$

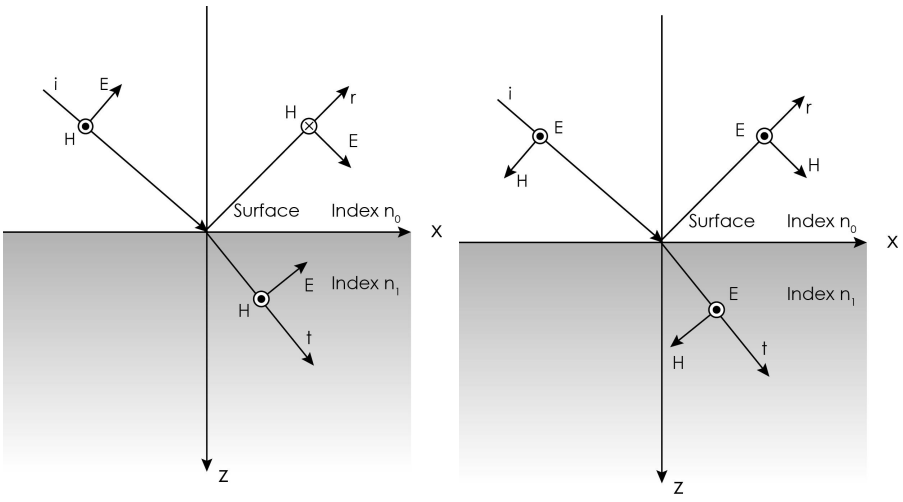

Figure 2.2: (a) Electric and magnetic vectors (positive directions) for p-polarized light (TM waves). (b) Electric and magnetic vectors (positive directions) for s-polarized light (TE waves).

moreover, being $\boldsymbol{H} = y\boldsymbol{E}$

$$y_0 \boldsymbol{E}_i - y_0 \boldsymbol{E}_r = y_1 \boldsymbol{E}_t \tag{2.29}$$

The amplitude reflection and transmission coefficients, denoted by ρ and τ respectively, are

$$\rho = \frac{\boldsymbol{E}_r}{\boldsymbol{E}_i} \tag{2.30}$$

$$\tau = \frac{\boldsymbol{E}_t}{\boldsymbol{E}_i} \tag{2.31}$$

Because the irradiances measured along the wave's propagation path have been computed and the transmitted wave is slanted at a different angle than the incident wave, adopting these definitions will require rejecting the $R + T = 1$ rule. Therefore, the energy flow components that are normal to the boundary were employed. The *tangential components* of the **E** and **H** vectors, which are used in these computations, are then parallel to the border. It is suitable to utilize it while discussing the wave amplitudes because

they are the ones that directly cross the boundary. Be aware that when employing limited beams, such as the output from a laser, reflectance and transmittance described for infinite plane waves in terms of normal flows of irradiance are completely compatible with reflectance and transmittance calculated in terms of the ratios of total beam power. Note also that the Fresnel coefficients are the amplitude coefficients, and that the conventional method in other branches of optics is to employ the whole components of **E** and **H** in amplitude expressions. It is practical to use unique symbols to represent the tangential components –$\mathcal{E}$ and $\mathcal{H}$. Then we can write

$$\boldsymbol{\mathcal{E}}_i = \boldsymbol{E}_i \cos\vartheta_0 \qquad \boldsymbol{\mathcal{H}}_i = \boldsymbol{H}_i = y_0 \boldsymbol{E}_i = \frac{y_0}{\cos\vartheta_0}\boldsymbol{\mathcal{E}}_i \tag{2.32}$$

$$\boldsymbol{\mathcal{E}}_r = \boldsymbol{E}_r \cos\vartheta_0 \qquad \boldsymbol{\mathcal{H}}_r = \frac{y_0}{\cos\vartheta_0}\boldsymbol{\mathcal{E}}_r \tag{2.33}$$

$$\boldsymbol{\mathcal{E}}_t = \boldsymbol{E}_t \cos\vartheta_1 \qquad \boldsymbol{\mathcal{H}}_t = \frac{y_1}{\cos\vartheta_1}\boldsymbol{\mathcal{E}}_t \tag{2.34}$$

These vectors have the exact same orientations as when light is incident normally.

Then, the equations (2.28) and (2.29) may be expressed as follows.

$$\boldsymbol{\mathcal{E}}_i + \boldsymbol{\mathcal{E}}_r = \boldsymbol{\mathcal{E}}_t \tag{2.35}$$

$$\frac{y_0}{\cos\vartheta_0}\boldsymbol{\mathcal{E}}_i + \frac{y_0}{\cos\vartheta_0}\boldsymbol{\mathcal{E}}_r = \frac{y_1}{\cos\vartheta_1}\boldsymbol{\mathcal{E}}_t \tag{2.36}$$

i.e.,

$$\rho_p = \frac{\boldsymbol{\mathcal{E}}_r}{\boldsymbol{\mathcal{E}}_i} = \left(\frac{y_0}{\cos\vartheta_0} - \frac{y_1}{\cos\vartheta_1}\right) / \left(\frac{y_0}{\cos\vartheta_0} + \frac{y_1}{\cos\vartheta_1}\right) \tag{2.37}$$

$$\tau_p = \frac{\boldsymbol{\mathcal{E}}_t}{\boldsymbol{\mathcal{E}}_i} = \left(\frac{2y_0}{\cos\vartheta_0}\right) / \left(\frac{y_0}{\cos\vartheta_0} + \frac{y_1}{\cos\vartheta_1}\right) \tag{2.38}$$

Since the boundary has no thickness, neither energy can be added to nor taken away from the various waves, but the total

tangential components of the electric and magnetic fields are continuous across it. The Poynting vector will be continuous across the boundary on both cases, allowing to write:

$$net\ irradiance = Re\left[\frac{1}{2}\left(\boldsymbol{\mathcal{E}}_i + \boldsymbol{\mathcal{E}}_r\right)\left(y_0\boldsymbol{\mathcal{E}}_i - y_0\boldsymbol{\mathcal{E}}_r\right)^*\right] = Re\left[\frac{1}{2}\boldsymbol{\mathcal{E}}_i\left(y_1\boldsymbol{\mathcal{E}}_t\right)^*\right] \tag{2.39}$$

Now

$$\boldsymbol{\mathcal{E}}_r = \rho\boldsymbol{\mathcal{E}}_i$$

and

$$\boldsymbol{\mathcal{E}}_t = \tau\boldsymbol{\mathcal{E}}_i$$

i.e.,

$$net\ irradiance = \frac{1}{2}y_0\mathcal{E}_i\mathcal{E}_i^*\left(1-\rho^2\right) = \frac{1}{2}y_0\mathcal{E}_i\mathcal{E}_i^*\left(y_1/y_0\right)\tau^2 \tag{2.40}$$

where $\frac{1}{2}y_0\mathcal{E}_i\mathcal{E}_i^*$ is the irradiance of the incident beam I_i, $\rho^2\frac{1}{2}y_0\mathcal{E}_i\mathcal{E}_i^* = \rho^2 I_i$ is the irradiance of the reflected beam I_r and $(y_1/y_0)\times\tau^2\frac{1}{2}y_0\mathcal{E}_i\mathcal{E}_i^* = (y_1/y_0)\,\tau^2 I_i$ is the irradiance of the trasmitted beam I_t.

The ratio of reflected and incident irradiances is known as the reflectance R, while the ratio of transmitted and incident irradiances is known as the transmittance T:

$$T = \frac{I_t}{I_i} = \frac{y_1}{y_0}\tau^2$$

$$R = \frac{I_r}{I_i} = \rho^2 \tag{2.41}$$

So, in the case of p-polarized light

$$T_p = \frac{y_1}{y_0}\tau_p^2 = \left[\left(\frac{y_0}{\cos\vartheta_0} - \frac{y_1}{\cos\vartheta_1}\right)/\left(\frac{y_0}{\cos\vartheta_0} + \frac{y_1}{\cos\vartheta_1}\right)\right]^2$$

$$R_p = \rho_p^2 = \left(\frac{4y_0y_1}{\cos\vartheta_0}\right)/\left(\frac{y_0}{\cos\vartheta_0} + \frac{y_1}{\cos\vartheta_1}\right)^2 \tag{2.42}$$

From Equation 2.40 and 2.42

$$(1 - R) = T \tag{2.43}$$

The energy flow into the second medium is merely the difference between the incident and reflected irradiances when there is no absorption. This equations describe the concept of separating the irradiances into incident, reflected, and transmitted irradiances, which may be viewed as independent waves.

2.2.0.2 s-Polarized Light

In the case of s-polarization, the components of the waves parallel to the boundary have amplitudes that are

$$\boldsymbol{\mathcal{E}}_i = \boldsymbol{E}_i \qquad \boldsymbol{\mathcal{H}}_i = \boldsymbol{H}_i \cos\vartheta_0 = (y_0 \cos\vartheta_0)\,\boldsymbol{\mathcal{E}}_i$$

$$\boldsymbol{\mathcal{E}}_r = \boldsymbol{E}_r \qquad \boldsymbol{\mathcal{H}}_r = \boldsymbol{H}_i \cos\vartheta_0 = (y_0 \cos\vartheta_0)\,\boldsymbol{\mathcal{E}}_r$$

$$\boldsymbol{\mathcal{E}}_t = \boldsymbol{E}_t \qquad \boldsymbol{\mathcal{H}}_t = (y_1 \cos\vartheta_1)\,\boldsymbol{\mathcal{E}}_t$$

and the tangential components are arranged as they would be for normally incident light. A similar study so results in

$$\rho_s = \frac{\boldsymbol{\mathcal{E}}_r}{\boldsymbol{\mathcal{E}}_i} = (y_0 \cos\vartheta_0 - y_1 \cos\vartheta_1) \,/\, (y_0 \cos\vartheta_0 + y_1 \cos\vartheta_1) \tag{2.44}$$

$$\tau_s = \frac{\boldsymbol{\mathcal{E}}_t}{\boldsymbol{\mathcal{E}}_i} = (2y_0 \cos\vartheta_0) \,/\, (y_0 \cos\vartheta_0 + y_1 \cos\vartheta_1) \tag{2.45}$$

$$R_s = \left[(y_0 \cos\vartheta_0 - y_1 \cos\vartheta_1) \,/\, (y_0 \cos\vartheta_0 + y_1 \cos\vartheta_1)\right]^2 \tag{2.46}$$

$$T_s = (4y_0 \cos\vartheta_0 y_1 \cos\vartheta_1) \,/\, (y_0 \cos\vartheta_0 + y_1 \cos\vartheta_1)^2 \tag{2.47}$$

where the $(R + T = 1)$ rule is respected.

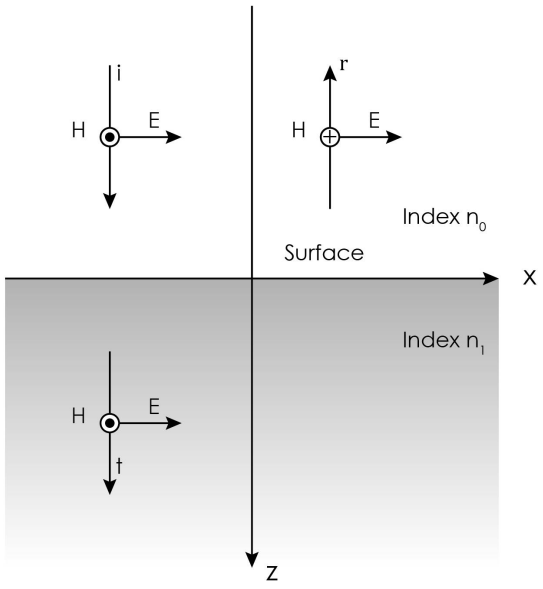

Figure 2.3: Electric and magnetic vectors (positive directions) for reflection and transmission at an interface at normal incidence.

2.2.1 Normal Incidence

It is possible to simplify initial discussion considering the normal incidence and letting the incident wave be a linearly polarized plane harmonic wave. The coordinate axes are shown in Figure 2.3. The xy plane is the plane of the boundary. The incident wave is propagating along the z-axis with the positive direction of the $\boldsymbol{E}$ vector along the x-axis. Then, the positive direction of the $\boldsymbol{H}$ vector will be the y-axis. It is clear that the only waves that satisfy the boundary conditions are linearly polarized in the same plane as the incident wave.

When two waves are moving in the same direction, a phase difference between them is instantly significant. We assign $z = 0$ - the boundary- as the reference point for calculations of the relative phase of beams that are traveling in opposing directions. The magnetic vector will have a positive direction along the y-axis for incident and transmitted waves and a negative direction along the y-axis for reflected waves since we specify the positive direction of

E along the x-axis for all the concerned beams.

It is now considered the amplitudes, including any phase changes, in the boundary conditions because the conditions on the phase factors being already satisfied:

- Electric vector continous across the boundary

$$\boldsymbol{E}_i + \boldsymbol{E}_r = \boldsymbol{E}_t \tag{2.48}$$

- Magnetic vector continous across the boundary

$$\boldsymbol{H}_i - \boldsymbol{H}_r = \boldsymbol{H}_t \tag{2.49}$$

Through the characteristic admittance the relationship between magnetic and electric field is

$$y_0\boldsymbol{E}_i - y_0\boldsymbol{E}_r = y_1\boldsymbol{E}_t \tag{2.50}$$

therefore, being also $y = nY_0$, the *amplitude reflection* and *transmission coefficients* are

$$\rho = \frac{\boldsymbol{E}_r}{\boldsymbol{E}_i} = \frac{y_0 - y_1}{y_0 + y_1} = \frac{n_0 - n_1}{n_0 + n_1} \tag{2.51}$$

$$\tau = \frac{\boldsymbol{E}_t}{\boldsymbol{E}_i} = \frac{2y_0}{y_0 + y_1} = \frac{2n_0}{n_0 + n_1} \tag{2.52}$$

The reflectance R and the transmittance T are

$$R = \left(\frac{y_0 - y_1}{y_0 + y_1}\right)^2 = \left(\frac{n_0 - n_1}{n_0 + n_1}\right)^2 \tag{2.53}$$

$$T = \frac{4y_0y_1}{(y_0 + y_1)^2} = \frac{4n_0n_1}{(n_0 + n_1)} \tag{2.54}$$

Also in this case the relation $(1 - R) = T$ is true and the irradiance can be splitted into into incident, reflected and trasmitted irradiances, which being handled as separated waves.

2.2.2 Optical Admittance - Brewster Angle

We introduced a slanted optical admittance, η, which links $\boldsymbol{\mathcal{E}}$ and $\boldsymbol{\mathcal{H}}$ as a result of finding it convenient to work with $\boldsymbol{\mathcal{E}}$ and $\boldsymbol{\mathcal{H}}$, the components of E and H parallel to the boundary, in the prior approach.

$$\eta = \frac{\boldsymbol{\mathcal{H}}}{\boldsymbol{\mathcal{E}}} \tag{2.55}$$

At oblique incidence

$$\eta_p = \frac{y}{\cos\vartheta} = \frac{nY_0}{\cos\vartheta} \tag{2.56}$$

$$\eta_s = y\cos\vartheta = nY_0\cos\vartheta \tag{2.57}$$

where the ϑ and y are those appropriate to the particular medium and must be used the Snell's law for the calculation. While at normal incidence

$$\eta = y = nY_0 \tag{2.58}$$

In every instance, we may write

$$\begin{aligned} \rho &= \left(\frac{\eta_0 - \eta_1}{\eta_0 + \eta_1}\right) \\ \tau &= \left(\frac{2\eta_0}{\eta_0 + \eta_1}\right) \end{aligned} \tag{2.59}$$

$$\begin{aligned} R &= \left(\frac{\eta_0 - \eta_1}{\eta_0 + \eta_1}\right)^2 \\ T &= \frac{4\eta_0\eta_1}{(\eta_0 + \eta_1)^2} \end{aligned} \tag{2.60}$$

The variation in reflectance of single boundary between extended media may be computed using these formulas. Examples of the angular spectrum of reflectance are illustrated in Figure 2.4. As there is no material absorption in this instance, it is clear that at a certain angle, the Brewster angle, the reflectance for p-polarized light (TM) goes to zero. The Brewster angle is one particular

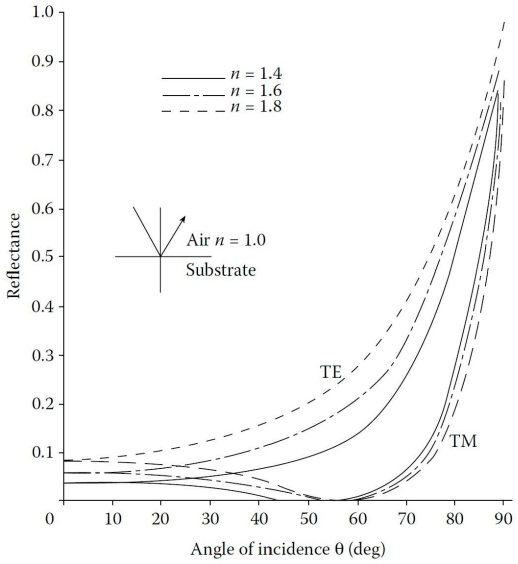

Figure 2.4: Incidence reflectance angular spectrum for various values of refractive index.

angle that has some significance. The windows of a cell must have almost negligible reflection loss in various applications. A plate inclined at the Brewster angle will work well when it is possible to arrange for the light to be linearly polarized. In this case it is also defined as the polarization angle, since, in the case of a compound wave, only the perpendicular component will be reflected.

The following may be used to obtain the Brewster angle expression. For the definition of p-reflectance, from Equation 2.42, and considering only the numerator, we will have that this will vanish only if:

$$\frac{y_0}{\cos\vartheta_0} = \frac{y_1}{\cos\vartheta_1}$$

that is

$$\frac{n_0 Y_0}{\cos\vartheta_0} = \frac{n_1 Y_0}{\cos\vartheta_1}$$

From which, taking into account Snell's law, that gives another relationship between ϑ_0 and ϑ_1

$$n_0 \sin\vartheta_0 = n_1 \sin\vartheta_1$$

we can obtain the value of this particular angle of incidence

$$\tan \vartheta_0 = n_1/n_0 \tag{2.61}$$

Observe that this derivation depends on the constituent parameters of the two media by the relationship $y = nY_0$.

In the case of absorbing media we will have that the Brewster angle will be complex and the reflection coefficient will never vanish for any real angle of incidence, however presenting a minimum in correspondence with that angle that is defined Pseudo-Brewster angle.

2.2.3 Incidence in Absorbing Media

2.2.3.1 Oblique Incidence in Absorbing Media

In the case of oblique incidence in absorbing media itb has been restricted this to an absorbent second medium and a transparent incident medium. The reason of this choice will be clear in the next section. The phase factors might be written as follows in order to achieve the first aim of ensuring consistency:

- Incident wave: $\exp\{\imath\left[\omega t - (2\pi n_0/\lambda)\left(x\sin\vartheta_0 + z\cos\vartheta_0\right)\right]\}$
- Reflected wave: $\exp\{\imath\left[\omega t - (2\pi n_0/\lambda)\left(x\sin\vartheta_0 - z\cos\vartheta_0\right)\right]\}$
- Transmitted wave: $\exp\{\imath\left[\omega t - (2\pi\left\{n_1 - ik_1\right\}/\lambda)\left(\alpha x + \gamma z\right)\right]\}$

where α and γ in the trasmitted phase factors are the only unknows. The phase factors must be indentically equal for all x and t with $z = 0$. This implies

$$\alpha = \frac{n_0 \sin\vartheta_0}{(n_1 - ik_1)} \tag{2.62}$$

and, since $\alpha^2 + \gamma^2 = 1$

$$\gamma = \left(1 - \alpha^2\right)^{1/2}$$

There are two solutions to this equation and we note that are required $(n_1 - ik_1)\,\alpha$ and $(n_1 - ik_1)\,\gamma$

$$(n_1 - ik_1)\,\gamma = \left[(n_1 - ik_1)^2 - n_0^2 \sin^2 \vartheta_0\right]^{1/2}$$
$$= \left[n_1 - ik_1 - n_0^2 \sin^2 \vartheta_0 - i2n_1k_1\right]^{1/2} \qquad (2.63)$$

The solution of the square roots can be found in the second quadrant (of the form -a + ib) and the fourth quadrant (of the form a - ib). When these values are replaced into the phase factors, it is possible to see that the fourth quadrant solution – which results in an exponential decay of amplitude with a z value and a shift in phase – must be right. A wave going in the opposite direction would be implied by the second quadrant solution, which would result in an increase with z and a change in the wrong sense's phase. The response for the fourth quadrant agrees with the solution for the case of media without absorption. Therefore, the phase factor of the transmitted component has the following form

$$exp\left\{i\left[\omega t - (2\pi n_0 \sin \vartheta_0 x/\lambda) - (2\pi/\lambda)\,(a - ib)\,z\right]\right\}$$
$$= exp\left(-2\pi bz/\lambda\right) exp\left\{i\left[\omega t - (2\pi n_0 \sin \vartheta_0 x/\lambda) - (2\pi az/\lambda)\right]\right\}$$

where

$$(a - ib) = \left[n_1 - ik_1 - n_0^2 \sin^2 \vartheta_0 - i2n_1k_1\right]^{1/2}$$

Any wave that has this kind of phase factor is said to be inhomogeneous. The z-axis is where the exponential amplitude decay occurs, and the direction cosines, which identify the propagation direction in terms of phase, may be derived from:

$$(2\pi n_0 \sin \vartheta_0 x/\lambda) + (2\pi az/\lambda)$$

At this point, it is important to keep in mind that the formulation of the ase without absorption situation applies just as well to absorbing medium as long as we take the chance of complex angles into account:

$$(n_1 - ik_1)\sin\vartheta_1 = n_0 \sin\vartheta_0$$
$$\alpha = \sin\vartheta_1$$
$$\gamma = \cos\vartheta_1$$
$$(a - ib) = (n_1 - ik_1)\cos\vartheta_1$$

We consider the effects of an inhomogeneous wave in the amplitude computation together with the calculation of the tilting admittance associated with this type of wave. The phase factor contains the x, y, and t variations of the wave, therefore could write:

$$\nabla\times = \left(\frac{\partial}{\partial x}\boldsymbol{i} + \frac{\partial}{\partial x}\boldsymbol{j} + \frac{\partial}{\partial x}\boldsymbol{k}\right)\times$$
$$= \left(-i\frac{2\pi\,(n - ik)}{\lambda}\alpha\boldsymbol{i} - i\frac{2\pi\,(n - ik)}{\lambda}\gamma\boldsymbol{k}\right)\times$$

and

$$\frac{\partial}{\partial t} = i\omega$$

where $\boldsymbol{k}$, which should not be confused with the extinction coefficient k, is a unit vector in the z direction. Since the H vector for p-waves is parallel to the boundary in the y direction, $H = \mathcal{H}_y\boldsymbol{j}$. Then, $\mathcal{E}_x\boldsymbol{i}$, the component of E parallel to the border, will be in the x direction.

$$\nabla \times \boldsymbol{H} = \sigma\boldsymbol{E} + \varepsilon\frac{\partial}{\partial t}\boldsymbol{E}$$
$$= (\sigma + i\omega\varepsilon)\,\boldsymbol{E}$$
$$= \frac{i\omega\,(n - ik)^2}{c^2\mu}\boldsymbol{E}$$

$\nabla \times \boldsymbol{H}$'s tangential component is now in the x direction, resulting in

$$-i\frac{2\pi\,(n-ik)}{\lambda}\gamma\,(\boldsymbol{k}\times\boldsymbol{j})\,\boldsymbol{\mathcal{H}}_y = i\frac{\omega\,(n-ik)^2}{c^2\mu}\boldsymbol{\mathcal{E}}_x\boldsymbol{i}$$

but

$$-\,(\boldsymbol{k}\times\boldsymbol{j}) = \boldsymbol{i}$$

so that

$$\eta_p = \frac{\boldsymbol{\mathcal{H}}_y}{\boldsymbol{\mathcal{E}}_x} = \frac{\omega\,(n-ik)\,\lambda}{2\pi c^2\mu\gamma} = \frac{(n-ik)}{c\mu\gamma}$$
$$= \frac{(n-ik)\,Y_0}{\gamma} = \frac{y}{\gamma}$$

For the s-waves, it is used

$$\nabla\times\boldsymbol{E} = -\frac{\partial}{\partial t}\boldsymbol{B} = -\mu\frac{\partial}{\partial t}\boldsymbol{H}$$

E is now along the y-axis, then

$$\eta_s = \frac{\boldsymbol{\mathcal{H}}_x}{\boldsymbol{\mathcal{E}}_y} = (n-ik)\,Y_0\gamma = y\gamma \tag{2.64}$$

Now if ϑ is allowed to be complex, γ can be characterized as $\cos\vartheta$ and so

$$\begin{aligned}\eta_p &= y/\cos\vartheta\\ \eta_s &= y\cos\vartheta\end{aligned} \tag{2.65}$$

Otherwise, it is possible to employ the expressions in Equations 2.63 and 2.64 with $y = (n-ik)Y_0$ to give

$$\eta_s = Y_0\left[n_1^2 - k_1^2 - n_0^2\sin^2\vartheta_0 - i2n_1k_1\right]^{1/2} \tag{2.66}$$

The fourt quadrant is the proper solution, and then

$$\eta_p = \frac{y^2}{\eta_s} \tag{2.67}$$

The second version does not have any quadrant-related issues. Following that, the amplitude and irradiance coefficients are:

$$\rho = \frac{\eta_0 - \eta_1}{\eta_0 + \eta_1} \tag{2.68}$$

$$\tau = \frac{2\eta_0}{\eta_0 + \eta_1} \tag{2.69}$$

$$R = \left(\frac{\eta_0 - \eta_1}{\eta_0 + \eta_1}\right)\left(\frac{\eta_0 - \eta_1}{\eta_0 + \eta_1}\right)^* \tag{2.70}$$

$$T = \frac{4\eta_0 Re(\eta_1)}{(\eta_0 + \eta_1)(\eta_0 + \eta_1)^*} \tag{2.71}$$

And these statements also hold true for media without absorption.

2.2.3.2 Normal Incidence in Absorbing Media

In the presence of absorption in the case of normal incidence it should be written

$$\begin{aligned} \sqrt{\varepsilon_0} &= n_0 - ik_0 \\ \sqrt{\varepsilon_1} &= n_1 - ik_1 \\ y_0 &= (n_0 - ik_0)\, Y_0 \\ y_1 &= (n_1 - ik_1)\, Y_0 \end{aligned}$$

The analysis is the same of that for absorption-free media and the boundaries are as before, then we obtain these expressions for the amplitude coefficients

$$\rho = \frac{y_0 - y_1}{y_0 + y_1} = \frac{(n_0 - ik_0)\, Y_0 - (n_1 - ik_1)\, Y_0}{(n_0 - ik_0)\, Y_0 + (n_1 - ik_1)\, Y_0} = \frac{(n_0 - n_1) - i\,(k_0 - k_1)}{(n_0 + n_1) - i\,(k_0 + k_1)} \tag{2.72}$$

$$\tau = \frac{\boldsymbol{E}_t}{\boldsymbol{E}_i} = \frac{2y_0}{y_0 + y_1} = \frac{2\,(n_0 - ik_0)\, Y_0}{(n_0 - ik_0)\, Y_0 + (n_1 - ik_1)\, Y_0} = \frac{2\,(n_0 - ik_0)}{(n_0 + n_1) - i\,(k_0 + k_1)} \tag{2.73}$$

To obtain the reflectance and transmittance in each medium it has been computed and equated the Poynting vector at the boundary. The resulting electric and magnetic fields in the incident medium are

$$\boldsymbol{E}_i + \boldsymbol{E}_r = \boldsymbol{E}_t \left(1 - \rho\right)$$

and

$$\boldsymbol{H}_i - \boldsymbol{H}_r = y_0 \left(1 - \rho\right) \boldsymbol{H}_t$$

respectively, and in the second medium the fields are $\tau \boldsymbol{E}_i$ and $y_1 \tau \boldsymbol{E}_i$ respectively. On each side of the boundary, the net irradiance is

$$I = Re \left\{ \frac{1}{2} \left[\boldsymbol{E}_i \left(1 + \rho\right) \right] \left[y_0^* \left(1 - \rho^*\right) \boldsymbol{E}_i^* \right] \right\} \tag{2.74}$$

for the medium 0, and

$$I = Re \left\{ \frac{1}{2} \left[\tau \boldsymbol{E}_i \right] \left[y_1^* \tau^* \boldsymbol{E}_i^* \right] \right\} \tag{2.75}$$

for the medium 1. Then, equaling:

i.e.,

$$I_i - R I_i + \frac{1}{2} Re \left[y_0^* (\rho - \rho^*) \right] \boldsymbol{E}_i \boldsymbol{E}_i^* = T I_i \tag{2.76}$$

Since $(\rho - \rho^*)$ is imaginary if y_0 is real, the third component in Equation 2.76 equals zero. The incident, reflected, and transmitted irradiances are then comprised of the additional terms. When y_0 is complex, the imaginary components of y_0 and $(\rho - \rho^*)$ will be mixed to give a real result that will suggest that $T + R \neq 1$. Since the boundary has zero thickness, it cannot absorb or provide energy to the waves, so the radiations involved in the analysis are exactly those at the boundary. When calculating energy transmission, one must account for the coupling between the incident and reflected fields, which only happens in an absorbing material.

Therefore, it is wrong to assume that the irradiances can be separated into distinct incident, reflected, and transmitted irradiances; yet, the equations for the amplitude coefficients are entirely accurate. The incident medium needs to be sufficiently devoid of absorption in order for the measurement error to be negligibly

minimal. The incident media will never be significantly absorbing, even though we will undoubtedly deal with absorbing media in thin-film assemblies. It won't be a major lack of generality if we assume that our incident media are not absorbing. Then, in order to have accurate reflectance calculations, we must make sure that they are performed in a transparent material.

$$R = \left(\frac{y_0 - y_1}{y_0 + y_1}\right)\left(\frac{y_0 - y_1}{y_0 + y_1}\right)^* \tag{2.77}$$

$$T = \frac{4y_0 Re(y_1)}{(y_0 + y_1)(y_0 - y_1)^*} \tag{2.78}$$

where y_0 is real. By not defining reflectance until the incident media is sufficiently free of gain or absorption, it has been avoided the issue related to its definition in a medium with complicated properties. However, without a definition of reflectance, it is struggled to understand what antireflection in the context of antireflection coating means. The decrease of reflectance is the typical goal of an antireflection coating. An antireflection coating is defined as one that enhances transmittance and, in the ideal scenario, maximizes it since, in many cases, the goal of the reflectance reduction is the commensurate increase in transmittance. However, in order to do that, it must be first clarified what is meant by transmittance. Even if the emerging medium is absorbing, there is no issue with the measurement of irradiance at that side of the system. The incident irradiance makes things harder. If the transmitting structure were be replaced by an icident medium material unlimited extended, this might be defined as the irradiance. The ratio of these two quantities will therefore be the transmittance. i.e,

$$I_{inc} = \frac{1}{2} Re(y_0) \boldsymbol{E}_i \boldsymbol{E}_i^* \tag{2.79}$$

and then

$$T = \frac{\frac{1}{2} Re(y_1) \boldsymbol{E}_t \boldsymbol{E}_t^*}{\frac{1}{2} Re(y_0) \boldsymbol{E}_i \boldsymbol{E}_i^*} \tag{2.80}$$

The Equation 2.76 that is totally compatible with this

$$T = 1 - \rho\rho^* + \frac{Re\left[y_0^*\left(\rho - \rho^*\right)\right]}{Re(y_0)} \tag{2.81}$$

an alternative, using $\boldsymbol{E}_t = \dfrac{2y_0}{(y_0 + y_1)}\boldsymbol{E}_i$, we have

$$T = \frac{4y_0 y_0^* Re(y_1)}{Re(y_0)\left[\left(y_0 + y_1\right)\left(y_0 - y_1\right)^*\right]} \tag{2.82}$$

Let's now coat a dielectric film to the surface to provide the admittance $Y = \alpha + i\beta$. Since the emerging irradiance must also be the thin-film system's net irradiance in the absence of absorption,

$$T = \frac{4y_0 y_0^* Re(Y)}{Re(y_0)\left[\left(y_0 + Y\right)\left(y_0 - Y\right)^*\right]} = \frac{4\alpha\left(n_0^2 + k_0^2\right)}{n_0\left[\left(n_0 + \alpha\right)^2\left(k_0 - \beta\right)^2\right]} \tag{2.83}$$

and T is easily shown to be maximal when

$$Y = \alpha + i\beta = n_0 + ik_0 = \left(n_0 + ik_0\right)^* \tag{2.84}$$

Therefore, the complex conjugate of the incident admittance should be the matching admittance. The transmittance changes when this perfect matching occurs.

$$T = \left(1 + \frac{k_0^2}{n_0^2}\right) \tag{2.85}$$

And because of the definition of transmittance, this is more than unity. The impact is fairly minimal since the irradiance decreases by a factor of around $4\pi k_0$ in a distance of one wavelength, which is somewhat bigger than any typical value of k_0^2/n_0^2. It is a cyclical fluctuation in the rate of irradiance decrease and is brought on by the existence of the interface. If the coating is made to match $n_0 - ik_0$ rather than its complex conjugate, it should be noted that the transmittance is unity. When reversed, a dielectric coating that changes an admittance of y_1 to y_0^* likewise changes an admittance of y_0 to y_1^* in the exact same way.

Thus, the optimum coating to give highest transmittance will be the same in both directions. This implies that an absorbing substrate in identical dielectric incident and emergent media should

have exactly similar antireflection coatings on both front and rear surfaces.

A number of beams are merged either coherently or incoherently in order to calculate the characteristics of a coated slice of material. The typical interference calculation applies to the coherent scenario. For a multiple beam computation for the incoherent scenario, an estimate of the reflected beam is required. According to these estimates, the absorption is not high enough to fully remove a beam that supports two traversals of the system. This suggests that there will be very little absorption, $4\pi k_0$ will be very little, over the length of one wavelength. The effect under consideration can be as large as k_0^2/n_0^2, although this will still be less important.

A phase jumble that cancels out the impact of an incoherent computation is required for it to be suitable. For the sake of this explanation, it may be assumed that a shifting of the reflecting surface across the aperture is what causes the jumbling. An average of the extra term is appropriate at any exactly plane surface that may be used as a reference, and this will be zero because ρ will have a phase that varies across the four quadrants. The variation of the extra term in Equation 2.84 is stalled for its phase to the reflecting surface. Therefore, the reflectance may be calculated for multiple beam using the simple formula $\rho\rho^*$. The absorption will be extremely deep and most likely sufficient to make the impact of the multiple beam automatically insignificant where k_0^2/n_0^2 is substantial.

2.3 The Reflectance of a Thin Film

A thin, planar parallel layer of material covering the surface of a substrate results in a straightforward extension of the aforementioned study. A number of beams will be generated at two (or more) interfaces by sequential reflections, and the total of these beams will define the characteristics of the film. We can recognize two different cases that we can describe as *coherent* or *incoherent*: in the coherent case full interference effects can be detected in the reflected or transmitted light and the film is defined *thin*; when no

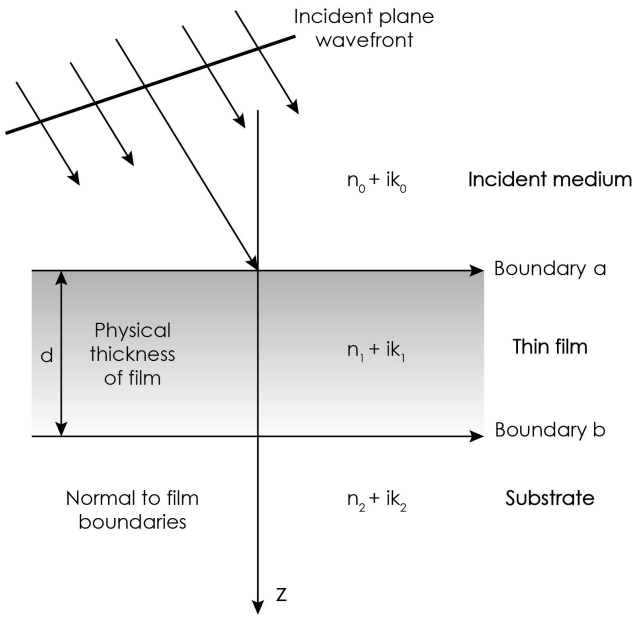

Figure 2.5: Plane wave incident on a thin film.

interference effects can be detected, the film is described as *thick* and the case is described as incoherent. The coherent and incoherent cases depend on the presence or absence of a constant phase relationship between the various beams, and this will depend on the nature of the light and the receiver and on the quality of the film. Depending on the lighting, the same film might look thick or thin. In most cases, the substrates supporting the films may be thought of as thick, whilst the films themselves can be viewed as thin. Figure 2.5 provides an illustration of the structure. Now, it is used the sign + (positive-going) to represent waves traveling in the direction of incidence, and the symbol - to represent waves traveling in the opposite direction (i.e., negative-going).

The simple boundary we previously mentioned may be applied to the interfaces between the film and the incident medium and the substrate, indicated by the symbols a and b. We take into account the tangential fields' components. Since the substrate lacks a negative-going wave, the waves in the film can be combined to create a single positive-going wave and a single negative-going wave. Therefore, the tangential components of $\boldsymbol{E}$ and $\boldsymbol{H}$ at this

interface are:

$$\boldsymbol{\mathcal{E}}_b = \boldsymbol{\mathcal{E}}^+_{1b} + \boldsymbol{\mathcal{E}}^-_{1b}$$
$$\boldsymbol{\mathcal{H}}_b = \eta_1 \boldsymbol{\mathcal{E}}^+_{1b} - \eta_1 \boldsymbol{\mathcal{E}}^-_{1b}$$

Here $\boldsymbol{\mathcal{E}}_b$ and $\boldsymbol{\mathcal{H}}_b$ represent the resultants and the common phase factors are neglected . Hence

$$\boldsymbol{\mathcal{E}}^+_{1b} = \frac{1}{2}\left(\boldsymbol{\mathcal{H}}_b/\eta_1 + \boldsymbol{\mathcal{E}}_b\right) \tag{2.86}$$

$$\boldsymbol{\mathcal{E}}^-_{1b} = \frac{1}{2}\left(-\boldsymbol{\mathcal{H}}_b/\eta_1 + \boldsymbol{\mathcal{E}}_b\right) \tag{2.87}$$

$$\boldsymbol{\mathcal{H}}^+_{1b} = \eta_1 \boldsymbol{\mathcal{E}}^+_{1b} = \frac{1}{2}\left(\boldsymbol{\mathcal{H}}_b + \eta_1 \boldsymbol{\mathcal{E}}_b\right) \tag{2.88}$$

$$\boldsymbol{\mathcal{H}}^-_{1b} = -\eta_1 \boldsymbol{\mathcal{E}}^+_{1b} = \frac{1}{2}\left(\boldsymbol{\mathcal{H}}_b - \eta_1 \boldsymbol{\mathcal{E}}_b\right) \tag{2.89}$$

The fields at the other interface a at the same instant and at a point with identical x and y coordinates is determined by a shift of the phase factors of the waves to allow the shifting in the z coordinate from 0 to $-d$. The phase factor of the positive-going wave will be multiplied by $exp(i\delta)$, while the negative-going phase factor will be multiplied by $-exp(i\delta)$. Here

$$\delta = 2\pi\left(n_1 - ik_1\right) d \cos\vartheta_1/\lambda$$

with ϑ_1 complex. This procedure is valid when the film is thin. Using the Equations (2.86) through (2.89) we have that the values of E and H at the interface are

$$\boldsymbol{\mathcal{E}}^+_{1a} = \boldsymbol{\mathcal{E}}^+_{1b} e^{i\delta} = \frac{1}{2}\left(\boldsymbol{\mathcal{H}}_b/\eta_1 + \boldsymbol{\mathcal{E}}_b\right) e^{i\delta} \tag{2.90}$$

$$\boldsymbol{\mathcal{E}}^-_{1a} = \boldsymbol{\mathcal{E}}^-_{1b} e^{i\delta} = \frac{1}{2}\left(-\boldsymbol{\mathcal{H}}_b/\eta_1 + \boldsymbol{\mathcal{E}}_b\right) e^{-i\delta} \tag{2.91}$$

$$\boldsymbol{\mathcal{H}}^+_{1a} = \boldsymbol{\mathcal{H}}^+_{1b} e^{i\delta} = \frac{1}{2}\left(\boldsymbol{\mathcal{H}}_b + \eta_1 \boldsymbol{\mathcal{E}}_b\right) e^{i\delta} \tag{2.92}$$

$$\boldsymbol{\mathcal{H}}^-_{1a} = \boldsymbol{\mathcal{H}}^-_{1a} e^{-i\delta} = \frac{1}{2}\left(\boldsymbol{\mathcal{H}}_b - \eta_1 \boldsymbol{\mathcal{E}}_b\right) e^{-i\delta} \tag{2.93}$$

so that

$$\begin{aligned}\boldsymbol{\mathcal{E}}_a &= \boldsymbol{\mathcal{E}}_{1a}^{+} + \boldsymbol{\mathcal{E}}_{1a}^{-} \\ &= \boldsymbol{\mathcal{E}}_b \left(\frac{e^{i\delta} + e^{-i\delta}}{2} \right) + \boldsymbol{\mathcal{H}}_b \left(\frac{e^{i\delta} - e^{-i\delta}}{2\eta_1} \right) \\ &= \boldsymbol{\mathcal{E}}_b \cos\delta + \boldsymbol{\mathcal{H}}_b \frac{i \sin\delta}{\eta_1}\end{aligned}$$

$$\begin{aligned}\boldsymbol{\mathcal{H}}_a &= \boldsymbol{\mathcal{H}}_{1a}^{+} + \boldsymbol{\mathcal{H}}_{1a}^{-} \\ &= \boldsymbol{\mathcal{E}}_b \eta_1 \left(\frac{e^{i\delta} - e^{-i\delta}}{2} \right) + \boldsymbol{\mathcal{H}}_b \left(\frac{e^{i\delta} + e^{-i\delta}}{2} \right) \\ &= \boldsymbol{\mathcal{E}}_b i\eta_1 \sin\delta + \boldsymbol{\mathcal{H}}_b \cos\delta\end{aligned}$$

This equations can be written in matrix notation as

$$\begin{bmatrix} \boldsymbol{\mathcal{E}}_a \\ \boldsymbol{\mathcal{H}}_a \end{bmatrix} = \begin{bmatrix} \cos\delta & (i\sin\delta)/\eta_1 \\ i\eta_1 \sin\delta & \cos\delta \end{bmatrix} \begin{bmatrix} \boldsymbol{\mathcal{E}}_b \\ \boldsymbol{\mathcal{H}}_b \end{bmatrix} \tag{2.94}$$

with $Z_1 = \frac{1}{\eta_1}$.

The tangential components of $\boldsymbol{E}$ and $\boldsymbol{H}$ at the incident interface and the tangential components of $\boldsymbol{E}$ and $\boldsymbol{H}$ transmitted through the final interface are connected by this relationship, because the tangential components of $\boldsymbol{E}$ and $\boldsymbol{H}$ are continuous across a boundary and since there is only a positive-going wave in the substrate. The 2×2 matrix

$$\begin{bmatrix} \cos\delta & (i\sin\delta)/\eta_1 \\ i\eta_1 \sin\delta & \cos\delta \end{bmatrix} \tag{2.95}$$

is known as the *characteristic matrix* of the thin film.

As before, we define the input optical admittance of the assembly as

$$\mathcal{Y} = \boldsymbol{\mathcal{H}}_a / \boldsymbol{\mathcal{E}}_a \tag{2.96}$$

to find the reflectance of a simple interface between an incident

medium of admittance η_0 and a medium of admittance $\mathcal{Y}$, i.e.,

$$\begin{aligned} \rho &= \frac{\eta_0 - \mathcal{Y}}{\eta_0 + \mathcal{Y}} \\ R &= \left(\frac{\eta_0 - \mathcal{Y}}{\eta_0 + \mathcal{Y}}\right)\left(\frac{\eta_0 - \mathcal{Y}}{\eta_0 + \mathcal{Y}}\right)^* \end{aligned} \tag{2.97}$$

We can normalize Equation (2.94) by dividing through by $\boldsymbol{\mathcal{E}}_b$ to give the normalized electric and magnetic fields at the front interfaces, rispectively B and C, that are the quantities from which the properties of the thin-film system can be extracted, i.e.

$$\begin{bmatrix} \boldsymbol{\mathcal{E}}_a/\boldsymbol{\mathcal{E}}_b \\ \boldsymbol{\mathcal{H}}_a/\boldsymbol{\mathcal{H}}_b \end{bmatrix} = \begin{bmatrix} B \\ C \end{bmatrix} \begin{bmatrix} \cos\delta & (i\sin\delta)/\eta_1 \\ i\eta_1 \sin\delta & \cos\delta \end{bmatrix} \begin{bmatrix} 1 \\ \eta_2 \end{bmatrix} \tag{2.98}$$

and so

$$\mathcal{Y} = \frac{\boldsymbol{\mathcal{H}}_a}{\boldsymbol{\mathcal{E}}_a} = \frac{C}{B} = \frac{\eta_2 \cos\delta + i\eta_1 \sin\delta}{\cos\delta + i\left(\eta_2/\eta_1\right)\sin\delta} \tag{2.99}$$

The matrix $\begin{bmatrix} B \\ C \end{bmatrix}$ is referred to as the assembly's *characteristic matrix*.

2.4 The Reflectance of an Assembly of Thin Films

The single film from the previous section is combined with another film to create a new interface c, as shown in Figure 2.6, where the characteristic matrix of the film closest to the substrate is

$$\begin{bmatrix} \cos\delta_2 & (i\sin\delta_2)/\eta_2 \\ i\eta_2 \sin\delta_2 & \cos\delta_2 \end{bmatrix} \tag{2.100}$$

from the Equation (2.94)

$$\begin{bmatrix} \boldsymbol{\mathcal{E}}_b \\ \boldsymbol{\mathcal{H}}_b \end{bmatrix} = \begin{bmatrix} \cos\delta_2 & (i\sin\delta_2)/\eta_2 \\ i\eta_2 \sin\delta_2 & \cos\delta_2 \end{bmatrix} \begin{bmatrix} \boldsymbol{\mathcal{E}}_c \\ \boldsymbol{\mathcal{H}}_c \end{bmatrix}$$

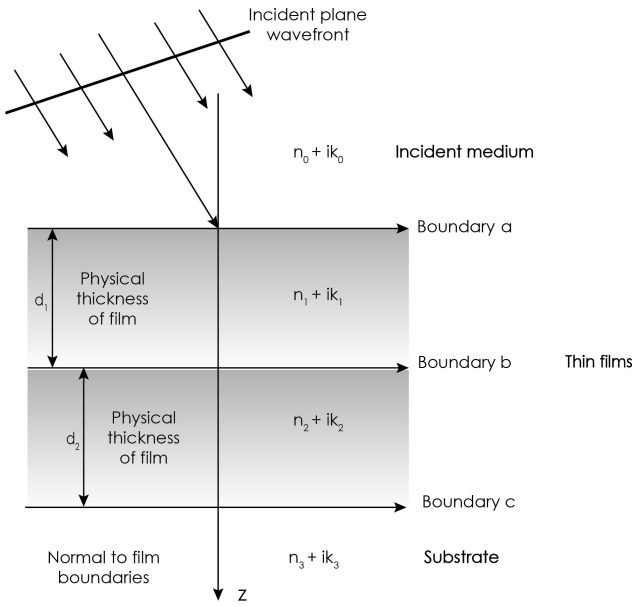

Figure 2.6: Plane wave incident on a structure of two thin film on a substrate.

Once more, it may be used Equation (2.94) to provide the interface a parameters

$$\begin{bmatrix} \boldsymbol{\mathcal{E}}_a \\ \boldsymbol{\mathcal{H}}_a \end{bmatrix} = \begin{bmatrix} \cos\delta_1 & (i\sin\delta_1)/\eta_1 \\ i\eta_1\sin\delta_1 & \cos\delta_1 \end{bmatrix} \begin{bmatrix} \cos\delta_2 & (i\sin\delta_2)/\eta_2 \\ i\eta_2\sin\delta_2 & \cos\delta_2 \end{bmatrix} \begin{bmatrix} \boldsymbol{\mathcal{E}}_c \\ \boldsymbol{\mathcal{H}}_c \end{bmatrix}$$

therefore, the characteristic matrix of the assembly

$$\begin{bmatrix} B \\ C \end{bmatrix} = \begin{bmatrix} \cos\delta_1 & (i\sin\delta_1)/\eta_1 \\ i\eta_1\sin\delta_1 & \cos\delta_1 \end{bmatrix} \begin{bmatrix} \cos\delta_2 & (i\sin\delta_2)/\eta_2 \\ i\eta_2\sin\delta_2 & \cos\delta_2 \end{bmatrix} \begin{bmatrix} 1 \\ \eta_3 \end{bmatrix}$$

As previously, the Equations (2.97) yield $\mathcal{Y} = C/B$, the reflectance R and the amplitude reflection coefficient ρ. In the general case of a stucture of q layers, the characteristic matrix is simply the product of the individual matrices taken in the correct order, that plays a crucial role in optical thin-film research and serves as the foundation for practically all computations. Therefore

$$\begin{bmatrix} B \\ C \end{bmatrix} = \left\{ \prod_{r=1}^{q} \begin{bmatrix} \cos\delta_r & (i\sin\delta_r)/\eta_r \\ i\eta_r\sin\delta_r & \cos\delta_r \end{bmatrix} \right\} \begin{bmatrix} 1 \\ \eta_m \end{bmatrix} \tag{2.101}$$

where

$$\delta_r = \frac{2\pi \left(n_r - ik_r\right) d_r \cos \vartheta_r}{\lambda}$$

$$\begin{aligned} \eta_r &= Y_0 \left(n_r - ik_r\right) \cos \vartheta_r \qquad \text{for } s\text{-polarization(TE)} \\ \eta_r &= Y_0 \left(n_r - ik_r\right) / \cos \vartheta_r \qquad \text{for } p\text{-polarization(TM)} \end{aligned}$$

where the suffix m refers to the substrate or emergent media

$$\begin{aligned} \eta_m &= Y_0 \left(n_m - ik_m\right) \cos \vartheta_m \qquad \text{for } s\text{-polarization(TE)} \\ \eta_m &= Y_0 \left(n_m - ik_m\right) / \cos \vartheta_m \qquad \text{for } p\text{-polarization(TM)} \end{aligned}$$

Given the angle of incidence ϑ_0, it is possible to obtain the value of ϑ_r from Snell's law, i.e.,

$$\left(n_0 - ik_0\right) \sin \vartheta_0 = \left(n_r - ik_r\right) \sin \vartheta_r = \left(n_m - ik_m\right) \sin \vartheta_m \quad (2.102)$$

The product of any number of these matrices has the same determinant as the characteristic matrix of a thin film, which is unity. This is a useful property for the analysis of multilayer structures

The arrangement to apply for computing phase thicknesses and admittances in the case of absorbing media is as follows, in order to avoid complications over signs and quadrants:

$$\delta_r = \left(2\pi/\lambda\right) d_r \left(n_r^2 - k_r^2 - n_0^2 \sin^2 \vartheta_0 - 2in_r k_r\right)^{1/2} \quad (2.103)$$

With the correct solution being in the fourth quadrant. Then

$$\eta_{rs} = Y_0 \left(n_r^2 - k_r^2 - n_0^2 \sin^2 \vartheta_0 - 2in_r k_r\right)^{1/2} \quad (2.104)$$

also in the fourth quadrant, and

$$\eta_{rp} = \frac{y_r^2}{\eta_{rs}} = \frac{Y_0^2 \left(n_r - ik_r\right)^2}{\eta_{rs}} \quad (2.105)$$

Now the phase shift ϕ related to the reflected beam can be calculated, using the multilayer's front surface as a reference surface.

Let $\mathcal{Y} = a + ib$ and η_0 real

$$\begin{aligned}\rho &= \frac{\eta_0 - a - ib}{\eta_0 + a + ib} \\ &= \frac{(\eta_0^2 - a^2 - b^2) - i\,(2b\eta_0)}{(\eta_0 + a)^2 + b^2}\end{aligned}$$

then

$$\tan\phi = \frac{(-2b\eta_0)}{(\eta_0^2 - a^2 - b^2)} \tag{2.106}$$

It is essential to maintain the signs of the numerator and denominator independently in order to specifically identify the quadrant in which the vector associated with ρ occurs. By dealing with the denominator as the x coordinate and the numerator as the y coordinate, the following scheme can be created.

Numerator	+	+	-	-
Denominator	+	-	+	-
Quadrant	1st	2nd	4th	3nd

2.5 Reflectance, Transmittance and Absorptance

The Equation (2.101) may be used to determine a thin-film assembly's transmittance and absorptance. As it has previously been established, the incident medium must be transparent for this to have a physical meaning; hence, η_0 must be real. Although the substrate need not be transparent, the computed transmittance will be the transmittance into the substrate rather than through it. The kth interface is determined first by calculating the net irradiance at the assembly's exit side. It is provided by

$$\begin{aligned}I_k &= \frac{1}{2} Re\left(\boldsymbol{\mathcal{E}}_k \boldsymbol{\mathcal{H}}_k^*\right) \\ &= \frac{1}{2} Re\left(\boldsymbol{\mathcal{E}}_k \eta_{in}^* \boldsymbol{\mathcal{E}}_k^*\right) \\ &= \frac{1}{2} Re\left(\eta_{in}^*\right) \boldsymbol{\mathcal{E}}_k \boldsymbol{\mathcal{E}}_k^*\end{aligned} \tag{2.107}$$

In case the characteristic matrix of the assembly is

$$\begin{bmatrix} B \\ C \end{bmatrix}$$

the net irradiance at the assembly's entry is

$$I_a = \frac{1}{2} Re\left(BC^*\right) \boldsymbol{\mathcal{E}}_k \boldsymbol{\mathcal{E}}_k^* \tag{2.108}$$

Assuming that the incident irradiance is represented by the symbol I_i, the irradiance that actually enters the assembly is represented by the Equation (2.108), which is $(1 - R)\, I_i$:

$$(1 - R)\, I_i = \frac{1}{2} Re\left(BC^*\right) \boldsymbol{\mathcal{E}}_k \boldsymbol{\mathcal{E}}_k^*$$

then,

$$I_i = \frac{Re\left(BC^*\right) \boldsymbol{\mathcal{E}}_k \boldsymbol{\mathcal{E}}_k^*}{2\,(1 - R)}$$

Being Equation (2.107) the irradiance entering the substrate from the assembly, the transmittance T is as follows:

$$T = \frac{I_k}{I_i} = \frac{Re\left(\eta_m\right)(1 - R)}{Re\left(BC^*\right)} \tag{2.109}$$

The connection between the multilayer's absorptance A and R and T is

$$1 = R + T + A$$

so that

$$A = 1 - R - T = (1 - R)\left(1 - \frac{Re\left(\eta_m\right)}{Re\left(BC^*\right)}\right) \tag{2.110}$$

It is simple to demonstrate that the above formulas are compatible with $A = 0$ and $T + R = 1$ in the absence of absorption in any of the layers since each film matrix will have determinants of unity and any product of these matrices will likewise have a determinant of unity. The matrix product may be written as

$$\begin{bmatrix} \alpha & i\beta \\ i\gamma & \delta \end{bmatrix}$$

because there is no absorption α, β, γ and δ are all real and $\alpha\delta + \gamma\beta = 1$.

$$\begin{bmatrix} B \\ C \end{bmatrix} \begin{bmatrix} \alpha & i\beta \\ i\gamma & \delta \end{bmatrix} \begin{bmatrix} 1 \\ \eta_m \end{bmatrix} = \begin{bmatrix} \alpha + i\beta\eta_m \\ \delta\eta_m + i\gamma \end{bmatrix}$$

$$\begin{aligned} Re\left(BC^*\right) &= Re\left[\left(\alpha + i\beta\eta_m\right)\left(\delta\eta_m - i\gamma\right)\right] = \left(\alpha\delta + \gamma\beta\right) Re\left(\eta_m\right) \\ &= Re\left(\eta_m\right) \end{aligned}$$

and the result follows.

From Equation (2.97) by manipulating it we can obtain Equation (2.109) and Equation (2.110) into the most useful form.

$$R = \left(\frac{\eta_0 B - C}{\eta_0 B + C}\right)\left(\frac{\eta_0 B - C}{\eta_0 B + C}\right)^* \tag{2.111}$$

so that

$$(1 - R) = \frac{2\eta_0\left(BC^* + B^*C\right)}{\left(\eta_0 B + C\right)\left(\eta_0 B + C\right)^*} \tag{2.112}$$

Substituting this result in Equation (2.109) we obtain

$$T = \frac{4\eta_0 Re\left(\eta_m\right)}{\left(\eta_0 B + C\right)\left(\eta_0 B + C\right)^*} \tag{2.113}$$

and in Equation (2.110)

$$A = \frac{4\eta_0 Re\left(BC^* - \eta_m\right)}{\left(\eta_0 B + C\right)\left(\eta_0 B + C\right)^*} \tag{2.114}$$

The shift in phase on reflection Equation (2.106) can be exressed as

$$\varphi = \arctan\left(\frac{Im\left[\eta_m\left(BC^* - CB^*\right)\right]}{\left(\eta_m^2 BB^* - CC^*\right)}\right) \tag{2.115}$$

The quadrant of φ is given by the same arrangement of signs of numerator and denominator as Equation (2.106).

The numerator and denominator signs are arranged in the same manner as in Equation (2.106) to get the quadrant of φ. Phase shift on transmission is the difference in phase between the incident wave entering the multilayer and the resultant transmitted wave

entering the emerging medium. Since the electric field amplitude at the emerging surface has been normalized to unity, the phase may be assumed to be zero. The incident amplitude expression, which will involve B and C, must then be found. These are the normalized total tangential electric and magnetic fields. Thus, it can be said:

$$\begin{aligned} \boldsymbol{\mathcal{E}}_i + \boldsymbol{\mathcal{E}}_r &= B \\ \eta_0 \boldsymbol{\mathcal{E}}_i - \eta_0 \boldsymbol{\mathcal{E}}_r &= C \end{aligned}$$

Then

$$E_i = \frac{1}{2}\left(B + \frac{C}{\eta_0}\right)$$

and the amplitude trasmission coefficient as

$$\tau = \frac{2\eta_0}{(\eta_0 B + C)} = \frac{2\eta_0 \left(\eta_0 B + C\right)^*}{(\eta_0 B + C)\left(\eta_0 B + C\right)^*}$$

so that

$$\varphi_t = \arctan\left[\frac{-Im\left(\eta_0 B + C\right)}{Re\left(\eta_0 B + C\right)}\right] \tag{2.116}$$

Once more, it's crucial to keep the denominator and numerator's signs distinct. The quadrant is then determined by the same sign configuration as Equation (2.106).

The admittance of the front surface of the multilayer determines reflectance, whereas the potential transmittance is necessary to determine transmittance. The ratio of irradiance exting by the back interface to that entering at the front interface is known as the potential transmittance, ψ, of a layer or an assembly of layers. It is provided by

$$\psi = \frac{I_{exit}}{I_{enter}} = \frac{T}{(1 - R)} \tag{2.117}$$

The net irradiance that really enters the system as a whole is the difference between the incident and reflected irradiances. Keep in mind that the irradiances in question are the normal components according to the definitions of reflectance and transmittance. The product of all the individual potential transmittances in a

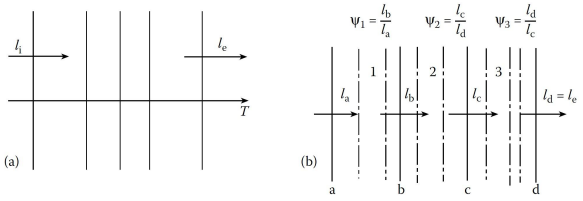

Figure 2.7: (a) An assembly of thin films. (b) The potential transmittance of an assembly of thin film.

group of subassemblies of layers is the potential transmittance of that group. Figure 2.7 depicts a system made up of a number of film components. Then

$$\psi = \frac{I_e}{I_i} = \frac{I_d}{I_a} = \frac{I_b}{I_a}\frac{I_c}{I_b}\frac{I_b}{I_c} = \psi_1\psi_2\psi_3 \tag{2.118}$$

The parameters of the layer, or collection of layers, involved, as well as the features of the structure at the exit interface, determine the prospective transmittance, which indicates the transmittance that this specific combination would provide in the absence of reflection losses. As a result, it represents the highest transmittance that might be achieved from the configuration. By definition, the potential transmittance is uninfluenced when a transparent structure is deposited over the front surface. However, the transmittance may be impacted, thus the layers added to the front surface must maximize the irradiance that actually enters the assembly in order to ensure that the transmittance is equal to the potential transmittance. This involve achieving zero reflectivity for the entire assembly and, so, applying an antireflection coating. However, any modifications to the structure at the exit interface have an impact on the potential transmittance, and it is conceivable to increase the potential transmittance of a subassembly in this manner.

B and C stand for the normalized electric and magnetic fields at every given interface in the matrix formulation for the characteristics of any combination of thin films. The net normalized irradiance is thus provided by $\frac{1}{2}Re(BC*)$, with Equation (2.118) being accurate if the irradiances is defined as the net irradiance

traveling across the proper interface. The irradiancescan be replaced in Equations (2.117) and (2.118).

The potential transmittance may be determined using the properties of the layer or subassembly as well as the optical admittance at the back surface. The full multilayer performance will be provided by

$$\begin{bmatrix} B \\ C \end{bmatrix} = \left[\underline{\underline{M}}_1\right] \left[\underline{\underline{M}}_2\right] \cdots \left[\underline{\underline{M}}_a\right] \left[\underline{\underline{M}}_b\right] \left[\underline{\underline{M}}_c\right] \cdots \left[\underline{\underline{M}}_p\right] \left[\underline{\underline{M}}_q\right] \begin{bmatrix} 1 \\ \eta_m \end{bmatrix}$$

where the potential transmittance $\left[\underline{\underline{M}}_a\right] \left[\underline{\underline{M}}_b\right] \left[\underline{\underline{M}}_c\right]$ of the subassembly is to be calculated. The product of the subassembly rightmost matrix will be supplied by

$$\begin{bmatrix} B_e \\ C_e \end{bmatrix}$$

Now, if

$$\begin{bmatrix} B_i \\ C_i \end{bmatrix} = \left[\underline{\underline{M}}_a\right] \left[\underline{\underline{M}}_b\right] \left[\underline{\underline{M}}_c\right] \begin{bmatrix} B_e \\ C_e \end{bmatrix} \tag{2.119}$$

Then

$$\psi = \frac{Re\left(B_e C_e^*\right)}{Re\left(B_i C_i^*\right)} \tag{2.120}$$

By dividing Equation (2.119) by B_e we have

$$\begin{bmatrix} B_i' \\ C_i' \end{bmatrix} = \left[\underline{\underline{M}}_a\right] \left[\underline{\underline{M}}_b\right] \left[\underline{\underline{M}}_c\right] \begin{bmatrix} 1 \\ Y_e \end{bmatrix}$$

where $Y_e = C_e/B_e, B_1' = B1/B_e, C_1' = C_1/C_e$, and the potential transmittance is

$$\begin{aligned} \psi &= \frac{Re\left(Y_e\right)}{Re\left(B_i' C_i'^*\right)} \\ &= \frac{Re\left(C_e/B_e\right)}{Re\left[\left(B_i/B_e\right)\left(C_i^*/B_e^*\right)\right]} = \frac{B_e B_e^* Re\left(C_e/B_e\right)}{Re\left(B_i/C_i\right)} \\ &= \frac{Re\left(B_e^* C_e\right)}{B_i C_i^*} = \frac{Re\left(B_e C_e^*\right)}{B_i C_i^*} \end{aligned}$$

which is identical to Equation (2.120).

2.6 Transmittance of a Thin-Film Assembly

An alternative way to calculate the transmittance of a single layer is the Characteristics Matrix Method which is particularly useful for our purposes because the transmittance of a cascade of many layers can be easily retrieved. Indeed, the transmittance of a thin film ensemble, with or without absorption, is independent of the direction of light propagation. A proof of this result, by Abelès, as we shall see, who was responsible for developing the matrix approach to thin film analysis, quickly follows from the properties of matrices. Indicate the matrices of the various layers of the assembly with

$$\left[\underline{\underline{M}}_1\right]\left[\underline{\underline{M}}_2\right], \ldots \left[\underline{\underline{M}}_q\right]$$

and considering the two massive media on either side be transparent. The two products of the matrices, which represent the two potential propagation directions, may be represented as

$$\left[\underline{\underline{M}}\right] = \left[\underline{\underline{M}}_1\right]\left[\underline{\underline{M}}_2\right]\left[\underline{\underline{M}}_3\right], \ldots \left[\underline{\underline{M}}_q\right]$$

and

$$\left[\underline{\underline{M'}}\right] = \left[\underline{\underline{M}}_q\right]\left[\underline{\underline{M}}_{q-1}\right], \ldots \left[\underline{\underline{M}}_2\right]\left[\underline{\underline{M}}_1\right]$$

Now, it can be demonstrated that if we express the matrices in such a way that the diagonal terms are equivalent regardless of whether there is absorption

$$\left[\underline{\underline{M}}\right] = [a_{ij}] \text{ and } \left[\underline{\underline{M'}}\right] = \left[a'_{ij}\right]$$

then

$$a_{ij} = a'_{ij}\,(1 \neq j)\,, a_{11} = a'_{22} \text{ and } a_{22} = a'_{11}$$

The medium on one side of the assembly is denoted by η_0, which is next to layer 1, and on the other by η_m. Equation (2.101) provides the characteristic matrix for the first direction

$$\begin{bmatrix} B \\ C \end{bmatrix} = \left[\underline{\underline{M}}\right]\begin{bmatrix} 1 \\ \eta_m \end{bmatrix}$$

and

$$B = a_{11} + a_{12}\eta_m \qquad C = a_{21} + a_{22}\eta_m$$

In the second case

$$B = a'_{11} + a'_{12}\eta_0 = a_{22} + a_{22}\eta_0$$

$$C = a'_{21} + a'_{22}\eta_0 = a_{21} + a_{11}\eta_0$$

Therefore, Equation (2.113) provides the two equations for the transmittance of the assembly

$$T = \frac{4\eta_0\eta_m}{|\eta_0 (a_{11} + a_{12}\eta_m) + a_{12} + a_{22}\eta_m|^2}$$

$$T' = \frac{4\eta_m\eta_0}{|\eta_m (a_{22} + a_{12}\eta_0) + a_{21} + a_{11}\eta_0|^2}$$

which are the same.

Clearly, this condition does not extend to the reflectance of an assembly, which must be the same on all sides of the assembly if there is no absorption in any of the layers. This formulation demonstrates, among other factors, that a one-way mirror – which only permits light to pass through it in one direction – cannot be made with straightforward optical thin films. The typical one-way mirror operates by relying on a discernible difference in the lighting conditions present on each side and has a high reflectance with some transmission.

2.7 Coherence

Coherence is a feature of the whole optical system and quantifies the ability to produce detectable interference effects. A characteristic of the whole optical system is coherence. *Coherent* is often used to characterize the existence of the greatest interference effects, and *incoherent* to express their total absence. Cases that fall within this limits are referred to as *partially coherent*.

The phenomena are presumpted to be stationary in every situation. This suggests that even though the waves may vary, their statistical characteristics do not change over time. An arbitrary wave is represented by a corresponding spectrum of harmonic waves by

taking advantage of how linear the interactions are. A pair of linearly polarized plane waves with equal polarization, propagating along the z-axis and with complex amplitudes $\boldsymbol{\mathcal{E}}_1$ and $\boldsymbol{\mathcal{E}}_2$, should be generated from a single spectral element. Let varphi 1 and varphi 2 be the phases of these two waves at $z = 0$ and $t = 0$, with φ_1 and φ_2 being included in the complex amplitudes. Since the polarizations are exactly equal, the electric and magnetic fields resulting from a combination of the waves will be the simple sums of the components. The resulting radiation will therefore be:

$$\begin{aligned} I &= \frac{1}{2} Re\left[(E_1 + E_2)\left(H_1 + H_2\right)^*\right] = \frac{1}{2} Re\left[(E_1 + E_2)\, y^*\left(E_1 + E_2\right)^*\right] \\ &= \frac{1}{2} Re\left(y\right) E_1 E_1^* + \frac{1}{2} Re\left(y\right) E_2 E_2^* + Re\left(y\right) E_1 E_1^* Re\left(E_1 E_2^*\right) \end{aligned} \tag{2.121}$$

$$\begin{aligned} I &= I_1 + I_2 + Re\left(y\right) Re\left(\boldsymbol{\mathcal{E}}_1 \boldsymbol{\mathcal{E}}_2^*\right) \\ &= I_1 + I_2 + 2\sqrt{I_1 I_2}\cos\left(\varphi_1 - \varphi_2\right) \end{aligned} \tag{2.122}$$

However, there are many more light waves involved, and they may have various frequencies, phases, or amplitudes. They add to the final irradiance, which is the total of all of the individual irradiances plus the interference terms.

The distribution of parameters among the different light waves determines everything. The interference term may be equally strong in this instance, making it coherent, or it might cancel out entirely in an incoherent situation since the terms might be positive or negative, or it might take on a value in the middle, making it somewhat coherent.

The interference term might become jumbled due to changes in the source of light or any other aspect of the system. For instance, there could be fluctuations in thickness throughout a thin film's aperture. Typically, a substrate behave incoherently due to its thickness that presents also a sufficient variability.

Real systems never have a single, endless, planar, linearly polarized harmonic wave of light, and they also never have perfect elements. A few straightforward parameters aid in the evaluation of coherence.

It will be first taken into account as a function of the light. Two rays that are pulled out from the exact same spot in a beam of light generate an interference effect with fringes. As the distance between the two spot increase, the interference fringes gradually lessen in intensity (less pronounced).

The distance between the two spots provides a gauge of coherence when the fringes simply vanish. The *coherence length* is the distance between two places if they are separated in the main light's direction of propagation. The *coherence area*, or *coherence volume*, is the region where the fringes simply disappear if the light is derived from an entire area, or volume, of the original light rather than two spots. The *coherence time* is the delay at which the fringes simply vanish, if moving the points is substituted for delaying one sample by a variable amount of time. It is obvious that coherence time is just the amount of time it takes for light to cover a coherence length.

Now, primary light can be expressed in terms of its spectral components and the spectrum is thought of as a continuous band of wavelengths with a bandwidth of $\Delta\lambda$ around λ, interference fringes are formed utilizing this light with a variable path difference. As the path difference is raised, the fringes will get spread out and the contrast will decrease since each wavelength will create its own unique set of fringes. The coherence length will be determined by the path difference at the location where they abruptly vanish. The point may be described as the location at which the fringes will spread out across the space between them.

Then, an order $m-1$ fringe at the longest wavelength will just overlap with an order m fringe at the smallest.

$$\text{Path difference} = m\left(\lambda - \frac{\Delta\lambda}{2}\right) = (m-1)\left(\lambda + \frac{\Delta\lambda}{2}\right) \quad (2.123)$$

$$\text{Coherence length} = \left(m - \frac{1}{2}\right)\lambda = \frac{\lambda^2}{\Delta\lambda} \quad (2.124)$$

$$\text{Coherence time} = \frac{\lambda^2}{c\Delta\lambda} \quad (2.125)$$

where c is 299.792458 nm/fs. Being vartheta the cone semiangle

and being the cone axis at normal incidence, using a rough two-dimensional model, it is possible to rephrase Equation (2.123) as

$$m\lambda = (m+1)\,\lambda\cos\vartheta \tag{2.126}$$

and

$$\text{Coherence length} = m\lambda = \frac{\lambda\cos\vartheta}{1-\cos\vartheta} \simeq \frac{2\lambda}{\vartheta^2} \tag{2.127}$$

or, if ϑ is given in degree

$$\text{Coherence length} = \frac{(7\times 10^3)\lambda}{\vartheta^2} \tag{2.128}$$

where ϑ is the angle within the specific thin film structure. It is feasible to estimate the adjustment to Equation in the case where the affected medium has a different index, resulting in:

$$\text{Coherence length} = \frac{(7\times 10^3)\lambda\eta_1^2}{n_0^2\ \vartheta^2} \tag{2.129}$$

wherein n_0 represents the index of the incident medium and n_1 either represents the index of the relevant film or the effective index of the coating. The characteristics of the cone and the film interact to produce this specific coherence length. The combined coherence lengths are as follows when many independent effects, such as cone and bandwidth, are present:

$$\frac{1}{L} = \sqrt{\frac{1}{L_a^2} + \frac{1}{L_b^2} + \dots} \tag{2.130}$$

When considering the characteristics of thin-film coatings, total coherence is assumed, but when discussing substrates, complete incoherence is assumed.

But it's crucial to consider the notion of partial coherence and, consequently, the interference element of Equation (2.121), $Re(y)Re(E_1E_2^*)$. Any given wave can be represented by E_1 and E_2, but the characteristic admittance of the medium, y, must remain constant in order to replace the magnetic field, H, with yE. Instead of assuming that the phase angle φ is the primary distinction between E_2 and E_1, and that the interference phenomenon is

therefore a function of φ, we allow E_1 and E_2 to represent fully general waves in order to obtain a more general derivation. Since φ only applies to harmonic waves, it makes no sense and has no significance. However, since E_1 and E_2 are also time-dependent functions, we may substitute a variable time delay τ for φ. We only take the $E_1 E_2^*$ portion to keep things straightforward. After that enough time has passed or there have been enough measurements, the average should be calculated. The so-called *mutual coherence function* is what it is obtained:

$$\Gamma_{12}(\tau) = \langle E_1(t+\tau) E_2^*(t) \rangle = \lim_{T\to\infty} \frac{1}{2T} \int_{-T}^{T} E_1(t+\tau) E_2^*(t) dt \tag{2.131}$$

$$\gamma_{12}(\tau) = \frac{\Gamma_{12}(\tau)}{\sqrt{\Gamma_{11}(0)}\sqrt{\Gamma_{22}(0)}} = \frac{\langle E_1(t+\tau) E_2^*(t) \rangle}{\sqrt{\langle E_1(t) E_1^*(t) \rangle}\sqrt{\langle E_2(t) E_2^*(t) \rangle}} \tag{2.132}$$

where $\gamma_{12}(\tau)$ is know as the complex degree of coherence. It is possible to rewrite (2.121) as:

$$\begin{aligned} I &= \frac{1}{2} Re(y) \langle E_1(t) E_1^*(t) \rangle + \frac{1}{2} Re(y) \langle E_2(t) E_2^*(t) \rangle \\ &\quad + Re(y) Re\left(\langle E_1(t+\tau) E_2^*(t) \rangle \right) \\ &= \frac{1}{2} Re(y) \langle E_1(t) E_1^*(t) \rangle + \frac{1}{2} Re(y) \langle E_2(t) E_2^*(t) \rangle \\ &\quad + Re(y) \sqrt{\langle E_1(t) E_1^*(t) \rangle + \frac{1}{2} Re(y) \langle E_2(t) E_2^*(t) \rangle} Re\left[\gamma_{12}(\tau) \right] \\ &= I_1 + I_2 + 2\sqrt{I_1 I_2} Re\left[\gamma_{12}(\tau) \right] \end{aligned} \tag{2.133}$$

where it is observed that the shape of the fringe is related to the real part of the degree of coherence (which is complex). If the fringes are similar, but not equal, to the cosine or sine function it is possible to define a fringe visibility like this:

$$V = \frac{I_{max} - I_{min}}{I_{max} + I_{min}} \tag{2.134}$$

The fringe is a cyclic function. Using the complex degree of coherence, the maximum and lowest extrema may be determined.

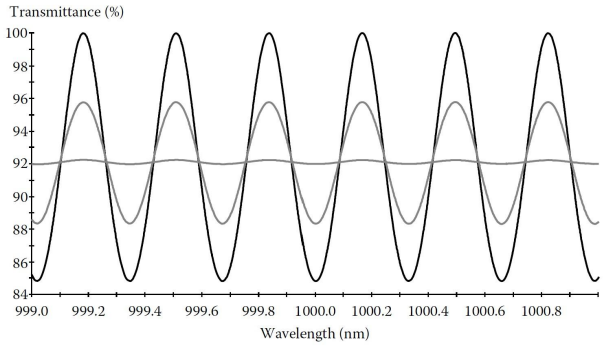

Figure 2.8: The appearance of fringes in a perfectly parallel glass substrate illuminated with light of various bandwidths (i.e. coherence length). The fringes show reducing amplitude with decreasing coherence length.

The whole complex form is effectively a rotating vector even if the real component is a fluctuating function. As a result, the magnitude denotes the amplitude of the fringe function and the visibility comes from:

$$V = \frac{2\sqrt{I_1 I_2}|\gamma_{12}(\tau)|}{I_1 + I_2} \tag{2.135}$$

The greatest level of fringe visibility is attained with value $|\gamma|$ when I_1 and I_2 are the same. Equation (2.135) connects the complex degree of coherence simply to the visibility of the fringes for direct evalutation of it.

The main emphasis has been on using time as a variable to create coherence functions, although it seems obvious that distance might also be a factor. The coherence length and time are essentially the length or time at which the magnitude of the complex degree of coherence decreases to a suitable level, as shown in Figure2.8. The level that is usually picked in this computation is the one that makes the most sense.

2.8 Incoherent Reflection at Two or More Surfaces

Substrates had hitherto been considered as being one-sided slabs of material infinitely deep. This is the practical case when the substrate is lossy and with a thickness which is much higher then the penetration depth so that it can be considered as infinite. The substrate will almost always have a limited depth and back surfaces that reflect part of the energy and impair the performance of the assembly. In this case the substrate has losses that can be neglected at the operating frequencies. The depth of the substrate is often considerably more than the light's wavelength, and changes in the flatness and parallelism of the two surfaces will typically be noticeable fractions of a wavelength. The incident light is typically not very well collimated. The substrate is referred to be thick because, under these conditions, interference effects between light reflected at the front and back surfaces of the substrate will not be seen with a limited aperture.

The fundamental path difference in all interference effects, i.e. the double traversal of the substrate, is greater than the coherence length. The accumulation of multiple waves is identified as incoherent rather than coherent. The interference element in Equation (2.122) disappears, leaving us with the sum of the irradiances rather than the vector sum of the amplitudes. Figure 2.9 provides an illustration of the symbols used. The front and back surfaces sequentially reflect waves.

The sums of the irradiances are given by

$$\begin{aligned} R &= R_a^+ + T_a^+ R_b^+ T_a^- \left[1 + R_a^+ R_a^- + \left(R_a^+ R_a^-\right)^2 + \ldots\right] \\ &= R_a^+ + \left[T_a^+ R_b^+ T_a^- / \left(1 - R_a^- R_b^+\right)\right] \end{aligned}$$

that is, since T^+ and T^- are always identical

$$T_a^+ = T_a^- = T_a$$

and so

$$R = \frac{R_a^+ + R_b^+ \left(T_a^2 - R_a^- R_a^+\right)}{1 - R_a^- R_b^+}$$

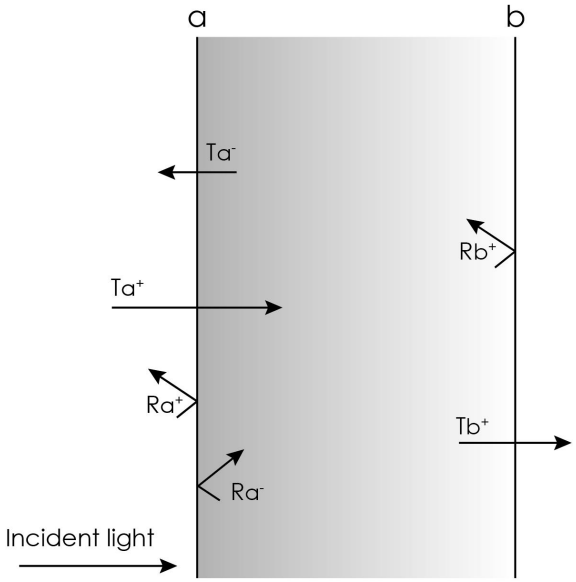

Figure 2.9: Notation for calculation of incoherent reflection at two or more surfaces.

If there is no absorption in the layers,

$$R_a^+ = R_a^- = R_a$$

and

$$1 = R_a + T_a$$

so that

$$R = \frac{R_a + R_b - 2R_aR_b}{1 - R_aR_b}$$

Similarly

$$T = T_a^+ T_b^+ \left[1 + R_a^- R_b^+ \left(R_a^- R_b^+\right)^2 + \ldots\right]$$

$$= \frac{T_aT_b}{1 - R_a^- R_b^+}$$

and again, if there is no absorption,

$$T = \frac{T_aT_b}{1 - R_aR_b} \tag{2.136}$$

or

$$T = \left(\frac{1}{T_a} + \frac{1}{T_b} - 1 \right)^{-1} \tag{2.137}$$

because

$$R_a = 1 - T_a \qquad R_b = 1 - T_b$$

Equation may be solved using a nomogram that is simple to create. Two right-angle axes are set out. Using the intersection as the zero, two linear equal transmittance scales are chalked out on the axes. These are both marked Ta and Tb, respectively. A third axis that will have the T scale written on it divides the angle between Ta and Tb.

A nomogram for solving Equation (2.137) can easily be constructed. Two axes at right angles are laid out on a sheet of graph paper and, taking the point of intersection as the zero, two linear equal scales of transmittance are marked out on the axes. One of these is labeled $T_a$and the other, T_b. The angle between T_a and T_b is bisected by a third axis that is to have the T scale marked out on it. To do this, a straight edge is placed so that it passes through the 100% transmittance value on, say, the T_a-axis and any chosen transmittance on the T_b-axis. The value of T to be associated with the point where the straight edge crosses the T-axis is then that of the intercept with the T_b-axis. The entire scale can be marked out in this way. A completed nomogram of this type is shown in Figure 2.10.

In the absence of absorption, the analysis can be very simply extended to further surfaces. Consider the case of two substrates, i.e., four surfaces. These can be labeled T_a, T_b, T_c, and T_d. Then, from Equation (2.137), we have for the first substrate

$$T_1 = \left(\frac{1}{T_a} + \frac{1}{T_b} - 1 \right)^{-1}$$

then

$$\frac{1}{T_1} = \frac{1}{T_a} + \frac{1}{T_b} - 1$$

and similarly for the second

$$\frac{1}{T_2} = \frac{1}{T_c} + \frac{1}{T_d} - 1$$

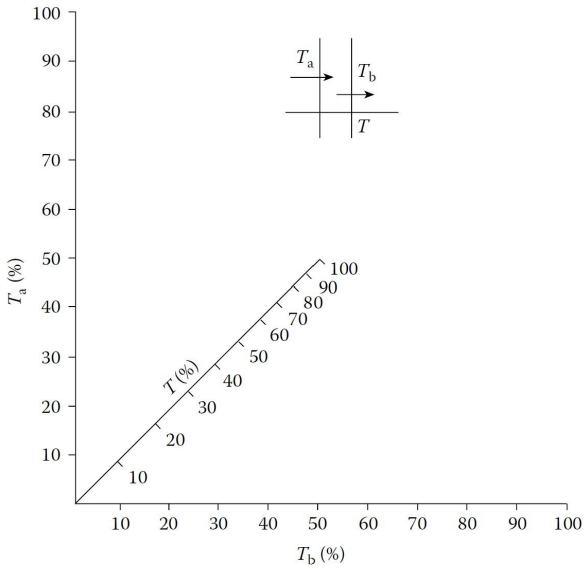

Figure 2.10: A nomogram for calculating the overall transmittance of a thick transparent plate given the transmittance of each individual surface.

The transmittance through all four surfaces is then obtained by applying Equation (2.137) again:

$$\frac{1}{T} = \frac{1}{T_1} + \frac{1}{T_2} - 1$$

i.e,

$$T = \left(\frac{1}{T_a} + \frac{1}{T_b} + \frac{1}{T_c} + \frac{1}{T_d} - 3 \right)^{-1} \tag{2.138}$$

For a succession of surfaces it is used a technique based on a matrix form of the calculation. The emphasis is placed on the flows of irradiance. Absorption in the media between the coated surfaces is supposed sufficiently small so that the coupling problem is negligible. The symbols are defined in Figure 2.11.

The direction of the light is denoted by the usual plus and minus signs. a and b are two coatings separated by a medium m with internal transmittance T_{mint}. The final medium will be the emergent medium and there, the negative-going irradiance will be

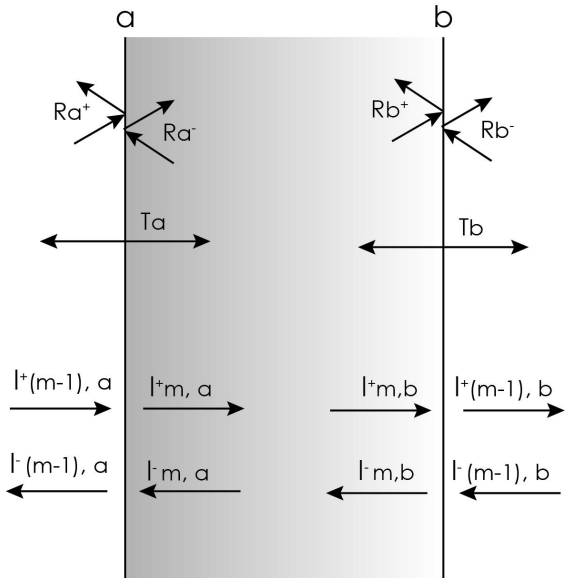

Figure 2.11: Symbols defining two successive coatings (a) and (b) with intervening medium in a stack.

zero. The procedure to be outlined will derive the values of I^+_{ma} and I^-_{ma} from $I^+_{(m+1)b}$ and $I^-_{(m+1)b}$. The irradiances on either side of the coating with label b are related through the equations

$$\begin{aligned} I^+_{(m+1)b} &= T_b I^+_{mb} + R^-_b I^-_{(m+1)b} \\ I^-_{mb} &= R^+_b I^+_{mb} + T_b I^-_{(m+1)b} \end{aligned}$$

These can be manipulated into the form

$$\begin{aligned} I^-_{mb} &= \frac{1}{T_b}\left\{R^+_b I^+_{(m+1)b} + \left(T^2_b - R^-_b R^+_b\right) I^-_{(m+1)b}\right\} \\ I^+_{mb} &= \frac{1}{T_b}\left\{I^+_{(m+1)b} - R^-_B I^-_{(m+1)b}\right\} \end{aligned}$$

and in matrix form this is

$$\begin{bmatrix} I^-_{mb} \\ I^+_{mb} \end{bmatrix} = \begin{bmatrix} \dfrac{\left(T^2_b - R^-_B R^+_b\right)}{Tb} & \dfrac{R^+_b}{T_b} \\ \dfrac{-R^-_b}{T_b} & \dfrac{1}{T_b} \end{bmatrix} \begin{bmatrix} I^-_{(m+1)b} \\ I^+_{(m+1)b} \end{bmatrix} \tag{2.139}$$

The conversion through the medium is given by

$$\begin{bmatrix} I_{ma}^{-} \\ I_{ma}^{+} \end{bmatrix} = \begin{bmatrix} T_{m\text{int}} & 0 \\ 0 & \dfrac{1}{T_{m\text{int}}} \end{bmatrix} \begin{bmatrix} I_{mb}^{-} \\ I_{mb}^{+} \end{bmatrix} \tag{2.140}$$

Equations (2.139) and (2.140) can be applied to the various coatings and intervening media in succession.

Chapter 3

Development of mirror coatings

As described above, by measuring the interferometric figure due to the length differences between mirrors in the arms of kilometer-long Michelson interferometers, gravitational waves are identified. Therefore, very sensitive interferometers that accurately measure the separation between suspended test masses coated to function as highly reflecting mirrors have been designed in order to detect gravitational waves. Any change in the distance between the mirrors results in a very little shift in the beams' phases, and so a changes in the intensity of the light, which depends on the wave's amplitude. In addition to the passage of a gravitational wave through the instrument, there may be additional causes for the power to vary, the so-called noises. The strain sensitivity may be restricted by a variety of noise sources: Current major noise sources in interferometric GW detectors establishing their maximal visible distance in the (40-300) Hz band, where all recent detections have been made, are thermal (Brownian) fluctuations in the high-reflectance (HR) coatings of the test masses. Furthermore, efforts to attain and exceed the quantum noise limit won't be worthwhile until coating thermal noise has been significantly reduced. Reducing coating thermal noise is thus the top current priority in the design of new generation GW detectors, also called third generation interferometers, such as the KAGRA, that is Kamioka Gravitational Wave Detector, the Einstein Tele-

scope and the upgrade of LIGO Voyager. The current research direction in coating technology explores two promising options for reducing coating thermal noise, namely the search of new material (e.g., crystalline materials nm-layered composite materials, Silicon Nitrides etc.), and the optimization of coating design, and deposition parameters to achieve the best relevant figures of merit (low optical and mechanical losses, high optical contrast). In addition, the use of cryogenic temperatures is envisaged.

This chapter offers a description of the main noise that decreases the sensitivity, and therefore the detection capabilities of the gravitational interferometers and an overview of the most widely used materials as well as the description of new developments to optimize the detection of gravitational waves.

3.1 Noise

Therefore, any noise in a GW interferometer occurs as a effective or seeming change in the position of the mirrors, giving a deceptive signal of the occurrence of a GW. The amplitude spectral sensitivity $h(f)$ is defined for each noise in order to separate the noise source from the gravitational signal:

$$h(f) = \frac{\sqrt{\tilde{x}^2(f)}}{L}, \tag{3.1}$$

where $\tilde{x}^2(f)$ is the power spectral density of the displacement caused by the noise source and L is the interformeter's arm length. The amount $h(f)$, whose dimension is $1/\sqrt{Hz}$, represents the amplitude of the gravitational wave signal that would result in the displacement brought on by the noise.

A GW detector's sensitivity is referred to in terms of strain sensitivity:

$$h(f) = \sqrt{\sum_{i=1}^{n} h_i^2(f)}, \tag{3.2}$$

where $h_i(f)$ is the amplitude spectral densities of the i-th noise affecting the detector.

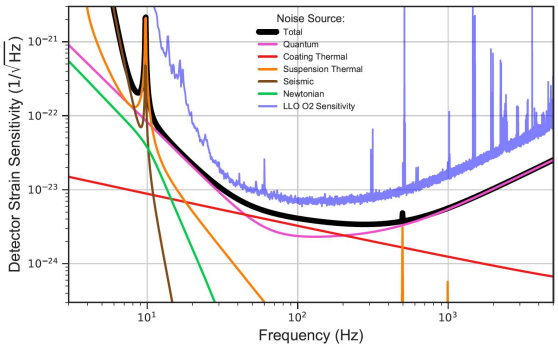

Figure 3.1: Advanced LIGO's strain sensitivity and major noise sources were modelled. The second observation run's LIGO Livingston detector's sensitivity is seen by the blue trace. In this scenario, a lower laser power was supplied into the interferometer to operate the detector. It was not operating at design sensitivity because technological control noise limits sensitivity below 50Hz. The sensitivity is limkitated by: suspension thermal noise and seismic noise - represented by the orange and brown traces - at the low frequency, quantum noise-represented by the pink trace - above 10 Hz and a combination of thermal (red) coating noise and quantum noise between 30 Hz and 500 Hz.

The sensitivity curve shows the minimal gravitational signal intensity that an interferometer can pick up. The key fundamental noise sources that limit the design sensitivity of Advanced LIGO and Advanced Virgo are shown in Figure 3.1 and Figure 3.2 and they are described in this section.

3.2 Seismic and Newtonian Noise

Seismic noise, or the vibration of the terrestrial environment, is a source of displacement noise that must be dealt with. It is mostly caused by human activity (such as road traffic), atmospheric natural occurrences, and several other types of ground-born oscillations in the frequency range of 1-10 Hz (e.g., earthquakes or large activity of ocean water). A GW interferometer is also susceptible to a micro-seismic background, which mostly manifests as surface

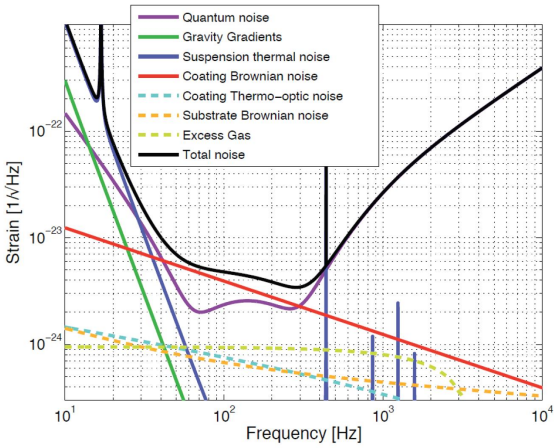

Figure 3.2: Modelled strain sensitivity of Advanced Virgo and principal noise sources. Each noise source is represented by a color curve giving its spectral density in equivalent gravitational wave amplitude. Between 40 Hz and 300 Hz, where the detector is the most sensitive, the most limiting noise source is the coating brownian noise.

waves that disturb the suspension systems and mirrors. The geographic location of the detector greatly affects this noise and for this reason its reduction contributes first of all to a location of the detector in a generally silent area. The amplitude spectral density, at a frequency of 10Hz, is approximately equivalent to:

$$h = 10^{-11} \frac{1}{\sqrt{Hz}} \tag{3.3}$$

that is ten orders of magnitude greater than that relating to gravitational waves (Nardecchia 2022). The gravity gradient noise, often referred to as Newtonian noise, is a result of time-varying Newtonian gravitational forces acting on mirrors as a result of density fluctuations brought on by seismic activity, acoustic phenomena, and turbulent phenomena in the Earth's atmosphere. Changing gravitational (or "Newtonian") forces exerted by transients in the local gravitational field on the suspended test masses cause length noise in the detector arms, which may conceal gravitational wave signals at low frequencies. (Hughes & Thorne 1998) The interfer-

ometer is run in ultra-high vacuum to limit optical scattering and acoustic noise coupling in order to isolate the test masses from non-astrophysical disturbances. To separate the motion of the mirror from the motion of the ground, the test masses are suspended on multi-stage pendulums that are in turn mounted on seismic isolation platforms (Matichard *et al.* 2015). A combination of active seismic isolation between the vacuum tanks and the ground and between the invacuum optical tables and the vacuum tanks is used to produce a degree of isolation that allows the motion of the test masses to be ten orders of magnitude lower than the surface ground motion.

The vibrations conveyed to the mirror are diminished by a factor of f_0^2/f^2 when a single pendulum with resonance frequency f_0 is used. As a result, a N pendula multistage filter has an attenuation factor of $(f_0^2/f^2)^N$.

A single pendulum with resonance frequency f_0 attenuates the vibrations transferred to the mirror by a factor f_0^2/f^2. Thus, a multistage filter made by N pendula provides an attenuation factor $(f_0^2/f^2)^N$. Mirrors cannot be shielded from Newtonian noise due to the direct coupling of gravitational fields. To minimize this noise, arrays of seismic sensors located near the vacuum chambers that house the mirrors are used so that, through the use of algorithms for processing the acquired data, its contribution is subtracted from the output data of the interferometer. The brown trace in Figure 3.1 shows the residual connection of seismic noise to the gravitational wave detection band and Newtonian noise is seen in the green trace in Figure 3.1 and 3.2. The residual coupling of seismic noise to the gravitational wave detection band is seen in the brown trace.

3.3 Quantum Noise

Quantum noise in interferometric detectors arise due to the quantum nature of light, which reveals itself through two fundamental mechanisms:

- *photon counting noise* (shot noise), resulting from statistical variations in the time at which photons arrive at the

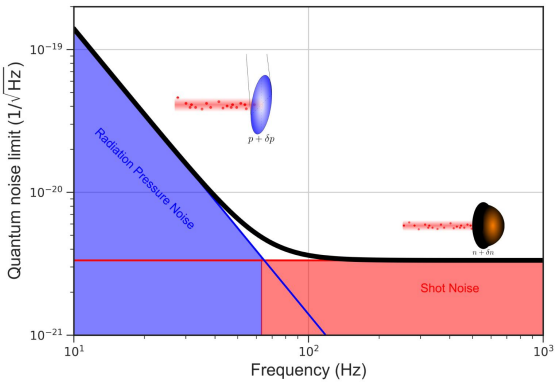

Figure 3.3: Quantum noise in an interferometer. A photodetector measures the fluctuation δn in the number of photons $n + \delta n$ that results in the shutter noise, which is represented in red. The beam imparts to a suspended mirror the random momentum kick $p + \delta p$ resulting in radiation pressure noise. This noise is represented in blue.

interferometer's output. The Fabry-Perot-Michelson interferometer's spectral density for a power recycled is given by:

$$h_{shot}(f) = \frac{1}{8FL}\left(\frac{4\pi\tilde{h}\lambda c}{P_{bs}}\right)^{1/2}\sqrt{1+(f/f_p)^2}; \tag{3.4}$$

- and *radiation pressure noise*, that relates to the operating optical laser power and is photon momentum transfer onto the test masses:

$$h_{rp}(f) = \frac{16\sqrt{2}F}{ML\left(2\pi f\right)^2}\left(\frac{\tilde{h}P_{bs}}{2\pi\lambda c}\right)^{1/2}\frac{1}{\sqrt{1+(f/f_p)^2}}. \tag{3.5}$$

where λ is the main laser's wavelength, P_{bs} is the recycled beam splitter's power, and M is the masses of the interferometer's four test masses. The quantum noise of a typical gravitational wave detector is presented as an example in the plot in Figure 3.3.

At high frequencies, the shot noise dominates, but at low frequencies, the radiation pressure noise component, which is proportional to $1/f^2$, predominates. The shot noise amplitude spectrum

density is inversely proportional to the laser light power, but the radiation pressure amplitude spectral density is proportional to the square root of this power. As a result, even while raising the circulating light power might improve an interferometer's strain sensitivity at high frequencies, doing so will ultimately result in an worsening in that sensitivity at low frequencies as the radiation pressure rises along with the light power.

By altering the interferometer's design parameters, quantum noise may be decreased. Increased mirror mass (M) can reduce radiation pressure noise without affecting shot noise, but there is a technological limit to the size (and hence mass) of optics that can be produced. Shot noise is decreased by raising the laser's effective power (P_{bs}) inside the interferometer's arm cavities, albeit at the price of increased radiation pressure noise. The amount of coherent laser power that can be produced and pumped into an interferometer has a technological limit as well (Strain 1994). Both shot noise and radiation pressure noise would be reduced by lengthening the interferometer (increasing L), but this is again bound by practical issues because the feasibility and cost of the infrastructure of the detectors limits the length of the detector. The bandwidth of the detector is eventually constrained by lengthening the cavity.

Quantum techniques are used to reduce quantum noise and improve measurement accuracy, such as the use of squeezed states of light as an additional input for laser interferometry GW detectors, as suggested by Caves in 1981 (Caves 1981). The correlations between phase and amplitude noise are exploited in the "squeezing" procedure to decrease noise in one quadrature at the price of raising noise in the orthogonal quadrature. The interference from the creation and annihilation of photons at the quantum level in the vacuum, also known as vacuum noise, which permeates all of space at all frequencies, limits the sensitivity.

The classical-limit of the detector sensitivity is imposed by noise fluctuations brought about by vacuum noise at the detector's output port. To get around this restriction, the primary laser is overlaid with a compressed beam that has the same size, shape, and frequency as the main interferometer beam. The quantum noise contributions can be changed by using the compressed light

in place of the traditional vacuum. The radiation pressure did not limit the low frequency range in the current generation of GW advanced detectors, therefore a frequency-independent squeezing was used to reduce shot noise. Squeezed light has been successfully employed to improve gravitational wave detector interferometers by cutting down shot noise.

This quantum noise improvement approach was first showed in the GEO gravitational wave detector (*A Gravitational Wave Observatory Operating Beyond the Quantum Shot-Noise Limit* 2011), (Grote, H. *at all* 2013), and it has since been adopted by the LIGO and Virgo projects (Oelker, E. *et al.* 2014).

Obviously, the radiation pressure noise may become the primary source if the present sensitivity at low frequencies were to improve. Thus, the compressed quadrature must be rotated as a function of frequency to produce the so-called frequency-dependent squeezing, which simultaneously reduces shot noise and quantum radiation pressure noise over the whole detection frequency range. The squeeze ellipse can rotate in this way when a frequency-independent squeezed state interacts with an optical Fabry-Perot resonator known as a filter cavity (Kimble, H. J. *et al.* 2001).

3.4 Thermal Noise

Another primary noise source that affects interferometric detection is thermal noise. Thermal noise causes spurious contributions to interferometric detector outputs, which places a restriction on the sensitivity of GW interferometers over a broad frequency range between a few 40 Hz and 300 Hz.

Brownian fluctuations dominate in this range. This term refers to a random movement of small particles when suspended in a fluid. The name derives from the Scottish botanist Robert Brown who, in 1827, discovered this phenomenon for the first time by observing the motion of pollen uniformly distributed in an aqueous suspension. Later, in 1905, Einstein presented a first mathematical treatment of Brownian noise motion and today it is clear that every generic dissipative mechanism inside a mechanical system exhibits spontaneous thermal fluctuations (Reid & Martin 2016).

In fact, according to the Fluctuation-Dissipation Theorem (Callen & Welton 1951), thermal noise is inherent to all bodies in thermodynamic equilibrium: in a body at steady-state temperature T, the energy equipartition theorem gives to each body a mean energy of $\frac{k_B T}{2}$ where k_B is the Boltzmann constant. This energy is prone to temporal fluctuations because of the interactions between the microscopic constituents that cause random oscillations of macroscopic observables that resemble the impact of the GW passage, translating the vibrations in a movement of the surfaces of the mirrors which involves a modification of the length of the detector arms. Therefore, the accuracy with which the variations of the interferometric lengths are measured and therefore the ability to detect gravitational waves is compromised.

The thermal noise in the GW detectors comes from two separate sources. The so-known *suspension thermal noise*, which dominates up to 30 Hz and is caused by dissipation in the cables used to hang the optics, is the first. The second source of thermal noise is caused by dissipation processes inside the mirrors themselves. The thermal noise originated by the coating layers deposited on the surfaces of the core optics to make them highly reflective (Acernese, F. *et al.* 2015*b*), also known as *mirror thermal noise*, limits the detector's sensitivity in the frequency range from 30 Hz to 300 Hz.

The horizontal and vertical oscillations caused by the pendulum design and the violin modes of the fibers suspending the mirrors are the three contributors to the suspension thermal noise. The mechanical losses associated with suspension ϕ are the outcome of losses of various types, including material intrinsic losses, thermoelastic losses resulting from the expansion coefficient of the material, losses associated with external pollution on surfaces, and, finally, losses associated with the coupling system between mirror and fibers.

The Fluctuation-Dissipation Theorem states that mechanical loss in suspensions must be minimized in order to reduce thermal noise. When a pendulum is moved horizontally from its rest position, the lossless gravitational field acts as a constant spring to produce a restoring force. Due to the ratio of elastic to gravitational energy, or the so-called dilution factor, the overall losses of

the suspension may be less than those of the material of which it is constituted.

The mechanism works differently in the vertical direction; if the mass is moved vertically, the restoring elastic force of the fiber acts on the mirror as a simple harmonic oscillator motion, with a frequency determined by the elastic spring constant associated with the elongation of the wire. Then, stress on the suspension wires causes them to behave like vibrating ropes, moulding the violin modes into a nearly harmonic sequence (Nardecchia 2022).

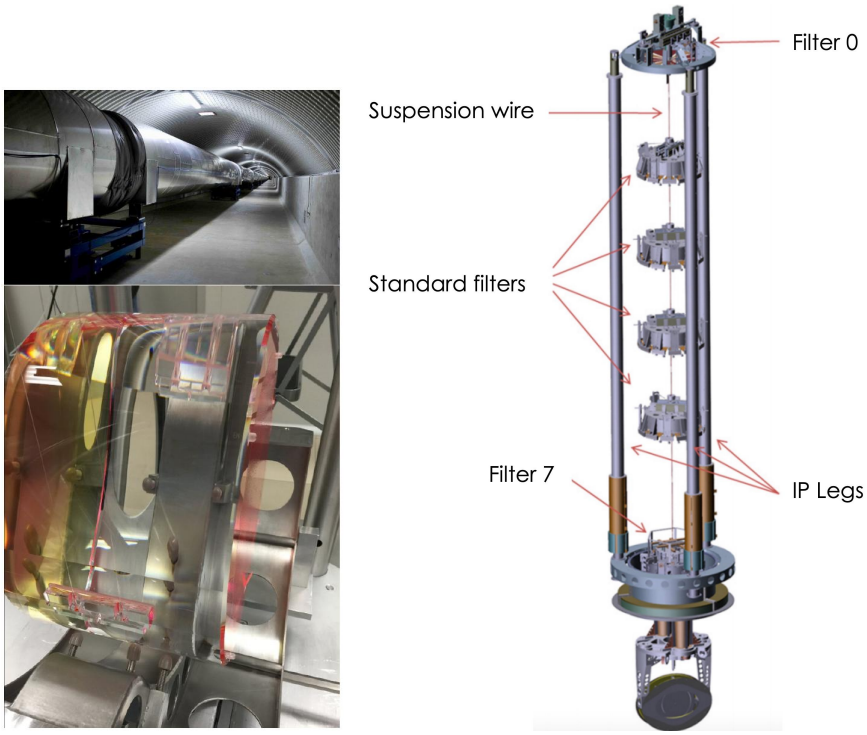

(a) (b)

Figure 3.4: Illustration of Advanced VIRGO construction (*VIRGO website* n.d.): (a) vacuum tube of one of the interferometer arms and suspension of a mirror. Note the two very thin glass wires suspensions attached to the mirror side employed to reduce the suspension thermal noise; (b) the superattenuator is a multistage mechanical filter used for the attenuation of the ground vibration.

According to the Fluctuation-Dissipation Theorem, the thermal noise power spectrum density is determined by:

$$\tilde{x}^2(w) = \frac{4k_B T t_C}{\omega^2} \mathbb{R}\left[\frac{1}{Z(\omega)}\right] \tag{3.6}$$

where $Z(w)$ is the system's impedance, whose real part is fuction of ϕ, the so-known *loss angle parameter*, which measures the material's internal friction's dissipative process.

The coating thermal noise power spectral density can be described also by (Steinlechner 2018)

$$h_B(f) \propto \frac{k_B T t_C}{\omega^2 f} \frac{1-\sigma^2}{Y} \phi = \frac{2k_B T t_C}{\pi^2 f Y_{sub} \omega^2} \left(\frac{Y_{coat}}{Y_{sub}} \phi_{\parallel} + \frac{Y_{sub}}{Y_{coat}} \phi_{\perp} \right) \tag{3.7}$$

where:

- w is the laser beam size on the mirror,
- k_B the Boltzmann constant,
- t_c the total coating thickness,
- σ its Poisson ratio, which measures the deformation of a material in the perpendicular direction to that the force responsible for the stress is applied,
- Y its Young's modulusof the coating and substrate materials, which indicates the mechanical property that measures the elasticity or compression of a material when a force is applied longitudinally,
- T its temperature,
- and $\phi_{\parallel}$ and $\phi_{\perp}$ the mechanical losses of the coating parallel and perpendicular to the coating layers.

Thermal noise is a frequency-dependent effect that becomes increasingly important at low frequencies. It is given in terms of amplitude spectral density $\sqrt{h_B(f)}$ since GW detection is sensitive to amplitude changes rather than intensity variations.

Decreasing Brownian noise by lowering the temperature to cryogenic values, optimizing the laser beam of the interferometer and working on the design of the coatings implies the use of mirrors characterized by specific properties (Pierro, V. *et al.* 2021). In general, multi-material optical coatings are a promising solution because they are able to meet the requirements, in terms of transmittance, absorbance and thermal noise, of the new generation gravitational wave detector mirrors (Pierro, V. *et al.* 2021).

3.4.1 Laser beam diameter

From the parameters involved in the definition of 3.6 it is clear when averaging across a wider surface area, thermal noise is reduced (It is proportional to $1/\omega$ with ω the beam diameter on the mirror). The laser beam has a Gaussian distribution, and its radius is determined by the distance from its center where it decrease to $1/e^2 \approx 13.5\%$. n order to reduce optical losses caused by the outside portions of the beam being outside the mirror, the mirror diameter is set to be roughly $3 \times \omega$.

The aLIGO mirrors have a diameter of 34 cm, a thickness of 40 cm, a mass of 20 kg, and a beam radius of 6.2 cm on the end mirrors of the interferometer arms. They are composed of fused silica. An increase in beam diameter is projected for next gravitational-wave detectors; for instance, the Einstein Telescope is estimated to have a diameter between 45 cm and 62 cm. The availability of large substrates and the capacity to create coatings on a wide scale with the necessary uniformity are the limitations on the mirror size from the standpoint of material development.

3.4.2 Temperature of the test-mass mirror

From the equation 3.6 it can be deduced that a direct reduction of the Brownian noise can occur as a result of a reduction of the absolute temperature T, i.e. through the cooling of the mirrors. It is estimated that the Japanese detector KAGRA will be the first new generation interferometer to operate at the lowest temperature ever used, i.e. at 20K. Future detectors like the Einstein Tele-

scope and LIGO Voyager also plan to function in colder temperatures. In reality this technique is not the best as the mechanical losses of some materials are strongly dependent on the temperature. For instance, the mechanical loss of fused silica, the presently utilized test bulk substrate material, increases by many orders of magnitude at cryogenic temperatures. Therefore, alternative materials are being studied with a low mechanical loss at low temperatures such as crystalline silicon which has a very high thermal conductivity and zero thermal expansion at 18K and 120K, and therefore low thermoelastic noise. Silicon is not transparent at 1064 nm. Thus, the silicon test masses require wavelength modification, specifically switching to the telecom wavelength, 1550 nm, due to available high power lasers and optical components; but a change in wavelength results in a changed coating thickness. As a result, the enhancement does not meet the needs of prospective gravitational wave detectors.

3.4.3 Periodic Double-Layer Coatings

The design of highly reflective coatings can be thought of as a cascade of pairs of materials that alternate according to the different refractive index by which they are characterized. The reflectivity increases by increasing the difference that exists between the refractive indices of the materials used and by increasing the number of layers [3]. The coating design is of the Bragg lattice type. The layers of material are repeated periodically with an individual optical thickness equal to a quarter of the wavelength in this way, with a limited number of layers, the reflectivity of the coating is increased. Typically the coating is made from an odd number of layers in which the first and last are chosen to have a high refractive index. From the latter it is possible to determine the thickness of the layers that can be used to reduce thermal noise by adjuting it. Its effect is zero compared to the oscillations and vibrations caused by other properties such as mechanical losses and optical absorption (discussed in the following sections). The optical absorption represents the ability of a material to absorb the energy associated with the electromagnetic radiation that propagates within it. It does not have a direct effect on Brownian noise

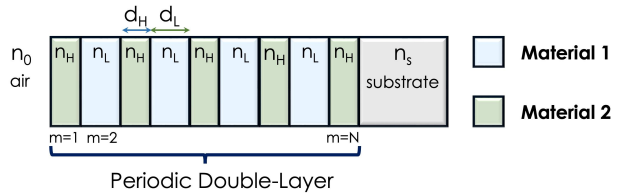

Figure 3.5: Schematic of Periodic Double-Layer Coatings comprised of N layers with alternating high and low refractive indices, indicated as n_H and n_L , and deposited on a substrate with n_s refractive index. As the layer index m rises from left to right, $m = 0$ corresponds to the leftmost vacuum half-space.

but leads to an increase in the temperature of the test masses.

The reflectivity R in a multilayer structure in air or vacuum of two materials n_H and n_L on a substrate with refractive index n_S is given by the following equation:

$$R_{2N} = \left(\frac{n_S \left(n_H/n_L\right)^{2N} - 1}{n_S \left(n_H/n_L\right)^{2N} + 1} \right)^2 \tag{3.8}$$

and

$$R_{2N+1} = \left(\frac{n_H^2 \left(n_H/n_L\right)^{2N} - n_S}{n_H^2 \left(n_H/n_L\right)^{2N} + n_S} \right)^2 \tag{3.9}$$

where it is indicated with N, n_S, n_H, and n_L respectively the total number (even in 3.8 and uneven in 3.9) of layers and the refractive index of the substrate, the *high* refractive index and the *low* refractive index materials used. An exemplary representation is given by Figure 3.5 , in which two generic materials are visible, named for simplicity 1 and 2, which alternate with different refractive indices n_H and n_L starting from the substrate. In the figure in question, the thicknesses of the individual layers can also be identified, such as d_1 relating to the first layer, and the number m of the layers that make up the coating. These equations also demonstrate that the value of R rises with rising values of n_H/n_L, meaning that for higher values of n_H/n_L, fewer bilayers are needed to produce a given value of R. The least amount of layers are used in this design to achieve the required reflectance, however

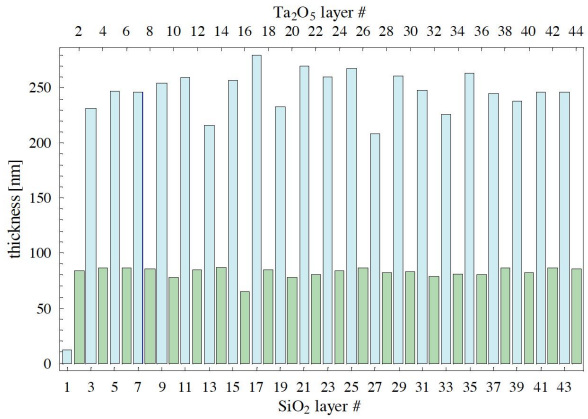

Figure 3.6: Prototype of a genetically engineered mirror (best design after 10^5 GA generations). Design objectives: Transmissivity $1-|\Gamma|^2 \leq 15$ ppm; Ta_2O_5thickness $\leq 80\%$ of the quantity utilized in the closest-reflecting standard QWL design.

it does not produce the least amount of noise among all feasible iso-reflective designs. (Agresti, J. *et al.* 2006). The use of more complex coating designs is frequently justified in practice; for instance, the aLIGO does not employ the ideal quarter-wavelength-thick layers design in order to attain a certain reflectivity at two wavelengths. It was suggested, further investigated, and demonstrated that a different design that consists of a stack of identical doublets with non-quarter-wave layers, with the exception of the terminal top/bottom doublets, outperforms the traditional quarter wavelength design. (Pierro, V. *et al.* 2019) In Figure 3.7a is displayed a multi-layer coating comprised of $2N + 1 = 13$ alternating layers of SiO_2 ($n_L = 1.5$, blue) and Ta_2O_5 ($n_H = 2.05$, green) on a fused silica substrate ($n_S = 1.5$, blue). The laser light intensity for a light field arriving from the left is depicted by the dark blue line. This yields a reflectivity of $R = 96.69\%$ using the equations 3.8 and 3.9. The reflectivity of the coating is shown in Figure 3.7b as a function of wavelength.

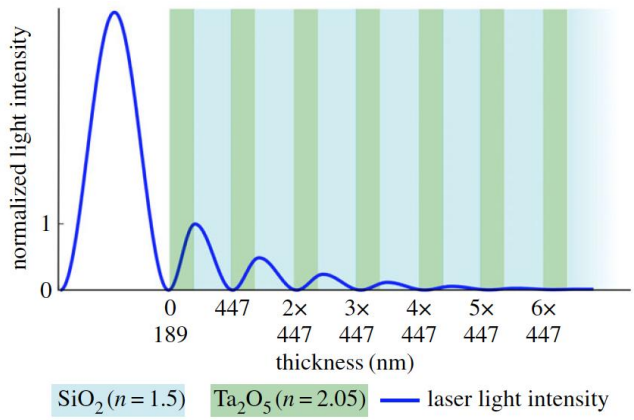

(a) Light intensity (blue line) within a highly reflective multi-layer coating comprised of 13 layers of two alternating materials (SiO_2 in blue and Ta_2O_5 in green) each with an optical thickness of a quarter of a wavelength and deposited on a SiO_2 substrate (fading blue on the right side). The light field is coming from an air or vacuum environment from the left.

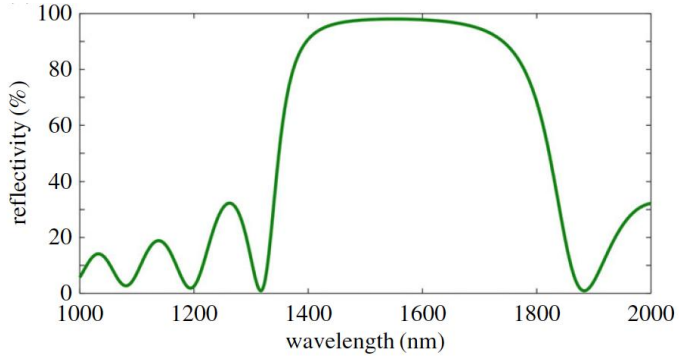

(b) Percent Reflectivity of the coating versus laser wavelength. At the design wavelength of 1550 nm the reflection is maximal.

Figure 3.7: Light intensity and Reflectivity of Periodic Double-Layer Coatings

3.4.4 Mechanical loss of the coating materials

Glass-type amorphous oxides are the category of materials most used in gravitational interferometers. This is because they guar-

antee the minimum optical absorption and therefore the minimum absorption coefficient, as well as ensuring a reduced value of thermal noise. Studying the microscopic mechanisms causing the mechanical loss is a significant area of research due to the relation between the mechanical loss and the atomic-scale structure of the amorphous coating materials.

Thermal noise is proportional to the square root of the mechanical loss ϕ, which is a material property. The phase delay between a stress being applied to a material and the ensuing strain is known as mechanical loss, often known as internal friction. The mechanical loss for a resonant system is inversely proportional to the resonance quality factor and the amount of energy lost during each oscillation cycle from a vibrational mode.

Since thermal noise strongly depends on mechanical losses, the choice of materials is performed considering the following formula for the coating loss angle (Principe 2015):

$$\phi_c = b_L Z_H + b_H Z_H \tag{3.10}$$

where $Z_{L,H}$ is the result of the total number of layers multiplied by the thickness of the individual layers (composed of materials with different refractive index). While the parameter $b_{L,H}$ is the specific mechanical loss given by the relation

$$b_{L,H} = \frac{\lambda_0}{\sqrt{\pi}\omega} \frac{\phi_{L,H}}{n_{L,H}} \left(\frac{Y_{L,H}}{Y_S} + \frac{Y_S}{Y_{L,H}} \right) \tag{3.11}$$

With $\phi_{L,H}$ we indicate the mechanical losses of the layers in which there is the alternation of materials with the lower n_L and higher n_H index material, while λ_0 is the operating wavelength.

Due to the relationship expressed in equation (2.3), the silicon dioxide is the most used low index material in interferometers and Ta_2O_5 , which alternates with SiO_2, the high index material. Considering again figure 15 it means replacing Ta_2O_5 in place of material 1 and silicon dioxide in place of material 2 as in figure 16 below:

The combination of SiO_2 and Ta_2O_5 materials is the choise, for example, for the LIGO detector in which, however, greater mechanical losses in the layers made with tantalum pentoxide, where

variations in the mechanical loss substantially relate with changes in the medium-range atomic ordering, than in the layers obtained from silica have been identified at room temperature. In fact, in the Laboratoire Materiaux Avancè, located in Lyon in France, an improvement in mechanical losses was achieved by incorporating the titanium dioxide TiO_2 within the layers of tantalum pentoxide Ta_2O_5. This combination was mainly used in the construction of the Advanced LIGO and Advanced VIRGO interferometers. With this modification it was possible to achieve a 40% reduction in mechanical losses.

Analyzing the mechanical loss at different temperatures of SiO_2- and TiO_2-doped $Ta_2O_5(TiO_2 : Ta_2O_5)$ it can be seen the following.

- At *room temperature* (290 K), the mechanical loss of TiO_2:Ta_2O_5 is significantly larger than that of SiO_2, to minimize coating thermal noise at room temperature, Ta_2O_5 should be replaced or improved.

- As *temperature decreases*, both materials' mechanical loss rises.

- For upcoming cryogenic detectors like the Einstein Telescope, coating enhancement must focus on both the TiO_2:Ta_2O_5 and SiO_2materials since at 20K, their mechanical losses are almost equivalent.

As anticipated, a material considered a valid substitute for $TiO_2 : Ta_2O_5$ in gravitational interferometers is amorphous silicon (a-Si). At room temperature, mechanical losses for a-Si deposited using the *ion beam sputtering (IBS)*-coating deposition method are between those of SiO_2 and TiO_2:Ta_2O_5, but they fall down at lower temperatures, with a mechanical loss of 40% below that of TiO_2:Ta_2O_5 at 20 K.

3.5 Technical Noise Sources

In addition to the noises seen so far, the performance of the detector is also affected by further disturbances, or so-called technical

noises, which must be reduced using cutting-edge technology. The interferometer's lock and alignment-related control noises make up the majority of technical noises. The scattered light, or diffused light caused by flaws in the optics surfaces, which is dispersed out along the main laser beam path and introduces extra noise in the detector signals, is another of the most restricting noise in low-medium frequency range.

The optical benches holding the optical systems devoted to injecting the beam into the detector, monitoring its performance, and extracting the GW signals are separated from the ground in a manner that simulate the operation of the core optics suspensions in order to decrease this spurious light. Furthermore, there are certain baffles constructed of absorbing materials that surround the core optics and light dumpers are scattered across the optical benches to smother spurious beams. Another important factor in the placement of GW detectors within the biggest vacuum chambers in the world is the minimization of diffused light. This in order to lessen the refractive index variation brought on by the existence of residual air molecules, so that the light actually propagates via the interferometer into ultra high vacuum pipes.

Chapter 4

Improve the sensitivity of the GWs Interferometer

A typical challenge is the optimization of the mirrors for GW detectors. In the case of mirrors for GW detectors, it is important to discover a mirror configuration that produces the least amount of extra (thermal) noise on the detection channel in addition to the typical mirror optimization design request of achieving high reflectance in a given frequency and angle range. Therefore, it's crucial to lower the thermal noise loss angle $\bar{\phi}_c$ as well as the power transmittance $\tau_c = 1 - |\Gamma_c|^2$.

As a result, a simple formulation of the coating optimization problem for the design of low noise dielectric mirrors can involve looking for the sequence of thicknesses of the selected materials that make up the mirrors that minimizes the thermal noise while maintaining the transmittance below a specified threshold value τ_{ref}. To improve the multilayers structures performance, It has been formulated and solved another design that consist in discovering (synthesizing and optimizing) improved materials that have increased optical contrast, fewer optical and mechanical losses and enabling the achievement of a specified transmittance with fewer layers, resulting into thinner coatings and lower noise and giving up the constraint of having only two constituent materials and, then, introducing new ternary multimaterial design. Futhermore, none of the materials present in nature and studied at this time qualifies as a straight substitute for the materials currently in use

with the highest optical losses (TiO_2-doped Ta_2O_5 in current setups), but a few of them are better in terms of some properties (e.g., optical density, and/or mechanical losses), while unfortunately worse regarding others. The optimal material can be synthetized by using *Nanolayered structure* (NL) with thickness and equivalent refractive index that must be choosen ad hoc to fulfill the imposed conditions: at this scope it has been introduced a novelty homogeneization procedure based on an established technique, the *Abelès method*. Furthermore, the NL strategy is expected to be extremely useful in increasing the crystallization temperature of the overall coating, thus allowing for higher temperature annealing with possibly beneficial consequences on the optical and mechanical properties of the final mirror.

4.0.1 The thermal noise model

The power spectral density of coating thermal noise is provided, as we have already defined in 3.6, under certain approximations, by

$$S^B_{coat} = \frac{2k_BT}{f\pi^{3/2}} \frac{1-\sigma_s^2}{wY_s}\phi_c \tag{4.1}$$

where f is the frequency, T is the (absolute) temperature, w is the (assumed Gaussian) laser-beam waist, and σ_s and Y_s are the Poisson and Young modulus of the substrate, and the coating loss angle ϕ_c is

$$\phi_c = \sum_{m=1}^{N_L} \eta_m d_m \tag{4.2}$$

where

$$\eta_m = \frac{1}{\sqrt{\pi}w}\phi_m \left(\frac{Y_m}{Y_s} + \frac{Y_s}{Y_m}\right) \tag{4.3}$$

in which the mechanical loss angle and the Young's modulus of the m-th layer, respectively, are denoted by the symbols ϕ_m and Y_m.

The coating structure which is currently used in Virgo/LIGO test masses (Pinard, L. *et al.* 2017), which consists of alternating quarter-wavelength layers of silicon and titania-doped tantala placed on a fused silica substrate, is taken into consideration for

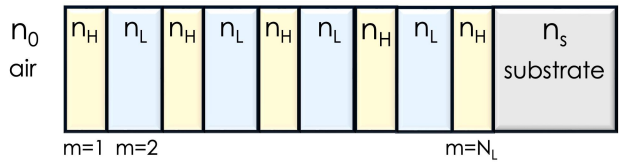

Figure 4.1: Schematic of Periodic Double-Layer Coatings comprised of N_L layers with alternating high and low refractive indices, indicated as n_H and n_L , and deposited on a substrate with n_s refractive index. As the layer index m rises from left to right, $m = 0$ corresponds to the leftmost vacuum half-space.

comparison with the optimum designs. Note that, the targeted transmittance value τ_{ref} should be typically a few parts per million (henceforth ppm), in the following is chosen to be 6 ppm, and the targeted absorbance value is $\alpha_{ref} \leq 1$ ppm. The loss angle of the admissible optimization solutions must be scaled to that of the reference LIGO- or Virgo-like design, consisting of $N_T = 36$ alternating HL layers, for which

$$\phi_c = \phi_c^{ref} = 18 \frac{\eta_L \lambda_0}{4Re(n_L)} (1 + \gamma_H) \tag{4.4}$$

4.1 Optimization of the layers' thicknesses

This section is focused on the reduction of the coating loss angle ϕ_c by optimizing the layer thicknesses introducing a multiobjective optimization approach (Emmerich & Deutz 2018):the thickness sequences are sought which simultaneously minimize the transmittance and the loss angle. The suffixes S,L,H are used to identify substrate (S), low (L) and high (H) index material, respectively, of the coating structure sketched in Figure 4.1 consisting of N_L layers beginning with the high refractive index materials at the vacuum/coating interface.

As a consequence it is

$$\begin{cases} n^{(m)} = n_H - ik_H, & m \text{ odd}, & n^{(m)} = n_L - ik_L, & m \text{ even}; \\ \phi_m = \phi_H, & m \text{ odd}, & \phi_m = \phi_L, & m \text{ even}; \\ Y_m = Y_H, & m \text{ odd}, & Y_m = Y_L, & m \text{ even}. \end{cases} \tag{4.5}$$

The coating noise angle becomes:

$$\phi_c = \eta_H \sum_{m \in J_o} d_m + \eta_L \sum_{m \in J_e} d_m, \tag{4.6}$$

where

The problem in non-standard mathematical notation can be expressed:

$$\begin{array}{ll} \text{Minimize} & [\bar{\phi_c}, \tau_c] \\ z_1, \ldots, z_{N_L} \in \Omega & \end{array} . \tag{4.7}$$

Finding the Pareto front, or tradeoff curve, in the $[\bar{\phi_c}, \tau_c]$ plane is necessary to solve this problem within the context of multiobjective optimization. A series $z_m, m = 1, \ldots, N_L$ of layer normalized thicknesses refers to each point on the Pareto front.

The notion of dominance, which is an appropriate ordering rule in the $[\bar{\phi_c}, \tau_c]$ plane, must be introduced in order to establish the Pareto front. A reasonable solution A in the space $[\bar{\phi_c}, \tau_c]$ that is physically possible is dominated by another (different) physically reasonable solution B if the coordinates of A are orderly greater than B. Therefore, the collection of physically possible solutions for which there is no physically feasible dominating solution is the Pareto front of the multiobjective optimization problem. To address the issue of Pareto front computing for large dimensional issues, a variety of methods based on various global multiobjective optimization tools are available, employing an appropriate sampling technique of the physically viable configuration space (e.g. NSGA-II, NSGA-III, B-MOEA etc.). It is used a state of the art, public domain *Multi Objective Evolutionary Algorithm (MOEA)* named *Borg MOEA* (Hadka & Reed 2013), that uses an evolutionary strategy appropriate for continuous variables.

It has been used a state of the art, open-source *Multi Objective Evolutionary Algorithm (MOEA)* known as *Borg MOEA*,

which employs an evolutionary approach suitable for continuous variables.

Unlike common optimization algorithms that use mutation, crossover, and selection operators, which do not change during the execution program, the BorgMOEA adopts different operators and adaptively on the basis of their search success: evaluate progress, adapt population size and increase the archive with new solutions. These characteristics allow the algorithm to advance and keep it from being stuck in some loops for the duration of the run. It is compared to reference solutions, the goodness of the numerical solutions provided by the Borg MOEA.

4.1.1 Evolutionary Algorithm

The selection probability is proportional to the quality of the represented solution, or to the fitness function to be optimized, in order to solve optimization problems with an evolutionary algorithm. Individuals of a population are associated with a physical solution of a given problem (in our case, the layer thicknesses sequence) by the encoding procedure. The population then experiences crossover selection and mutation (similar to natural genetic evolution), giving rise to new offspring and adjourning the population. Over several generations, the procedure is repeated until a satisfactory termination criterion is attained. Based on the value of its goal function, each person encoding a potential solution is given a fitness value, and the fitter people are given a better opportunity to mate and produce additional fitter individuals.

The same general structure governs the multi-objective version of the evolutionary algorithm, with the inclusion of an appropriate Pareto front extraction method. The fundamental structure shown in Figure 4.2 is followed by a Multi-Objective Evolutionary Algorithm.

4.1.2 Numerical solution of multiobjective optimization problem

Table 4.1 summarizes the physical parameters of the coating and substrate employed in the simulations.

Result: Pareto front of population
initialize random population $P(0)$, at the iteration $t = 0$;
find fitness of initial population;
extraction of Pareto front elements;
while *termination criteria is not reached* **do**
    parent selection;
    crossover of the parent;
    mutation;
    decode and fitness calculation;
    survivor selection and update population $P(t+1)$;
    extraction of Pareto front elements from $P(t+1)$;
    increment t;
return Pareto fronts;

Figure 4.2: Multi-Objective evolutionary algorithm

	L	**H**	**Substrate**
	SiO_2	TiO_2:Ta_2O_5	bulk crystalline SiO_2
n_r	1.45	2.1	1.45
κ	10^{-11}	2×10^{-8}	10^{-11}
$Y(GPa)$	72	140	72
ϕ	5.00×10^{-11}	3.76×10^{-4}	7.00×10^{-8}
γ		9.5	

Table 4.1: Physical parameters of coating and substrate materials employed in simulations, for which temperature $T = 300K$ and free space wavelength $\lambda_0 = 1064nm$.

In order to investigate the optimal structure, it has been computed the Pareto fronts for the cases N_L ranging from 11 to 19 with step 2, Figure 4.3a. The Pareto fronts are shown to have numerous hillocks, the number of which is equivalent to the number of layers N_D of high refractive index materials. In the lower transmittance region, the hills are less noticeable. For the case $N_L = 19$ it has been indicated with $N_b = 1, 2, 3$ the last three hillocks and in Figure 4.3b, c, d it has been displayed, for this three case, the thicknesses as a function of layer index m. Furthermore, the red circle marks match thequarter wavelength design, QWL. The normalized layer thicknesses z_m of the high (low) refraction index material are given by the height of vertical light blue (yellow) bars.

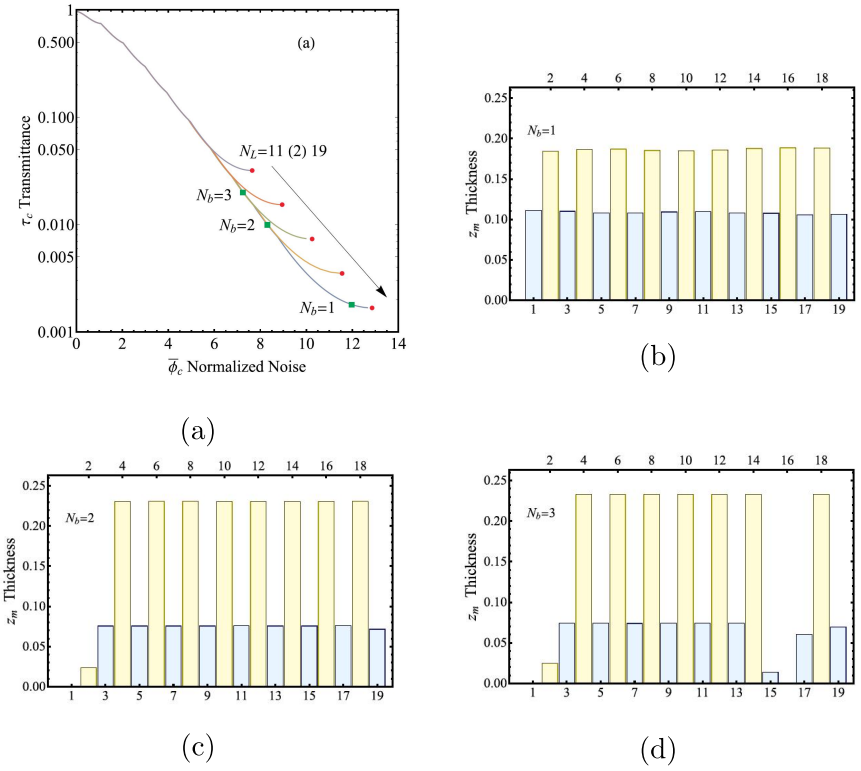

Figure 4.3: (a) Pareto fronts for scenario $N_L = 11(2)19$. The high transmittance section of the curve clearly demonstrates the hillock-like structure of Pareto fronts. The last three hillocks for the scenario $N_L = 19$ are highlighted with $N_b = 1, 2, 3$. The quarter wavelength design is shown by the red circle markings. (b,c,d) Thicknesses for the green square markers that correlate to the hillocks $N_b = 1, 2, 3$ as a function of layer index m. The normalized layer thicknesses z_m of the high (low) refraction index material are shown by the height of the vertical light blue (yellow) bars.

It can be noted that:

- a mirror arrangement with layer thicknesses that are all different from zero corresponds at the hillock with lowest transmittance ($N_b = 1$), see Figure 4.3c, and also corresponds to the QWL design at the operating wavelength $\lambda_0 = 1064nm$

with $N_L = 19$ (the rightmost red point in Figure 4.3a). This is consistent with the widely recognized QWL design characteristic of minimizing transmittance in the case of multilayer reflectors built of negligibly absorbing materials. (Carniglia & Apfel 1980).

- The thickness of the first high refractive index layer in the mirror design represented by the following hillock $N_b = 2$ has essentially been adjusted to zero. (see Figure 4.3c).
- For the case $N_b = 3$ illustrated in Figure 4.3d, in addition to the first layer, another layer of low index material, layer 16, has a thickness of zero, which suggests that two layers of high refractive index material right next to itself combine and become one layer.

It has been founded that the behavior described above is applicable to all hillocks, meaning that the generic hillock $N_b = k$ roughly resembles a multilayer structure with $N_D - k + 1$ layers of high refractive index. Basically, continuous, decreasing, and non-convex (hillocky) curves are a general property of the Pareto front of dielectric mirror multiobjective optimization. In order to investigate design configurations that demonstrate performances of possible interest for current GW interferometer detectors, the Pareto curves (blue lines) for N_L ranging from 11 to 39 with step 4 are shown in Figure 4.4. Simulations for coating have been run using the physical parameters listed in Table 4.1.

Also in this case the red points are the QWL design which are situated on a curve that, with appropriate approximations, may be expressed as a straight line in the $[\bar{\phi_c}, \tau_c]$ plane's log-linear axis scale. Indeed, the reflectivity of a quarter wavelength multilayer made of $N_L = 2N_D - 1$ alternating layers with high and low refractive indexes, respectively, placed on a substrate with refractive index $n_s = n_L$ is:

$$|\Gamma_c|^2 = \frac{\left(1 - n_L \left(\frac{n_H}{n_L}\right)^{2N_D}\right)^2}{\left(1 + n_L \left(\frac{n_H}{n_L}\right)^{2N_D}\right)^2} \tag{4.8}$$

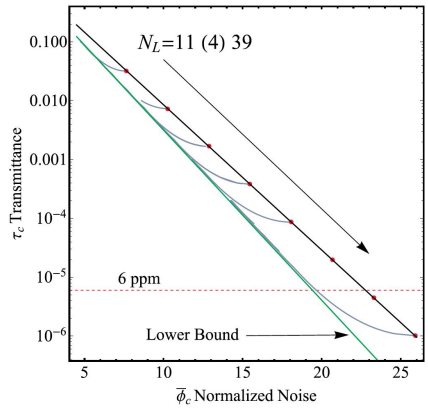

Figure 4.4: Pareto fronts for $N_L = 11(4)39$ in logarithmic-linear scale (blue curves). In Table 4.1, the simulation parameters are listed. Referring to the QWL design are red circle marks. The standard design objective for 2nd generation (advanced) Virgo-LIGO detectors is the dashed red horizontal grid line at $\tau_c = 6ppm$.

where $n_H/n_L \geq 1$. In view of eq. 4.8 the transmittance $\tau_c = 1 - |\Gamma_c|^2$ reads:

$$\tau_c = \frac{4n_L \left(\frac{n_H}{n_L}\right)^{2N_D}}{\left(1 + n_L \left(\frac{n_H}{n_L}\right)^{2N_D}\right)^2} \tag{4.9}$$

that can be written as

$$\tau_c = \frac{\frac{4}{n_L} \left(\frac{n_H}{n_L}\right)^{-2N_D}}{\left(1 + \frac{1}{n_L} \left(\frac{n_H}{n_L}\right)^{2N_D}\right)^2} \tag{4.10}$$

For $\frac{1}{n_L} \left(\frac{n_H}{n_L}\right)^{2N_D} \ll 1$, by applying the long on both side of equation 4.10 we get

$$\log(\tau_c) \sim \log\left(\frac{4}{n_L}\right) - 2N_D \log\left(\frac{n_H}{n_L}\right). \tag{4.11}$$

For the QWL design, however, specializing eq. 4.6, the normalized loss angle $\bar{\phi_c}$ may be expressed as a function of N_D

$$\bar{\phi_c} = \frac{\gamma N_D}{4n_H} + \frac{N_D - 1}{4n_L} = \left(\frac{\gamma}{4n_H} + \frac{1}{4n_L} N_D - \frac{1}{4n_L}. \right) \tag{4.12}$$

Solving 4.12 for N_D and connecting eq. 4.11:

$$\log(\tau_c) \sim \log\left(\frac{4}{n_L}\right) - 2\frac{2n_H}{\gamma n_L + n_H} \log\left(\frac{n_H}{n_L}\right) - \bar{\phi_c}\frac{8n_L n_H}{\gamma n_L + n_H} \log\left(\frac{n_H}{n_L}\right) \tag{4.13}$$

That is the straight line equation. In the plane $[\bar{\phi_c}, \tau_c]$ with a log-linear axes scale, the tradeoff curves asymptotically locate close to the straight line eq. 4.13 (green line in Figure 4.4). When Pareto front data are used to do regression, the noise ratio coefficient is decreased to an *effective* value $\gamma_e = 7.9$.

For the values listed in Table 4.1, it has been hypothesized that this curve is a lower bound for all tradeoff curves in the region of low transmittance ($\tau_c \leq 0.1$) above the Koppelmann limit (Koppelmann 1960), that is placed at $\tau_c \sim 10^{-7}$. The normalized energy absorption (assorbance) order of magnitude in each design is also known as the Koppelmann limit. The reference design is the QWL coating with $N_L = 35$ because it meets the goal transmittance ($\tau_c = 6ppm$) with the least amount of normalized noise. In contrast to the quarter wavelength reference design, it is evident that each tradeoff curve with $N_L \geq 35$ comprises layer configurations that meet the requirement $\tau_c \leq 6ppm$ and exhibit lower normalized noise $\bar{\phi_c}$.

The configurations with $N_L = 39, 41, 43$ that matches are shown in Figure 4.5 yields a normalized noise reduction with respect to the QWL reference design of about $15.5\%, 15.9\%$ and 15.9% respectively. Note that the designs reported in Figure 4.5a and b belong to the first hillock of the tradeoff curves $N_L = 39, 41$ respectively, while the configuration in Figure 4.5c belongs to the second hillock of the Pareto front $N_L = 43$.

Furthermore, observe that, with the exception of the first two layers and the last one, the thickness sequences resemble a truncated periodic structure. The interior layers with high and low refractive index materials have normalized physical lengths of $z_H \sim$

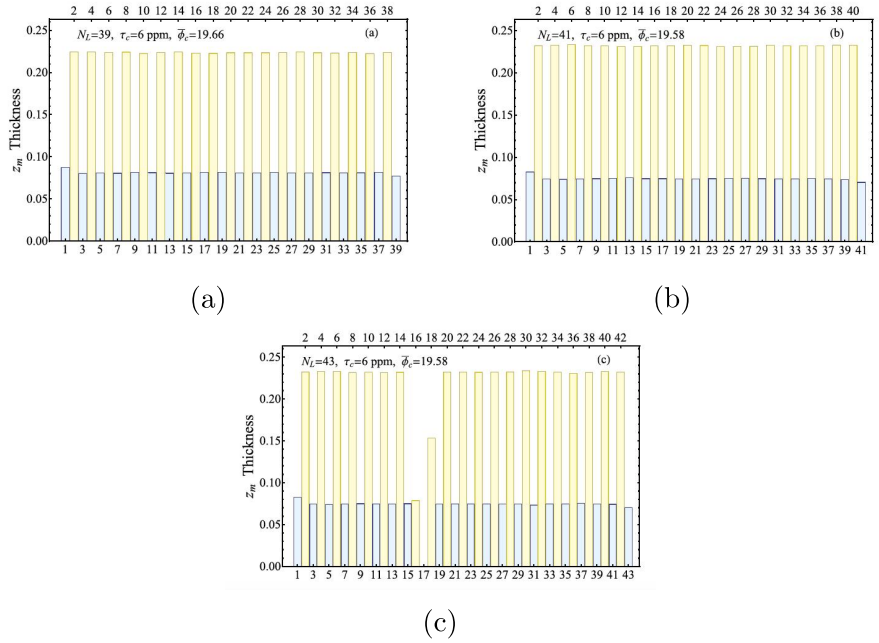

Figure 4.5: Thicknesses as a function of layer index m for the cases $N_L = 39, 41, 43$, respectively. The height of vertical light blue (yellow) bars gives the normalized layer thicknesses z_m of the high (low) refraction index material. The horizontal line (dashed line in Figure 4.4) made at the required transmittance level A ($\tau = 6ppm$) intersects with the points obtained from the intersection of the Pareto boundary.

0.081 and $z_L \sim 0.22$, respectively. These lengths correspond to normalized optical lengths of $n_H z_H \sim 0.17$ and $n_L z_L \sim 0.32$, whose sum is less than 0.5. All of the aforementioned simulations were run while varying the noise ratio coefficient in the range $\gamma \in [7, 10]$ due to the measurement uncertainty of the specific loss angle coefficient. According to Figure 4.6a and b, respectively, the noise reduction of the optimized coating structure in comparison to the reference QWL design and the effective γ_e noise ratio coefficient are provided as functions of γ.

It has been established that the effective noise ratio γ_e and noise reduction (*gain*) are both almost linear, rising functions of the noise ratio coefficient γ.

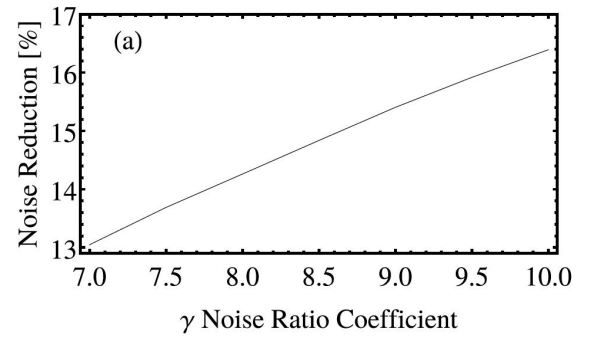

(a)

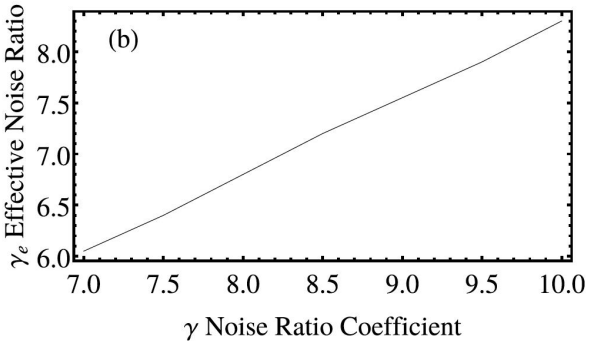

(b)

Figure 4.6: (a) Optimizated coatings percent loss angle reduction in comparison to the reference QWL design. (b) The effective noise ratio coefficient γ_e versus γ.

4.2 Introduction of new materials

As it has be seen, the study of astrophysical processes is possible with these remarkable km-long facilities, but their sensitivity is constrained by much smaller scale physics, particularly laser quantum noise and Brownian motion of the end test masses. This Brownian motion results from internal energy loss in the materials that make up the interferometer's test masses.

The test mass mirrors in GW detectors are made of a high purity SiO_2 substrate covered in a multi-layer stack of highly reflective amorphous oxide thin films. At first, Ta_2O_5 and SiO_2 were used by LIGO and Virgo as the high index and low index

materials, respectively. Later, a combination of Ta_2O_5 and TiO_2 was employed as the high index material by Advanced LIGO and Advanced Virgo. When Ta_2O_5 is doped with 22.5% TiO_2, it was discovered that the mechanical loss in this instance is reduced by 40%.

Over the years, much research has been done to determine if tantalum-based mixed oxide coatings and amorphous metal oxides are suitable for use as low-brownian noise interference coatings for GW detectors (Fazio, M. A. *et al.* 2022). Along with assessing the materials' loss angle, coatings were characterized to determine their optical, structural, and elastic characteristics. The influence of the dopant on the elastic and optical characteristics of the coatings as well as on the mechanical loss has been shown to be correlated with the amorphous morphology of the material.

Recent research has found that among Ta_2O_5-based mixed oxide coatings with low dopant concentrations, the present high index material of TiO_2-doped $Ta_2O_5$is the best option for decreased thermal noise. A thorough knowledge of the characteristics of amorphous materials is essential for the development of future interference coatings that are tuned for low Brownian noise in light of the impending A+Ligo update and the arrival of third generation GW detectors with tougher noise budgets.

A material considered a valid substitute for TiO_2-doped Ta_2O_5 and, therefore, presented as the candidate material for coatings in third generation cryogenic interferometers is Amorphous Silicon (a-Si). The a-Sihas mechanical losses which decrease as the temperature decreases. It is used as a material with a high refractive index, in fact the value varies between 3.5 and 4.0, in order to have a coating made from a few layers and with high reflectivity. A coating made of amorphous silicon and SiO_2reduces the thermal noise by a factor of 2 when compared to the coating made of TiO_2-doped Ta_2O_5 and SiO_2 at 20K temperature (Reid & Martin 2016). This is due to the low mechanical losses and the reduced thickness of the layers. However, the optical absorption of amorphous silicon is high at $1550nm$ (i.e. the wavelength of the laser source of third generation interferometers), and is even higher at $1064nm$, making it unsuitable for gravitational wave detectors. This material is still tested starting from the fact that the optical

absorption is higher when using the Ion Beam Deposition technique. Indeed, different types of deposition processes are being employed, such as ion plating. It is a method in which coatings of materials, usually metallic, are deposited on target surface areas. The material used is ionized and vaporized by means of an electric arc which forces the process at a high speed. This method is commonly performed in a vacuum chamber and has an optical absorption reduction of approximately 1000ppm compared to the IBS deposition technique. Furthermore, the optical absorption of amorphous silicon is reduced by 80% when working at a variable temperature between $400C$ and $500C$ while it decreases by a factor of 2 following the cooling of the interferometric mirrors. Carrying out the deposition processes at elevated temperature, rather than room temperature, has emerged as another solution to reducing optical absorption for the aforementioned material. In this way it is said that an "ideal glass" is formed. To obtain this result, the material must be deposited at an extremely low speed or with a substrate at a high temperature in such a way as to guarantee energy to the atoms in such a way that they are able to rearrange themselves before the deposition of the next layer. In the $a\text{-}Si/SiO_2$ coating combination the mechanical losses of the layers made from silicon dioxide would be problematic. The high refractive index of amorphous silicon allows you to have a wide choice when it comes to replacing silicon dioxide with another material. An example is silicon nitride $SiNx$, a chemical compound of silicon and nitrogen, in which the "x" indicates the variable stoichiometry. Given the low mechanical losses at low temperatures, the combination of amorphous silicon with this material makes the resulting coating better than that achieved by the SiO_2/TiO_2-doped Ta_2O_5 combination. In fact, at a temperature of 20K, there is a significant reduction in thermal noise. The silicon nitride is deposited with the *PECVD* technique, *Plasma Enhanced Chemical Vapor Deposition*, with which the properties of optical absorption, refractive index and mechanical losses are improved. Plasma assisted chemical deposition is the process by which nanometric films are formed by bringing the material from the gaseous to the solid state. In a vacuum chamber, with a pressure that reaches a few Pascals, gases are introduced which are ionized by the elec-

tromagnetic field formed by the presence of some electrodes. The films obtained present a semi-crystalline microstructure without porosity, roughness and therefore extremely homogeneous.

Moreover, detailed investigations of SiN deposited via PECVD have led to evidence of reduced mechanical losses than existing GW-coating materials at room temperature and at low temperatures down to 10K, demonstrating that the precise material composition has a substantial impact on the material characteristics. SiN is deposited using PECVD. A SiN/SiO_2 has optical absorption that is comparable to that of the best $a\text{-}Si/SiO_2$. The possibility of a pure SiN coating in which SiN produces the high and low refractive index layers might also be made possible by the variable refractive index for different concentrations of SiN.

4.2.1 Ternary QWL coatings

A promising and practical solution to satisfy the demanding criteria (in terms of transmittance, absorbance, and thermal noise) is multimaterial optical coatings. Therefore, the focus has been on ternary coatings made up of quarter-wavelength-thick layers, where a third material (H') is added to the two that are currently being used, that is SiO_2 (L) and TiO_2-doped Ta_2O_5 (H). These coatings have higher optical losses but higher dielectric contrast (compared to SiO_2) and lower thermal noise (compared to TiO_2-doped Ta_2O_5). By simulating all conceivable configurations for all values of the optical density and extinction coefficient of the third material, including the case of two putative materials, the best material combinations with the least amount of thermal (Brownian) noise under the prescribed transmittance and absorbance constraints 4.4 were identified. These two extreme paradigms, which it will be refered to as *material A* and *material B*, are comparable to *a-Si* and *SiNx*.

It will be describe numerical experiments that operate at both room temperature and cryogenic temperatures and are based on practical materials, specifically *a-Si*and *SiNx*. The simplest thermal noise model previously described (eq. 4.3) and the transmission matrix formalism (2.6) are the foundations for the simulations. The Transmission matrices $T_m,\ m = 1, 2, \ldots, N_T$, in 2.101,

have the following straightforward form for coatings made up of QWL layers:

$$T_m = i \begin{bmatrix} \sinh\left(\frac{\pi}{2}\frac{\kappa^{(m)}}{n_r^{(m)}}\right) & \frac{1}{n^{(m)}}\cosh\left(\frac{\pi}{2}\frac{\kappa^{(m)}}{n_r^{(m)}}\right) \\ n^{(m)}\cosh\left(\frac{\pi}{2}\frac{\kappa^{(m)}}{n_r^{(m)}}\right) & \sinh\left(\frac{\pi}{2}\frac{\kappa^{(m)}}{n_r^{(m)}}\right) \end{bmatrix} \tag{4.14}$$

where $n^{(m)}$ take values in $n_L, n_H, n_{H'}$. The corresponding single-layer matrices will be denoted as $T_L, T_H \text{and} T_{H'}$ respectively. The material sequences for which $n^{(m)} = n^{(m-1)}$ for some m should be discarded; accordingly, a total of $N_C = 3 \times 2^{N_T-1}$ distinct acceptable ternary coatings consisting of N_T layers QWL are left. Knowledge of the matrix 2.101 yields the coating transmittance and absorbance, as shown in Chapter 2. In order to compute the coating thermal noise, we have

$$\gamma_H = \frac{Re[n_L]}{Re[n_H]}\frac{\eta_H}{\eta_L} = \frac{Re[n_L]}{Re[n_H]}\frac{\phi_H}{\phi_L}\left(\frac{Y_H}{Y_s}+\frac{Y_s}{Y_H}\right)\left(\frac{Y_L}{Y_s}+\frac{Y_s}{Y_L}\right)^{-1}, \tag{4.15}$$

$$\gamma_{H'} = \frac{Re[n_L]}{Re[n_{H'}]}\frac{\eta_{H'}}{\eta_L} = \frac{Re[n_L]}{Re[n_{H'}]}\frac{\phi_{H'}}{\phi_L}\left(\frac{Y_{H'}}{Y_s}+\frac{Y_s}{Y_{H'}}\right)\left(\frac{Y_L}{Y_s}+\frac{Y_s}{Y_L}\right)^{-1}, \tag{4.16}$$

where $\phi_L, \phi_H \text{and} \phi_{H'}$ are the material mechanical loss angles. Hence, using 4.3 and 4.2,

$$\phi_C = \frac{\eta_L \lambda_0}{4Re(n_L)}\left(N_L + \gamma_H N_H + \gamma_{H'} N_{H'}\right), \tag{4.17}$$

$N_L, N_H, \text{and} N_{H'}$ being the number of laters made of the L, H and H' materials, respectively.

Therefore, the goal was to identify the optimal material sequences for a QWL structure, characterized by a minimum thermal noise considering specific transmittance and absorbance constraints, by simulating the possible configurations, for different values of the optical density and the extinction coefficient of the third material.

In this regard, It first was conducted a study on two hypothetical materials (named A and B), evaluating their transmittance and the coating power noise spectral density obtainable.

	Hypothetical Material			Real Material	
	Material A	Material B		*a-Si*	*SiNx*
n_r	3.0	2.1		3.5	2.28
κ	$10^{-6} - 10^{-4}$	$10^{-6} - 10^{-4}$		1.22×10^{-5}	1.51×10^{-5}
Y	100GPa	100GPa		147GPa	103.7GPa
			T		
ϕ	3.76×10^{-4}	10^{-4}	20K	2×10^{-5}	1×10^{-5}
			120K	8×10^{-5}	2×10^{-5}
			290K	10^{-4}	1×10^{-5}
d	$\frac{\lambda}{4 \cdot n_A}$	$\frac{\lambda}{4 \cdot n_B}$		$\frac{\lambda}{4 \cdot n_{aSi}}$	$\frac{\lambda}{4 \cdot n_{SiNx}}$

Table 4.2: Physical parameters of H'-layers used in coating simulations.

Later it was considered the case in which the third material used is a real material, that is the case of amorphous silicon and silicon nitride operating at ambient and cryogenic temperatures.

The model was structured to be composed of three materials L, H and H' according to a certain configuration. For the material L, i.e. the one with the lowest refractive index, $SiO_2$was chosen; while for the material H, which has a higher refractive index, titanium dioxide doped with tantalum oxide was chosen, TiO_2:Ta_2O_5. The multilayers structure is deposed on a SiO_2substrate.

The refractive index, Young's modulus, the mechanical loss angle, the extinction coefficient and the thickness of the materials used for the L-layers, H-layers and substrate are shown in Table 4.1, while the parameters of the H'-layers are reported in Table 4.2.

The air refractive index and substrate refractive index are, respectively, $n_0 = 1$ and $n_s = 1.45$.

	Study Cases	$\kappa_{H'}$	τ_c $[ppm]$	α_c $[ppm]$	$\frac{\phi_c}{\phi_{ref}}$
Hypothetical	$[A\|L]^{10}$	10^{-6}	1.165	0.945	0.3638
Material	$[H\|L]^4[A\|L]^7$	10^{-5}	5.418	0.947	0.4768
A	$[H\|L]^7[A\|L]^6$	10^{-4}	2.510	0.936	0.6071

Table 4.3: Optimal ternary QWL coating using hypothetical material A: numerical values of transmittance, absorbance and loss angle at $\lambda = 1064nm$.

4.2.2 Ternary QWL coating using hypothetical material A

For each of the three possible values of the extinction coefficient ($\kappa_{H'} = 10^{-6}, 10^{-5}, 10^{-4}$), the set of all admissible ternary QWL coatings that satisfy the required transmittance and absorbance constraints using hypothetical material A for *H'* is presented in Table 4.3. In order of increasing transmittance and/or absorbance, they are easily divided into subsets with the same number of $[H|L]$, $[H'|L]$, and $[H'|H]$ doublets and, thus, the same coating loss angle. The best design, with the lowest coating loss angle for all κ_H values taken into account, consists of a stack of $N_{H'}$ doublets $[H'|L]$ grown on top of the substrate, followed by another stack of N_H doublets $[H|L]$. This supports the idea that the field intensity is often low enough close to the substrate to render the comparatively high optical losses of the denser material *H'* negligible. This enables the reduction of the coating's thermal noise and the overall number of layers. Furthermore, the extinction coefficient of the material *H'* affects the optimum values of $N_{H'}$ and N_H.

4.2.3 Ternary QWL coating using hypothetical material B

The total number of high-low index doublets needed to satisfy the specified transmittance constraint in the case of ternary QWL coatings using hypothetical material B remains constant regardless

	Study Cases	$\kappa_{H'}$	τ_c $[ppm]$	α_c $[ppm]$	$\frac{\phi_c}{\phi_{ref}}$
Hypothetical	$[H\|L]^2[B\|L]^{16}$	10^{-6}	1.015	0.958	0.4068
Material	$[H\|L]^5[B\|L]^{13}$	10^{-5}	4.467	0.978	0.5180
B	$[H\|L]^8[B\|L]^{10}$	10^{-4}	4.469	0.998	0.6293

Table 4.4: Optimal ternary QWL coating using hypothetical material B: numerical values of transmittance, absorbance and loss angle at $\lambda = 1064nm$.

of whether the high-index layers are made of material H or H' because they have the same refractive index. Therefore

$$N_H + N_{H'} = N_L = N_L^{(ref)}. \tag{4.18}$$

Using hypothetical material B for H' with $\kappa_{H'} = 10^{-6}, 10^{-5}, 10^{-4}$, the obtained optimum designs are shown in Fig. In this instance as well, a stack of $[H'|L]$ doublets grown on top of the substrate is followed by another stack of $[H|L]$ doublets to create the best design with the lowest thermal noise within the established transmittance and absorbance limits.

4.3 Uncertainties

Quarter wavelength ternary coatings are the optimal solution in the mirrors of gravitational interferometers. To ensure this even in the face of uncertainties and inaccuracies relating to the variability of both the value of the extinction coefficient and the thickness of the layers under examination, another set of Matlab simulations were carried out to demonstrate the robustness of the coatings designs. Initially, analyzes were conducted to demonstrate the robustness of the optimal ternary coating with respect to the uncertainty of the value of the extinction coefficient. For this reason, this coefficient was made to vary randomly and uniformly within the range:

$$\kappa_{H'} \Rightarrow (0.5 \cdot \bar{\kappa}_{H'}, 1.5 \cdot \bar{\kappa}_{H'}) \tag{4.19}$$

The result obtained relates to the distributions of the occurrences of the transmittance and absorbance of the coating in a sample of 10^5 realizations of the optimal ternary coating using, respectively, hypothetical material A, material B and real materials for the layers *H'*.

26-layers $\Rightarrow [H, L]^7[A, L]^6$ with $\kappa_A = 10^{-4}$

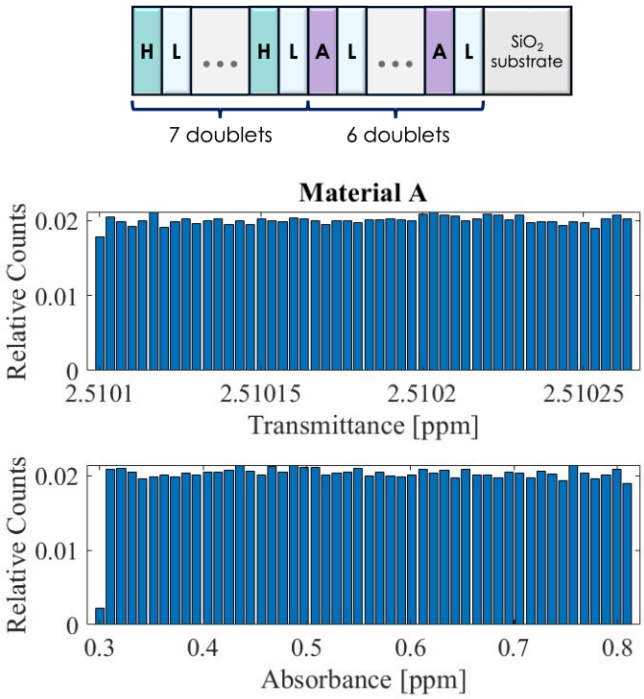

Table 4.5: Optimal ternary QWL coating using material A: distributions of coating transmittance and absorbance in a sample of 10^5 realizations, assuming κ_A to be random uniform in $(0.5 \cdot \bar{\kappa}_A, 1.5 \cdot \bar{\kappa}_A)$, with $\bar{\kappa}_A = 10^{-4}$, and the same for all A layers

Then was conducted the distributions of coating transmittance and absorbance in a sample of 10^5 realizations of the optimal ternary QWL coating where the extinction coefficients of the *H'* layers, $\kappa_{H'}$, are independent identically distributed random variable in $(0.5 \cdot \bar{\kappa}_{H'}, 1.5 \cdot \bar{\kappa}_{H'})$.

36-layers $\Rightarrow [H, L]^5[B, L]^{13}$ with $\kappa_B = 10^{-5}$

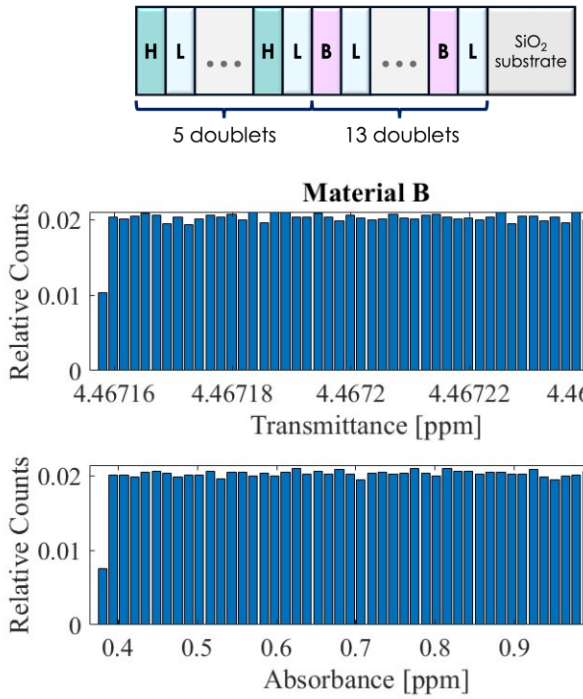

Table 4.6: Optimal ternary QWL coating using material B: distributions of coating transmittance and absorbance in a sample of 10^5 realizations, assuming κ_B to be random uniform in $(0.5 \cdot \bar{\kappa}_B, 1.5 \cdot \bar{\kappa}_B)$, with $\bar{\kappa}_B = 10^{-5}$, and the same for all B layers

Similarly, for real materials, namely amorphous silicon and silicon nitride, the same simulations relating to the uncertainty of the extinction coefficient were carried out.

The deposition processes of the coatings for the mirrors of gravitational interferometers can be a source of uncertainty regarding the thickness of the coating layers. Therefore, due to the technological limitations, the simulations of the distributions of transmittance, absorbance and the loss angle (normalized to the value of the reference binary coating, i.e that relating to the classic coating made by the alternation of SiO_2 and TiO_2:Ta_2O_5) are presented below. It is considered a sample of 10^5 realizations in which the

26-layers $\Rightarrow [H, L]^7[A, L]^6$ with $\kappa_A = 10^{-4}$

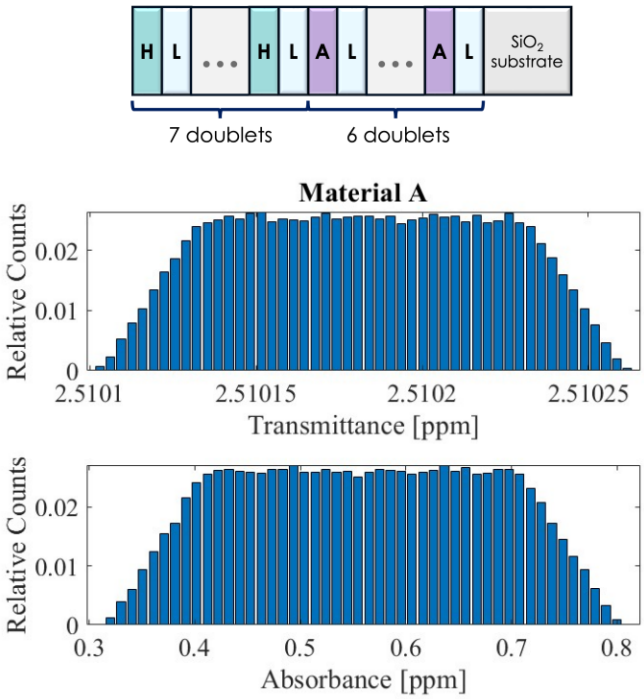

Table 4.7: Optimal ternary QWL coating using material A: distributions of coating transmittance and absorbance in a sample of 10^5 realizations, assuming κ_A to be random uniform in $(0.5 \cdot \bar{\kappa}_A, 1.5 \cdot \bar{\kappa}_A)$, with $\bar{\kappa}_A = 10^{-4}$, and independent identically distributed random variables.

thickness of all the layers is assumed to be a random and independent variable, identically distributed, uniformly, around the nominal thickness of the optimal coating at a quarter wavelength. The thickness variability is defined with respect to a symmetrical interval of size of 2 nm.

Finally, the simulations are repeated using the real materials for the realization of the layer *H'* using the parameters reported in Table 4.2 for *a-Si* and *SiNx*.

We may conclude that the optimal ternary QWL designs are fairly robust against uncertainties in the deposition-related thick-

36-layers $\Rightarrow [H, L]^5[B, L]^{13}$ with $\kappa_B = 10^{-5}$

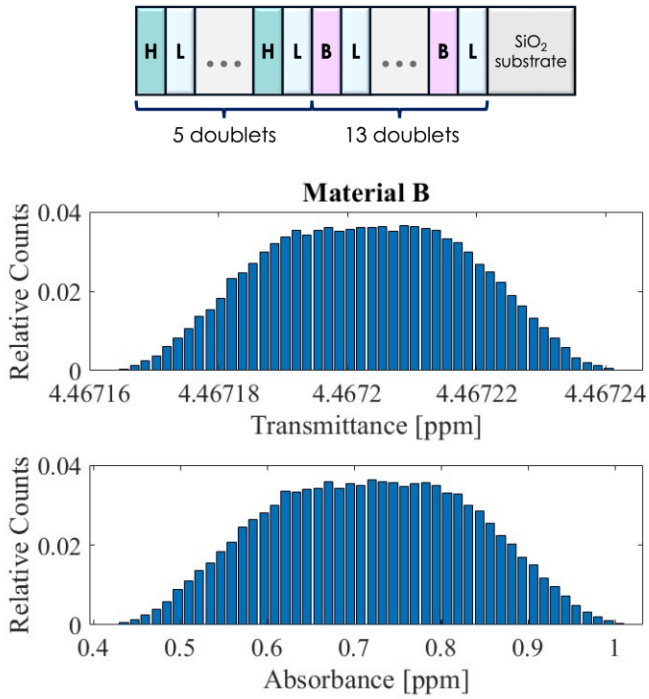

Table 4.8: Optimal ternary QWL coating using material B: distributions of coating transmittance and absorbance in a sample of 10^5 realizations, assuming κ_B to be random uniform in $(0.5 \cdot \bar{\kappa}_B, 1.5 \cdot \bar{\kappa}_B)$, with $\bar{\kappa}_B = 10^{-5}$, and independent identically distributed random variables.

ness errors: the transmittance and absorbance spectra are lower than the reference values, 6ppm and 1ppm, respectively. The coating noise also fulfills the design constraints in the useful band.

4.4 Nanolayers

The aim of the nanolayers (NLs) strategy already introduced by Ref. [(Principe 2015)- (Magnozzi, M. *et al.* 2018)- (Pan, H. *et al.* 2014)] is to act on the coating of the mirrors used in gravitational

26-layers $\Rightarrow [H, L]^7[a - Si, L]^6$ with $\kappa_{a-Si} = 1.22 \times 10^{-5}$

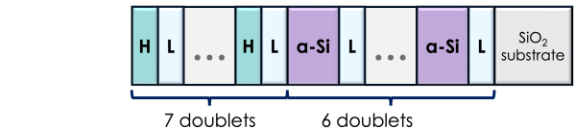

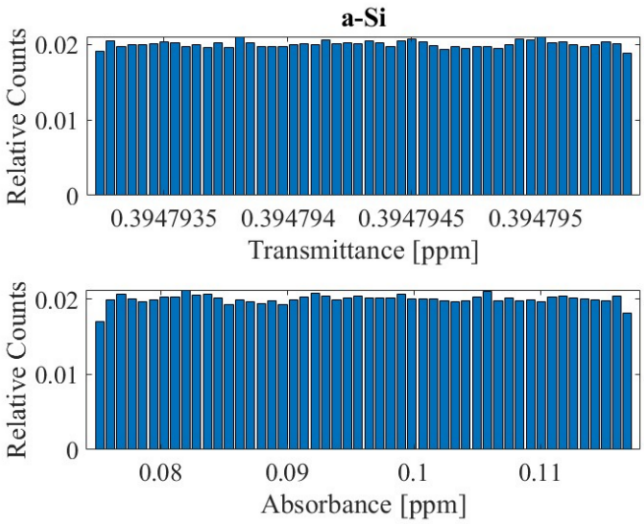

Table 4.9: Optimal ternary QWL coating using real material a-Si: distributions of coating transmittance and absorbance in a sample of 10^5 realizations, assuming κ_{a-Si} to be random uniform in $(0.5 \cdot \bar{\kappa}_{a-Si}, 1.5 \cdot \bar{\kappa}_{a-Si})$, with $\bar{\kappa}_{a-Si} = 10^{-4}$, and the same for all *a-Si* layers

wave (GW) interferometers, by replacing the layer with the highest optical losses (TiO_2-doped Ta_2O_5 in current setups) with nanostructured metamaterials, made of alternating nm-thick layers of, again, low and high refractive index. A schematic drawing of the NL structures studied is shown in Figure 4.9. This strategy makes it possible to synthesize an artificial material with an excellent equivalent refractive index as to greatly improve the optical properties of GW mirrors as well as to be extremely useful in increasing the crystallization temperature of the overall coating, thus allowing for higher temperature annealing. In this way it is possible to

36-layers $\Rightarrow [H, L]^5[SiNx, L]^{13}$ with $\kappa_{SiNx} = 1.51 \times 10^{-5}$

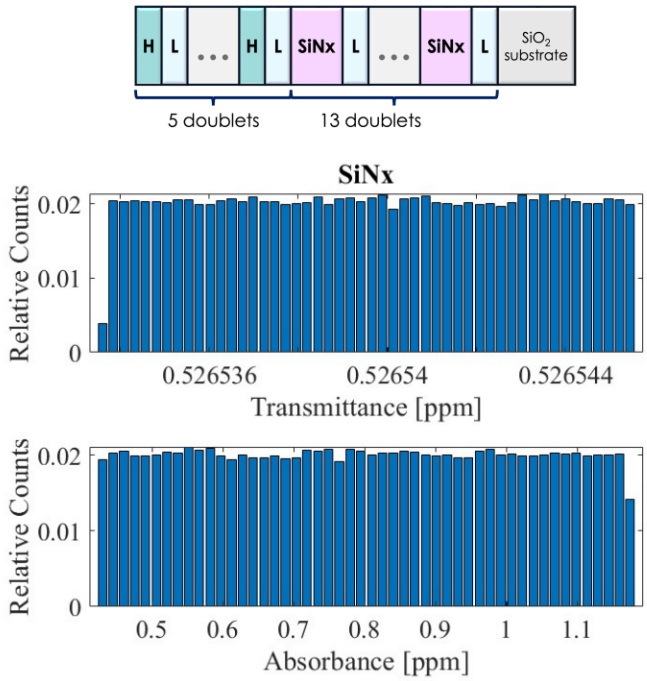

Table 4.10: Optimal ternary QWL coating using real material SiNx: distributions of coating transmittance and absorbance in a sample of 10^5 realizations, assuming κ_{SiN} to be random uniform in $(0.5 \cdot \bar{\kappa}_{SiNx}, 1.5 \cdot \bar{\kappa}_{SiNx})$, with $\bar{\kappa}_{SiNx} = 10^{-5}$, and the same for all $SiNx$ layers

produce uniform and homogeneous coatings with smooth surfaces accessible throughout accurate protocols of deposition and post-deposition thermal processes at temperature higher than 500°C. This latter is indeed the current annealing temperature used for the standard thermal process employed in the GW coating technology. The project requirements led to the study of the physics occurring when TiO_2 (high refractive index, but low crystallization temperature material) is combined with other oxides, such as SiO_2, ZrO_2, Al_2O_3, and Ta_2O_5, in a nanolayered structure. This PhD work shows a novel experimental validation of the homoge-

26-layers $\Rightarrow [H, L]^7[a - Si, L]^6$ with $\kappa_{a-Si} = 1.22 \times 10^{-5}$

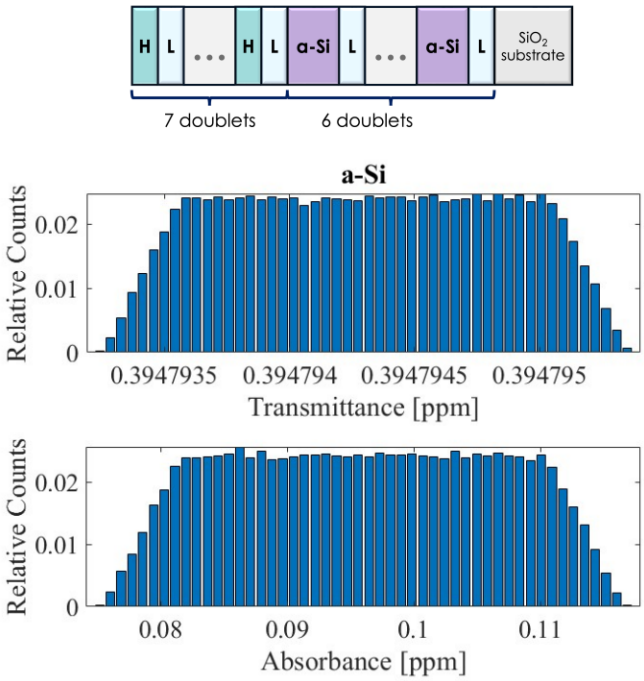

Table 4.11: Optimal ternary QWL coating using real material a-Si: distributions of coating transmittance and absorbance in a sample of 10^5 realizations, assuming κ_{a-Si} to be random uniform in $(0.5 \cdot \bar{\kappa}_{a-Si}, 1.5 \cdot \bar{\kappa}_{a-Si})$, with $\bar{\kappa}_{a-Si} = 10^{-4}$, and independent identically distributed random variables.

nization procedure based on a consolidated technique: the Abelès method. The novelty of this method, presented in the Chapter 5.2, is the possibility of carrying out the angular characterization of the optical characteristics of the media through a simpler and cheaper analysis with laboratory measuring equipment. In this sense, it is very relevant to first study the optical characteristics for the single material (TiO_2 in this thesis) and for the substrate as a function of thickness and then the application of the extension of the Abeles method. After that this study is extended for the TiO_2/SiO_2 multilayered structure and consequently the cou-

36-layers $\Rightarrow [H, L]^5[SiNx, L]^{13}$ with $\kappa_{SiNx} = 1.51 \times 10^{-5}$

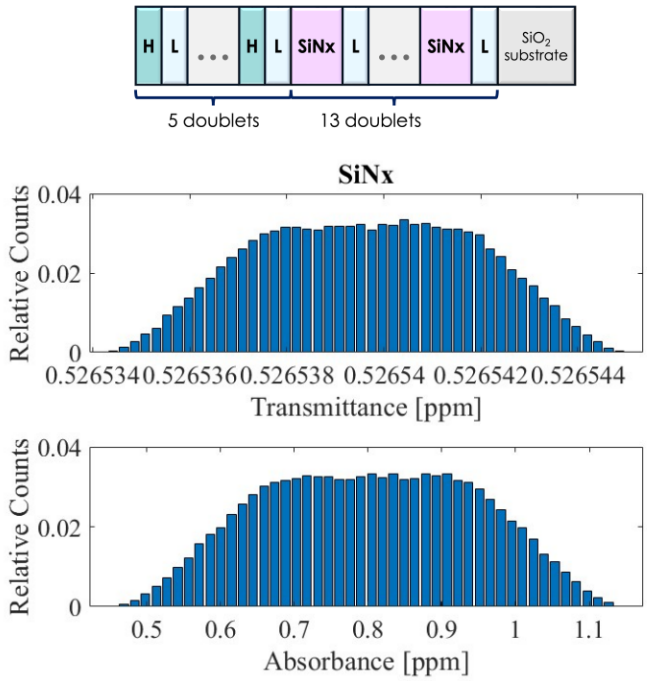

Table 4.12: Optimal ternary QWL coating using real material SiNx: distributions of coating transmittance and absorbance in a sample of 10^5 realizations, assuming κ_{SiN} to be random uniform in $(0.5 \cdot \bar{\kappa}_{SiNx}, 1.5 \cdot \bar{\kappa}_{SiNx})$, with $\bar{\kappa}_{SiNx} = 10^{-5}$, and independent identically distributed random variables.

pling with other oxides in a nanolayered structure, focusing on the combination of TiO_2 with SiO_2, Ta_2O_5, ZrO_2, and Al_2O_3.

Most of the samples investigated in this work, Figure 4.10, are fabricated by using the OptoTech OAC- 75F coater, Figure 4.11, located at University of Sannio (Benevento), see Appendix A.

26-layers $\Rightarrow [H, L]^7[A, L]^6$ with $\kappa_A = 10^{-4}$

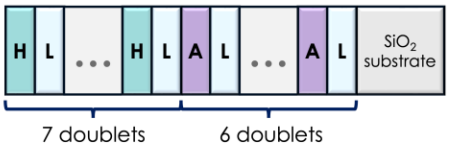

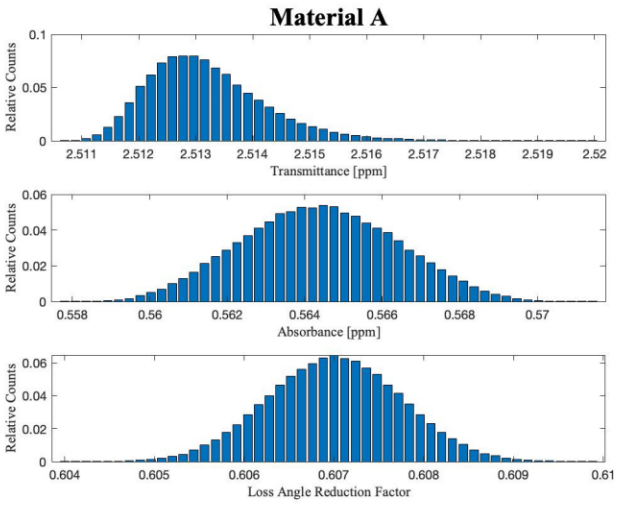

Table 4.13: Optimal ternary QWL coating using material A for *H'*: Distributions of coating transmittance, absorbance, and loss angle in a sample of 10^5 realizations (normalized to the value of the reference binary coating), assuming that the thicknesses of all layers are independent random variables that are identically distributed uniformly around the nominal QWL thickness, in a symmetric interval with a total width of 2 nm.

36-layers $\Rightarrow [H, L]^5[B, L]^{13}$ with $\kappa_B = 10^{-5}$

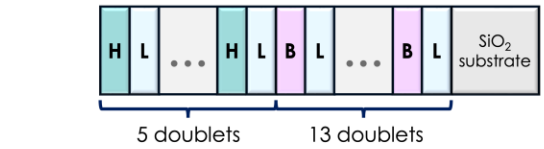

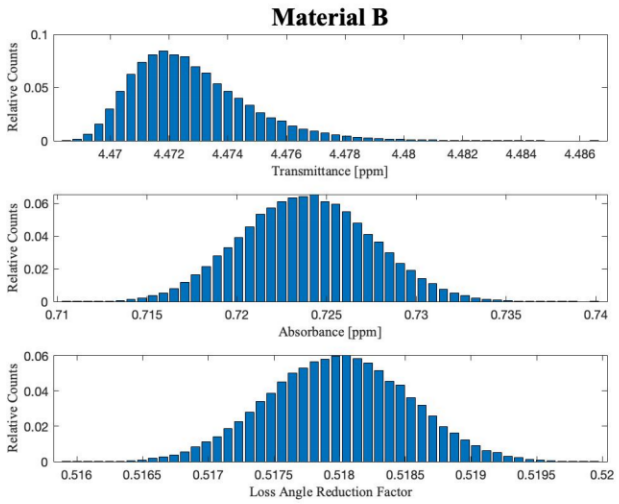

Table 4.14: Optimal ternary QWL coating using material B for *H'*: distributions of coating transmittance, absorbance, and loss angle in a sample of 10^5 realizations (normalized to the value of the reference binary coating), assuming that the thicknesses of all layers are independent random variables that are identically distributed uniformly around the nominal QWL thickness, in a symmetric interval with a total width of 2 nm.

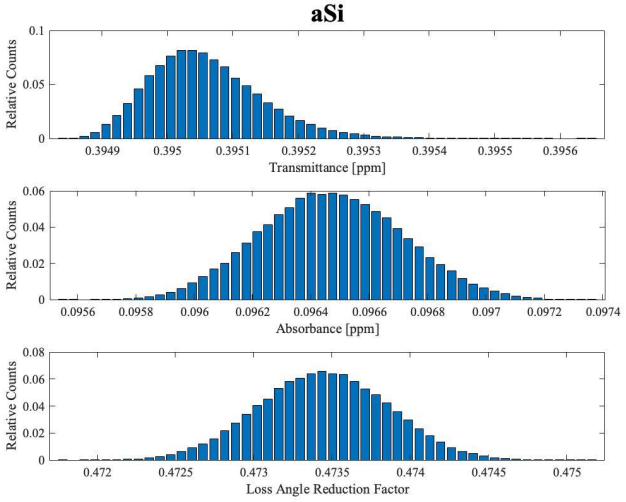

(a) $T = 20K$

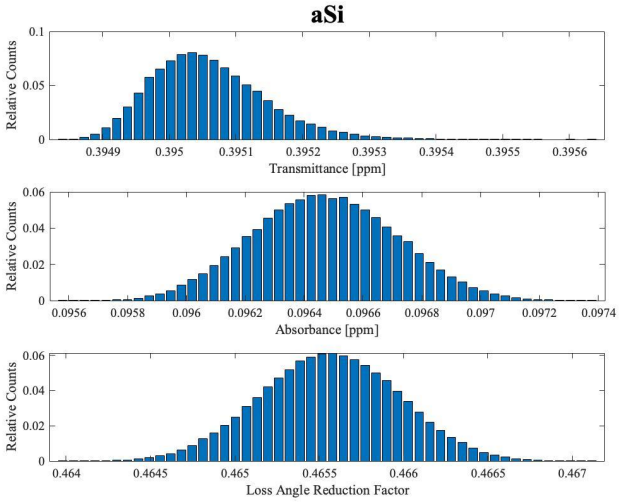

(b) $T = 120K$

Figure 4.7: Optimal ternary QWL coating using real material *a-Si* for *H'*: distributions of coating transmittance, absorbance, and loss angle in a sample of 10^5 realizations (normalized to the value of the reference binary coating), assuming that the thicknesses of all layers are independent random variables that are identically distributed uniformly around the nominal QWL thickness, in a symmetric interval with a total width of 2 nm. (a) T=20K; (b) T=120K; (c) T=290K

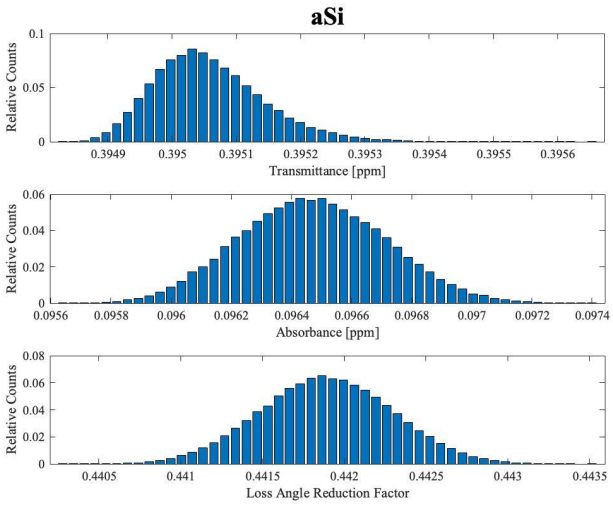

(c) $T = 290K$

Figure 4.7: Optimal ternary QWL coating using real material *a-Si* for *H'*: distributions of coating transmittance, absorbance, and loss angle in a sample of 10^5 realizations (normalized to the value of the reference binary coating), assuming that the thicknesses of all layers are independent random variables that are identically distributed uniformly around the nominal QWL thickness, in a symmetric interval with a total width of 2 nm. (a) T=20K; (b) T=120K; (c) T=290K

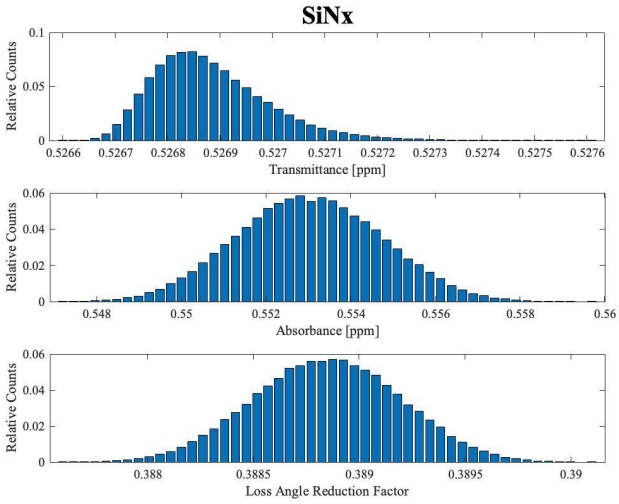

(a) $T = 20K$

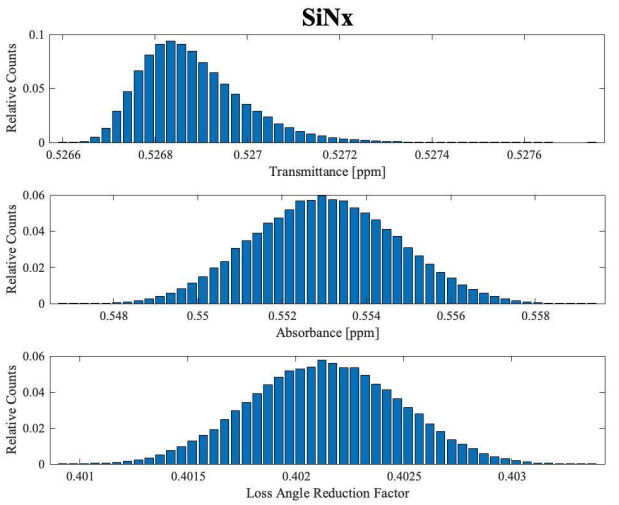

(b) $T = 120K$

Figure 4.8: Optimal ternary QWL coating using real material $SiNx$ for H': distributions of coating transmittance, absorbance, and loss angle in a sample of 10^5 realizations (normalized to the value of the reference binary coating), assuming that the thicknesses of all layers are independent random variables that are identically distributed uniformly around the nominal QWL thickness, in a symmetric interval with a total width of 2 nm. (a) T=20K; (b) T=120K; (c) T=290K

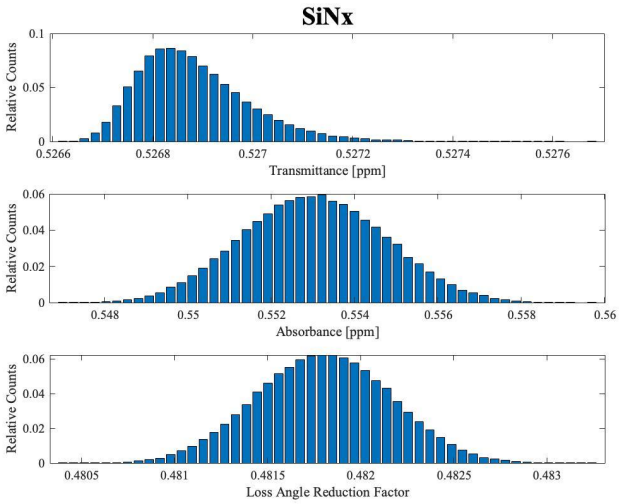

(c) $T = 290K$

Figure 4.8: Optimal ternary QWL coating using real material $SiNx$ for H': distributions of coating transmittance, absorbance, and loss angle in a sample of 10^5 realizations (normalized to the value of the reference binary coating), assuming that the thicknesses of all layers are independent random variables that are identically distributed uniformly around the nominal QWL thickness, in a symmetric interval with a total width of 2 nm. (a) T=20K; (b) T=120K; (c) T=290K

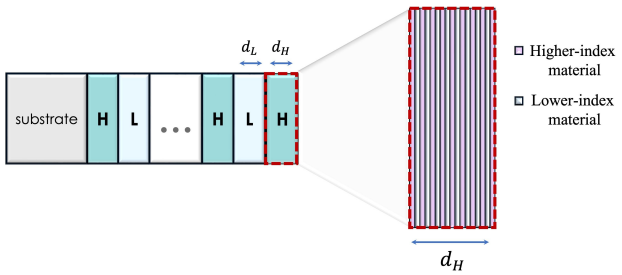

Figure 4.9: Scheme of the NL structure

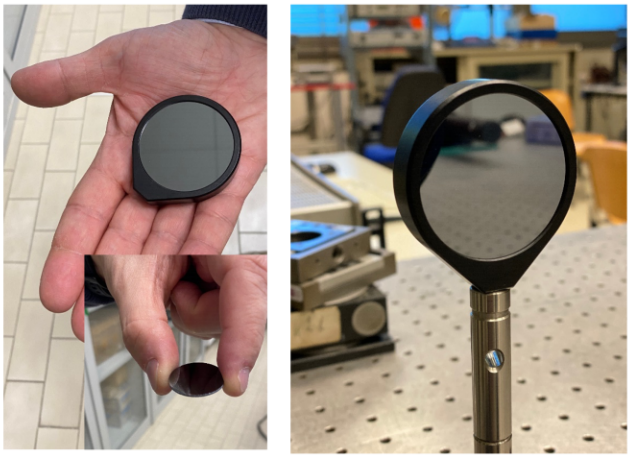

Figure 4.10: Mirror samples realized with the University of Sannio coater

(a) (b)

Figure 4.11: OptoTech OAC-75F coater located at University of Benevento.

Chapter 5

Thin Film Optical Properties

Recently, the necessity of measuring the optical characteristics of thin films has grown to the point that specialized instruments are now readily available. It is crucial to emphasize that we never, ever directly measure the optical constants n and k. While thickness, d, is easier to measure directly, the value of the optical constants is usually the result of an indirect process as well. Measurements of thin-film behavior are required for the extraction of these properties, among others, and are followed by a fitting procedure in which the parameters of a film model are changed to make the computed behavior of the model match the measured data. Then, the customizable model parameters are assumed to represent the equivalent model parameters for the real film. The process is based on a model that closely resembles the original film. It is possible to anticipate that an imperfect model with properly adjusted parameters would recreate the original measurements. But in that role, the retrieved parameters are seldom ever used. Instead, they are employed to make predictions about how films will behave in various contexts, including those in which the film may be a component of a considerably more complicated structure and/or have quite a range in thickness. This brings up the notion of stability of optical constant, which is somewhat unrelated to precision. When observed data is accurately fitted using the wrong model, the measurements may be reproduced with incredible accuracy,

but predictions for different film thicknesses may result in grave errors. Such parameters are unstable to a large extent. Stable optical constants might only be able to accurately replicate the observed values, but they would work just as well as predictors. A instance where a film that is inhomogeneous and devoid of absorption is mimicked by a homogeneous and absorbing film would be a good example. In this instance, the derived film parameters may be utterly deceptive. The film model is very significant. Accuracy of the real measurements is nearly as crucial as the model. In order to assess the performance that will be used for the optical constant extraction, calibration verification is a crucial step. Small measurement mistakes can have significant effects on the inhomogeneity of the film evaluation and/or extinction coefficient. The samples themselves ought to be appropriate for the measurement's accuracy. A poorly designed substrate, for instance, can partially deflect the beam out of the system, causing the measurement to be inaccurate, or it might create scattering losses that are uncharacteristic of the film. The calculation of performance based on an optical coating's design is a simple process. Extraction of optical constants is very different. Every film is a unique riddle. It could be required to experiment with various methods and models. Repeated coatings of various thicknesses or on several substrates could be necessary. Some films could seem to defy logical explanation. Cyclic inhomogeneity, which gives measurements that the typical simpler film models are unable to match with reasonable results, is a prevalent flaw in films. To identify potential flaws, it is always useful to try to recalculate the data using the model and extracted parameters. The computation of the optical characteristics is simple, as was seen in Chapter 1, given the optical constants and thicknesses of any succession of thin films on a substrate. There is no general analytical solution to the challenge of inverting the equations, making the inverse problem- calculating the optical constants and thicknesses of even a single thin film- much more challenging. Currently the angular characterization of the optical characteristics of the media is carried out through the ellipsometer, which is a very expensive and involved measuring instrument. We focus on a technique known as Abelés Method that allows with angular spectrum measurements to derive the optical

characteristics of a thin layer of a material whose thickness is unknown through a simpler and cheaper analysis.
At a later stage, this method will be extended to the case where a layered (multilayer) structure is deposited instead of a single material. The Abelès Method is based on the existences of the Brewster's angle whereas a multilayer structure does not exhibit total transmission phenomenon. Apparently this would lead to the conclusion that the method is not at all applicable to multilayer structure. In addition, as showed by Pendry et al. (Wood et al. 2006) the equivalent layer of a stratified nanostructure must have an anisotropic refractive index. Nevertheless, has will be shown in the following, the Abelès Method provides results that are in excellent agreement with simulated and experimental curves. Due to the simplicity of the Abelès Method is, therefore, very expedient to apply it to multilayer structures in the final goal of providing guidelines for the synthesis of nanostratified mirrors.

5.1 Ellipsometry

The optical constants of an opaque surface are totally and unambiguously defined by reflectance R and phase ϕ. Absolute reflectance is challenging to measure, and it is more common to measure how an unknown surface matches up against a recognized reference, which creates further challenges. Phase requires both an interferometric operation and a well-known standard, making it much more complicated. As a result, phase measurements are extremely uncommon and normal reflectance measurements are virtually always comparative.

There is only one reflectance value and one phase value for normal incidence, but there are two for oblique incidence, one pair for s-polarization and the other for p-polarization. Therefore, in theory, it should be feasible to utilize one as a reference for the other, which gives rise to the well-known *ellipsometry technique*. Ellipsometry uses polarized light to characterize thin film and bulk materials (Tompkins & Irene 2005). A change in polarization is measured after reflecting light from the surface, Figure 5.1: light returning from the film-substrate interface interferes with the sur-

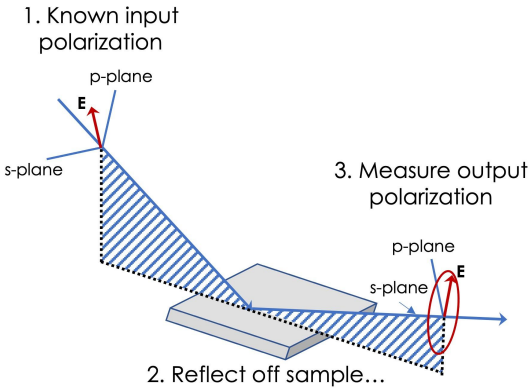

Figure 5.1: Reflection of plane polarized light from a surface resulting in elliptical polarization.

face reflection to provide layer information. Thin film thickness and optical constants (n, k) are derived from these measurement. Information is obtained from each layer interacting with the measurement.

An ellipsometry measurement, therefore, is a description of the change in light polarization after reflection from the sample under investigation. It is expressed as two parameters for each wavelength-angle combination: Psi ψ and Delta Δ

$$\Delta = \phi_p - \phi_s \quad \text{in trasmission} \tag{5.1}$$

$$\Delta = \phi_p - \phi_s \pm \pi \quad \text{in reflection} \tag{5.2}$$

These values can be related to the ratio of complex Fresnel reflection coefficients, ρ_p and ρ_s, for p- and s- polarized light, through the well known formula

$$\tan\psi = \left|\frac{\rho_p}{\rho_s}\right| \quad \text{or} \quad \left|\frac{\tau_p}{\tau_s}\right| \tag{5.3}$$

One of the various advantages of ellipsometry is that it only requires single illuminated spot for the two measurements. There are also no reference samples that need to be kept up to date, and even though high precision is needed, the measurement just requires basic polarized light manipulations. The measurement is at an oblique angle, which makes it challenging to analyze the

findings. The fact that there are just two parameters much less than the number that is sometimes required to create a thorough description of the system is a drawback. This constraint is typically overcome by adding a physical model and further altering the wavelength, angle of incidence, or both. *Variable angle spectroscopic ellipsometry*, or VASE, is as it is usually referred to the combination. A simple surface may be defined using just two variables: extinction coefficient and refractive index. It should be feasible to determine the surface parameters from a single ellipsometric measurement since there are two ellipsometric parameters: ψ and Δ. Unfortunately, this is not normally the case with a thin film on a substrate. Three parameters, n, k, and d, are required to define the film even with a straightforward absorbing film on a substrate that has previously been defined. The characteristics of absorbing coatings may only marginally differ from the surface of a bulk material. In these cases, it's frequently thought that the extraction methods employed for a straightforward surface apply. The recovered parameters, n and k, are commonly referred to as the pseudo-optical constants in this case. Even if they might not be appropriate for thin film calculations and forecasts, they often show the basic characteristics of the real optical constants.

The wavelength is varied in spectroscopic ellipsometry. Redundancy is included since the physical thickness of the film is not wavelength-sensitive. The introduction of supplementary data is then adequate. This often results in a spectral variation of the optical constant that is accorded to a known model. When additional film parameters are added, the measurement's redundancy can be so high that even straightforward multilayers can be assessed.

For example, optical characterization by spectroscopic ellipsometry of high-quality oxide coating materials used in gravitational-wave advanced detectors(aLIGO, Advanced Virgo, KAGRA) (Amato, A. *et al.* 2019) was carried out comparing the experimental data $(\Psi_{exp}, \Delta_{exp})$ with simulations $(\Psi_{mod}, \Delta_{mod})$ based on realistic optical models of the system under investigation. The complex dielectric function ε and the thickness of layers in the optical stack are parametrically taken into consideration in models. Minimization of *mean squared error* (MSE) is used to assess the validity of

the model and improve parameter values:

$$MSE = \frac{1}{2N - M} \sum_{i=1}^{N} \left[\left| \frac{\Psi_i^{mod} - \Psi_i^{exp}}{\sigma_{\Psi,i}^{exp}} \right|^2 + \left| \frac{\Delta_i^{mod} - \Delta_i^{exp}}{\sigma_{\Delta,i}^{exp}} \right|^2 \right] \tag{5.4}$$

where N is the number of experimental points, M is the number of the parameters used in the model to simulate the points and σ^{exp} is the standard deviation of experimental data.

5.2 Abelés Method

A classical technique for determining out the refractive index of dielectric thin films is the Abelès method. It was developed by Abelès (Abelès 1963) in 1949, and since then, research on it has been ongoing (Goell & Standley 1972) (Awai & Ikenoue 1984). As a result, its key characteristics are well understood. The technique is based on the principle for that p-polarized incident light, when it is incident at the Brewster angle of the film, entirely transmits through the surface of the film, as if the film is not being "seen".

As a result, the Brewster angle is the angle for which the transmittance spectrums for p-polarized incidence of the film and of the substrate alone cross.

The ray, in fact, undergoes the effects of the film medium, namely, it is bent by refraction, but it does not experience energy loss and does not bounce back and forth in the film as is typical.

Let us consider a structure consisting of two homogeneous dielectric half-spaces with refractive indices of n_0 and n_2, respectively, and a thin layer with refractive index n_1 sandwiched between them (see Figure 5.2). The substrate is the half-space to the bottom (with refractive index n_2), while the vacuum is the half-space to the top.

Let a monochromatic plane wave impinge with an incidence angle θ_0 on the coating from the vacuum, part of this wave will be transmitted inside the film and will be incident on the interface with the substrate with an angle of incidence θ_1.

Assuming that the substrate is much thicker than the penetration depth it can be assumed to be semi-infinite, so that in the

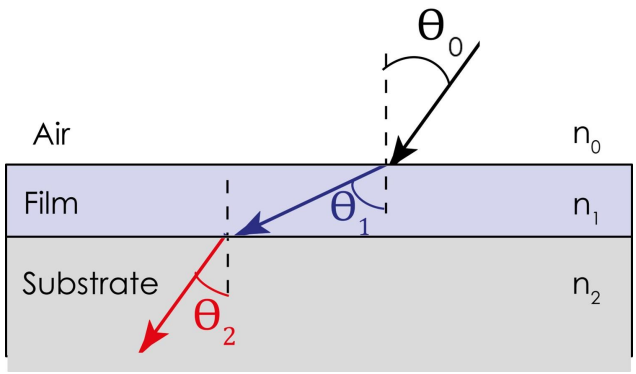

Figure 5.2: Model of Multilayers structure under test

substrate there will be only the transmitted wave that propagates endlessly with the angle θ_2.

The field reflection coefficient for this structure can be found in many textbooks (e.g., refs. (Born & Wolf 2013)), and is sometimes referred to as the Fresnel-Airy formula:

$$\Gamma = \frac{\Gamma_{01} + \Gamma_{12} e^{-2i\delta_1}}{1 - \Gamma_{01}\Gamma_{12} e^{-2i\delta_1}} \tag{5.5}$$

where

$$\Gamma_{ij}(\theta_i) = \frac{\tan(\theta_j - \theta_i)}{\tan(\theta_j + \theta_i)}$$

is the polarization-dependent Fresnel coefficient and

$$\delta_1 = \frac{2\pi}{\lambda} n_1 d_1 \cos\theta_1$$

The fraction of light that is reflected is described by the Fresnel equations and depends on the incoming light's polarization and angle of incidence. The Fresnel equations predict that light with the p-polarization (electric field vector lying in the same plane defined by the incident ray and the vector normal to the surface) will not be reflected if the angle of incidence is the *Brewster's angle*

$$\theta_B = \theta_0 = \tan^{-1}\left(\frac{n_1}{n_0}\right) \tag{5.6}$$

Therefore, the reflection coefficient at the Air-film interface at an angle of incidence equal to the Brewster's angle is

$$\Gamma_{01}(\theta_B) = 0$$

And the total reflection coefficient of our system is given by

$$\Gamma_B = \Gamma_{12B} e^{-j2\delta_{1B}} \tag{5.7}$$

We can now write the result obtained in terms of reflectance, making use of the fact that $|e^{-i2\delta_{1B}}| = 1$.

$$|\Gamma_B|^2 = |\Gamma_{12B}|^2 \tag{5.8}$$

In this case Snell's law can be written as follows:

$$n_0 \sin\theta_B = n_1 \sin\theta_{1B} \tag{5.9}$$

From which it is possible to obtain:

$$\sin\theta_{1B} = \frac{n_0}{n_1} \sin\theta_B \tag{5.10}$$

Now exploiting the result of Equation 5.6 it can be observed that:

$$\frac{n_0}{n_1} = \tan\theta_B \tag{5.11}$$

Consequently, 5.11 can be replaced within 5.10, obtaining:

$$\begin{aligned} \sin\theta_{1B} &= \frac{\sin\theta_B}{\tan\theta_B} \\ &= \frac{\sin\theta_B \cos\theta_B}{\sin\theta_B} \\ &= \cos\theta_B \end{aligned} \tag{5.12}$$

But this equation has physical significance only in the case where:

$$\theta_{1B} = \frac{\pi}{2} - \theta_B \tag{5.13}$$

That is θ_{1B} and θ_B are complementary angles.

It can be shown that, at the Brewster's angle, the Fresnel reflection coefficient for the interface between the film under test and the substrate is equal to the Fresnel reflection coefficient at the Air-Substrate interface. At the Film -Substrate interface the Fresnel reflection coefficient is

$$\Gamma_{12B}(\theta_B) = \frac{\tan(\theta_{2B} - \theta_{1B})}{\tan(\theta_{2B} + \theta_{1B})} \tag{5.14}$$

Replacing the Equation 5.13 whitin the 5.14 we have:

$$\begin{aligned}
\Gamma_{12B}(\theta_B) &= \frac{\tan\left[\theta_{2B} - \left(\frac{\pi}{2} - \theta_B\right)\right]}{\tan\left[\theta_{2B} + \left(\frac{\pi}{2} - \theta_B\right)\right]} \\
&= \frac{\tan\left[\theta_{2B} + \theta_B - \frac{\pi}{2}\right]}{\tan\left[\theta_{2B} - \theta_B + \frac{\pi}{2}\right]} \\
&= -\frac{\tan\left[\frac{\pi}{2} - (\theta_{2B} + \theta_B)\right]}{\tan\left[\frac{\pi}{2} + (\theta_{2B} - \theta_B)\right]}
\end{aligned} \tag{5.15}$$

Using the relation $tan\left(\frac{\pi}{2} \pm \alpha\right) = \pm \cot \alpha$ the previous relationship simplifies as

$$\begin{aligned}
\Gamma_{12B}(\theta_B) &= \frac{\cot(\theta_{2B} + \theta_B)}{-\cot(\theta_{2B} - \theta_B)} \\
&= \frac{\tan(\theta_{2B} - \theta_B)}{\tan(\theta_{2B} + \theta_B)}
\end{aligned} \tag{5.16}$$

That is $\Gamma_{02B}(\theta_B)$, i.e.

$$\Gamma_{02B}(\theta_B) = \frac{\tan(\theta_{2B} - \theta_B)}{\tan(\theta_{2B} + \theta_B)} \tag{5.17}$$

In terms of reflectance, it can be said that, at the Brewster angle, the reflectance of the entire system under test (Air-Film-Substrate) is equal to the reflectance of the structure composed of Air-Substrate:

$$|\Gamma_B|^2 = |\Gamma_{02B}|^2 \tag{5.18}$$

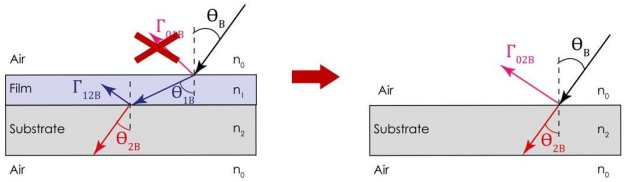

Figure 5.3: Schematic of the reflection at Brewster's angle incidence

5.2.1 Shortcomings of Abelés Method

The simplicity of this method, the fact that it works even though there isn't much information available, and the fact that the only requirements for the method to work are that the film and substrate are homogeneous and isotropic and the film height is uniform, makes it attractive and widely used despite its shortcomings. (Logofatu, P. *et al.* 2006) One major drawback is the fact that it cannot be used for absorbent films, because absorbent media have no Brewster angle at all and the incident beam cannot "not see" the film. Furthermore, even if only the substrate is absorbent, the method becomes ambiguous and often useless.

5.2.1.1 Dielectric film and substrate

It is well known that the Abelès method can be unclear since it can reveal many crossings of the two reflectance curves even when the film and substrate are both dielectric. The basic empiric rule that spurious crossings are really tangents of the film curve to the substrate curve, as can be shown in Figure 5.4, or double solutions of the following equation, is used to exclude these spurious intersections

$$R_p^{film}(\theta) = R_p^{substrate}(\theta), \tag{5.19}$$

with θ the incidence angle. With one exception – the Brewster angle – the oscillations of the film curve in this situation are tangent to those of the substrate curve. If the film curve is lower than the substrate curve for angles of incidence below the Brewster angle, the situation is reversed for values above the Brewster

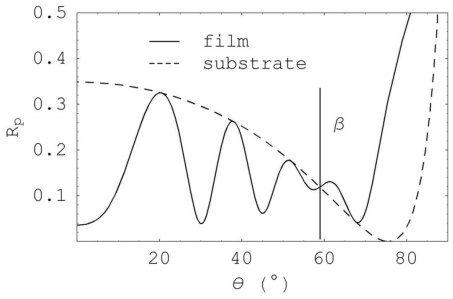

Figure 5.4: Reflectance curves corresponding to all dielectric material structure. In order to highlight the tangents, the film's height was purposefully selected to be rather large. We may see that the film curve flips above the substrate curve and maintains tangent points at incidence angles greater than the Brewster's angle. (Logofatu, P. *et al.* 2006)

angle. The intersection corresponding to the Brewster angle may be found where the trend of the curves is reversed. If the refractive index of the substrate is lower than the refractive index of the film, the behavior of the curves is reversed. The value of the film thickness is large in the preceding case to enable viewing of the tangent oscillations. They can only be observed at the intersection at the Brewster angle for thinner films, not at any other tangent locations. Although the rule of thumb for excluding spurious solutions generally applies, there are several circumstances in which it cannot be used and the procedure is unclear.

5.2.1.2 Dielectric film and absorbent substrate

When the substrate is absorbent, there is no means of excluding roots that are not Brewster's angle In this situation, the solution of Equation 5.19 is complex thus assuming a more complicated form. However, only a few practical cases fall into this evenience.

5.2.2 Homogenization in Layered Systems

It is feasible to illustrate how the optical characteristics are affected by the limited layer widths, going beyond the effective-medium approximation. Indeed, for a multilayer structure of two

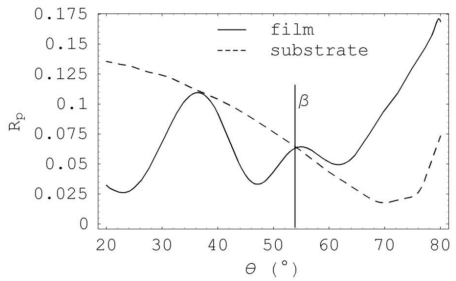

Figure 5.5: Experimental application of the Abelès method. At angles of incidence other than the Brewster angle, it is possible to observe the tangent characteristic between the film curve and the substrate curve as well as the shift in the locations of the curves, with the film curve now being higher than the substrate curve. (Logofatu, P. *et al.* 2006)

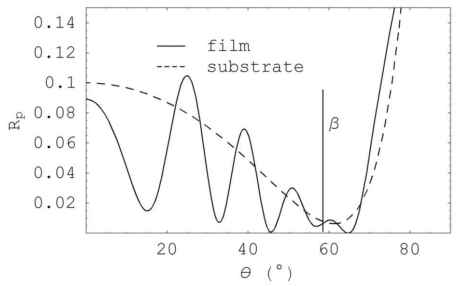

Figure 5.6: Reflectance curves corresponding to a structure with a substrate with a significant absorption coefficient. It cannot be distinguished the intersection at the Brewster angle from the spurious solutions. (Logofatu, P. *et al.* 2006)

different constituent materials n_1 and n_2 with thickness d_1 and d_2, respectively, it is expected that homogeneous and isotropic permittivity and permeability characteristics may adequately represent each layer. The entire system may be thought of as a single anisotropic media with the dielectric permittivity when the layers are thin enough:

$$\varepsilon_x = \varepsilon_y = \frac{\varepsilon_1 + \eta\varepsilon_2}{1+\eta}, \tag{5.20}$$

$$\frac{1}{\varepsilon_z} = \frac{1}{1+\eta}\left(\frac{1}{\varepsilon_1} + \frac{\eta}{\varepsilon_2}\right), \tag{5.21}$$

with

$$\eta = \frac{d_2}{d_1} \tag{5.22}$$

the fraction of widths of the two layers. Through the characteristic matrix formalism, this may be seen in a useful way. This, in fact, makes it possible to determine the effective parameters of the medium for the under study uni-dimensional system of alternating layers. TM fields are taken into consideration to determine the effective dielectric permittivity, whereas TE fields are used to determine the effective magnetic permeability. The z axis is parallel to the layers in the geometry of the system. The xz plane is assumed to be the plane of incidence; however, because of the system's symmetry, this is identical to the yz plane, and the results that follow are generic. The Fourier component of the field in the medium j in the plane $z = z_0$ and that in the plane $z = z_0 + d$ are related by the characteristic matrix $\boldsymbol{M}_j(k_x, d)$. It has the following form for TM waves in a homogeneous medium:

$$\boldsymbol{M}_j(k_x, d) = \begin{pmatrix} \cos k_z^{(j)} d & \dfrac{\imath k_0 \varepsilon_j}{k_z^{(j)}} \sin k_z^{(j)} d \\ \dfrac{\imath k_z^{(j)}}{k_0 \varepsilon_j} \sin k_z^{(j)} d & \cos k_z^{(j)} d \end{pmatrix} \tag{5.23}$$

where the dispersion relation determines $k_z^{(j)}$

$$k_x^2 + \left(k_z^{(j)}\right)^2 = \varepsilon k_0^2. \tag{5.24}$$

One layer of each material makes up a single cell in the layered system, and the matrix for that cell is just the product of the

matrices for the several layers:

$$\boldsymbol{M}_{cell}\left(k_x, d_1, \eta\right) = \boldsymbol{M}_1\left(k_x, d_1\right)\boldsymbol{M}_2\left(k_x, \eta d_1\right). \tag{5.25}$$

A system of n cells has the characteristic matrix $\boldsymbol{M}_n = \left(\boldsymbol{M}_{cell}\right)^n$. This may be determined by diagonalizing $\boldsymbol{M}_{cell}$ and finding

$$\boldsymbol{M}_n = \frac{1}{p-q}\begin{pmatrix} -q\lambda^n + p\lambda^{-n} & \lambda^n - \lambda^{-n} \\ -pq\left(\lambda^n - \lambda^{-n}\right) & p\lambda^n - q\lambda^{-n} \end{pmatrix}. \tag{5.26}$$

Since $det\boldsymbol{M}_{cell} = 1$, the eigenvalues are λ and λ^{-1}. p and q are the ratios of the components of the eigenvectors of $\boldsymbol{M}_{cell}$. The characteristic matrix for an effective medium expanding in powers the layer thickness may be related to $\boldsymbol{M}_n$:

$$\begin{aligned} \boldsymbol{M}_n = & \begin{pmatrix} \cos k_z^{eff} n(1+\eta)d_1 & \dfrac{\imath k_0 \boldsymbol{\varepsilon}_x}{k_z^{eff}} \sin k_z^{eff} n(1+\eta)d_1 \\ \dfrac{\imath k_z^{eff}}{k_0 \boldsymbol{\varepsilon}_x} \sin k_z^{eff} n(1+\eta)d_1 & \cos k_z^{eff} n(1+\eta)d_1 \end{pmatrix} \\ & + O[(1+\eta)d_1] \qquad (5.27) \\ = & \boldsymbol{M}_{eff} + O[(1+\eta)d_1] \qquad (5.28) \end{aligned}$$

where the parameters of the effective medium are 5.20 and 5.21, which appear in the effective medium's dispersion law but are different from 5.24 since the permittivity is now anisotropic:

$$\frac{k_x^2}{\boldsymbol{\varepsilon}_z} + \frac{\left(k_z^{eff}\right)^2}{\boldsymbol{\varepsilon}_x} = k_0^2. \tag{5.29}$$

5.3 Validation of Abelès Method

To validate the applicability of the Abelès Method to nanostratified structure – as already pointed out in the introduction paragraph – some simulations have been performed to calculate the equivalent refractive index of multilayer structures checking if the theoretical results are consistent.

As an example, let's simulate a three multilayer structures made of 60 layer of alternate high- low-index material with $n_H =$

2.1 and $n_L = 1.7$ in the first case, $n_H = 3$ and $n_L = 1.5$ in the second, and $n_H = 2.4$ and $n_L = 1.7$ in the last case, and with an infinite substrate of $n_s = 3$. The thickness of each layer is chosen to be $d_H = 2nm$ and $d_L = 3nm$. The input medium is considered air $n_{in} = 1$. Table 5.1 summarizes the refractive index of the coating material employed in the simulations and report the equivalent refractive index obtained with the Abelès Method, n_eq, and the indexes n_x and n_z for an equivalent anisotropic medium derived from the eq. 5.20 and eq. 5.21.

60 layers – $\mathbf{d_H} = 2nm$ $\mathbf{d_L} = 3nm$ –					
Case	$\mathbf{n_H}$	$\mathbf{n_L}$	$\mathbf{n_{eq}}$	$\mathbf{n_x}$	$\mathbf{n_z}$
1	2.1	1.7	1.87283	1.87029	1.83089
2	3.0	1.5	2.24604	2.22486	1.79284
3	2.4	1.7	2.01449	2.00948	1.89983

Table 5.1: Refractive index of coating materials employed in simulations with thickness of each layer $d_H = 2nm$ and $d_L = 3nm$ and an infinite substrate of $n_s = 3$.

For the first case, in Figure 5.7a is reported the simulated reflectance curves of the multilayer (blue curve) and of the air-substrate interface alone (red curve). Following the Abelès Method it has been found the intersection between those curves which occurs at an angle which replaced in the equation 5.6 the equivalent refractive index is $n_{eq} = 1.87283$. In the Figure 5.7b are depicted the reflectance of the multilayer calculated with the Transmission Matrix Method, blue curve, and the reflectance of the equivalent layer with refractive index $n_{eq} = 1.87283$ and thickness equal to the total thickness of the multilayer, i.e. $d_{eq} = 150nm$, red curve. As it can be seen the two curves are in excellent agreement – with Mean Square Error (MSE) as low as 3.49×10^{-5} and the percentage error for normal incidence between the two reflectances $\Delta_r(0)\% = 0.336$, thus validating the practical use of the Abelès Method. The Table 5.2 summarizes the results just described.

In the second case, in Figure 5.8a is reported the simulated reflectance curves of the multilayer (blue curve) and of the air-substrate interface alone (red curve). To follow the Abelès Method

60 layers $\mathbf{d_H} = 2nm$ $\mathbf{d_L} = 3nm$		
$\mathbf{n_H} = 2.1$ $\mathbf{n_L} = 1.7$		
	MSE%	$\mathbf{\Delta_r(0)\%}$
$\mathbf{n_{eq}} = 1.87283$	3.49×10^{-5}	0.336

Table 5.2: Percentage Mean Square Error ($MSE\%$) and percentage error for normal incidence $\Delta_r(0)\%$ between the reflectance of the multilayer calculated with the Transmission Matrix Method and the reflectance of the equivalent layer with refractive index n_{eq} for the first case in Table 5.1

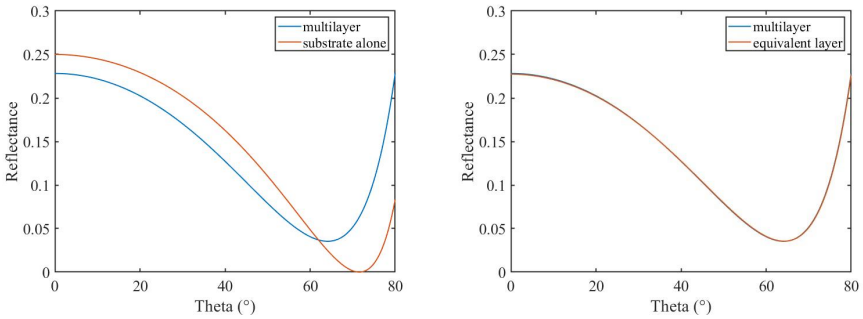

(a) (b)

Figure 5.7: Reflectance of simulated structures: (a) Blue curve: multilayer made of 60 layer with $n_H = 2.1$, $d_H = 2nm$, $n_L = 1.7$, $d_L = 3nm$ with an infinite substrate of $n_s = 3$; red curve: air-substrate interface. (b): Blue curve: multilayer made of 60 layer with $n_H = 2.1$, $d_H = 2nm$, $n_L = 1.7$, $d_L = 3nm$ with an infinite substrate of $n_s = 3$; red curve: equivalent layer with $n_{eq} = 1.87283$, $d_{eq} = 150nm$ with an infinite substrate of $n_s = 3$.

it has been found the intersection between those curves and the equivalent refractive index $n_{eq} = 2.24604$. In the Figure 5.8b are depicted the reflectance of the multilayer calculated with the Transmission Matrix Method, blue curve, and the reflectance of the equivalent layer with refractive index $n_{eq} = 2.24604$ and thickness equal to the total thickness of the multilayer, i.e. $d_{eq} =$

$150nm$, red curve. Also in this case it can be seen that the two curves are in excellent agreement – with Mean Square Error (MSE) as low as 6.42×10^{-4} and the percentage error for normal incidence between the two reflectances $\Delta_r(0)\% = 0.274$. The Table 5.3 summarizes the results just described.

60 layers $\mathbf{d_H} = 2nm$ $\mathbf{d_L} = 3nm$		
$\mathbf{n_H} = 3.0$ $\mathbf{n_L} = 1.5$		
	MSE%	$\mathbf{\Delta_r(0)\%}$
$\mathbf{n_{eq}} = 2.24604$	6.42×10^{-4}	0.274

Table 5.3: Percentage Mean Square Error ($MSE\%$) and percentage error for normal incidence $\Delta_r(0)\%$ between the reflectance of the multilayer calculated with the Transmission Matrix Method and the reflectance of the equivalent layer with refractive index n_{eq} for the second case in Table 5.1

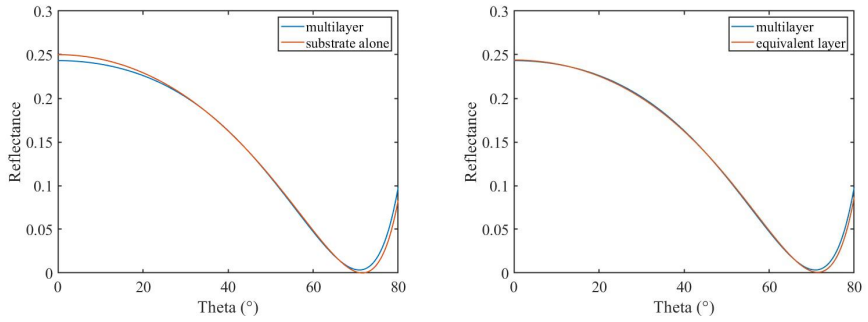

(a) (b)

Figure 5.8: Reflectance of simulated structures: (a) Blue curve: multilayer made of 60 layer with $n_H = 3.0$, $d_H = 2nm$, $n_L = 1.5$, $d_L = 3nm$ with an infinite substrate of $n_s = 3$; red curve: air-substrate interface. (b): Blue curve: multilayer made of 60 layer with $n_H = 3.0$, $d_H = 2nm$, $n_L = 1.5$, $d_L = 3nm$ with an infinite substrate of $n_s = 3$; red curve: equivalent layer with $n_{eq} = 2.24604$, $d_{eq} = 150nm$ with an infinite substrate of $n_s = 3$.

In the last case, in Figure 5.9a is reported the simulated reflectance curves of the multilayer (blue curve) and of the air-substrate interface alone (red curve). To follow the Abelès Method it has been found the intersection between those curves and the equivalent refractive index $n_{eq} = 2.01449$. In the Figure 5.9b are depicted the reflectance of the multilayer calculated with the Transmission Matrix Method, blue curve, and the reflectance of the equivalent layer with refractive index $n_{eq} = 2.01449$ and thickness equal to the total thickness of the multilayer, i.e. $d_{eq} = 150nm$, red curve. Also in this case it can be seen that the two curves are in excellent agreement – with Mean Square Error (MSE) as low as 2.22×10^{-4} and the percentage error for normal incidence between the two reflectances $\Delta_r(0)\% = 0.227$.

The Table 5.4 summarizes the results just described.

60 layers $\mathbf{d_H} = 2nm$ $\mathbf{d_L} = 3nm$		
$\mathbf{n_H} = 2.4$ $\mathbf{n_L} = 1.7$		
	MSE%	$\mathbf{\Delta_r(0)}\%$
$\mathbf{n_{eq}} = 2.01449$	2.22×10^{-4}	0.227

Table 5.4: Percentage Mean Square Error ($MSE\%$) and percentage error for normal incidence $\Delta_r(0)\%$ between the reflectance of the multilayer calculated with the Transmission Matrix Method and the reflectance of the equivalent layer with refractive index n_{eq} for the third case in Table 5.1

Many other simulations have been performed with various refractive indexes and layer thicknesses always obtaining great accordance between the reflectance of the multilayer and of the equivalent layer.

For our purposes this results is very useful for drafting guidelines to synthesize high-reflectance mirrors under normal incidence condition.

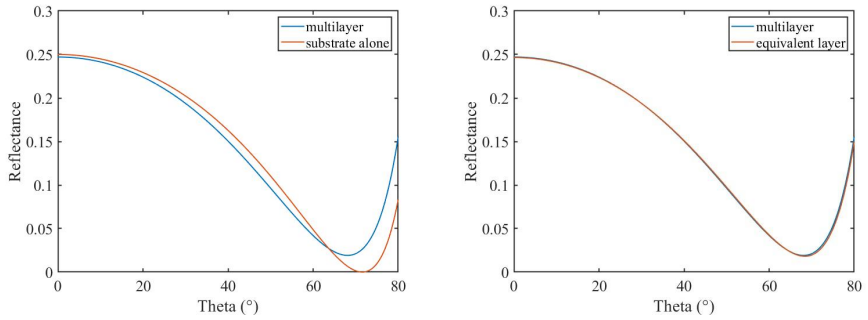

(a) (b)

Figure 5.9: Reflectance of simulated structures: (a) Blue curve: multilayer made of 60 layer with $n_H = 2.4$, $d_H = 2nm$, $n_L = 1.7$, $d_L = 3nm$ with an infinite substrate of $n_s = 3$; red curve: air-substrate interface. (b): Blue curve: multilayer made of 60 layer with $n_H = 2.4$, $d_H = 2nm$, $n_L = 1.7$, $d_L = 3nm$ with an infinite substrate of $n_s = 3$; red curve: equivalent layer with $n_{eq} = 2.01449$, $d_{eq} = 150nm$ with an infinite substrate of $n_s = 3$.

Chapter 6

Results and Discussion

6.1 Experimental Application of the Abelés Method

In order to experimentally validate the Abelès Method an optical setup to measure angular reflectance spectra of real samples – deposited at University of Sannio in Benevento – has been built and is located in the Microwave and Optical Technologies Laboratory (MOTLab) in Industrial Engigneering Department at University of Salerno and is shown in Figure 6.1.

A laser source, at a wavelength of $632.8nm$, passes through a polarizer (which only transmits the p-polarized waves to identify the Brewster angle) and a $100\mu m$ pin-hole with the purpose of conveying the incident wave and having a collimated ray. The emerging wave is incident on the sample placed on a rotator with a graduated ring that allows you to measure the reflected power transmitted through a photometer as the angle varies.

Therefore, it was possible to obtain the refractive index of the film under consideration by measuring the reflectance of the substrate (Air-Substrate interface alone) first, and measuring the reflectance of the system composed of Air-Film-Substrate afterwards. Then, with a Matlab routine, the two curves of the reflectance were reconstructed as the angle of incidence changed; they were superimposed and the intersection between the two curves was found, which occurs precisely in correspondence of the

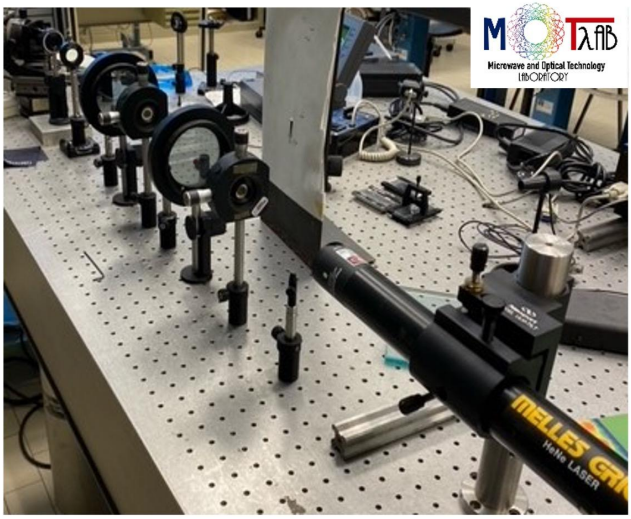

Figure 6.1: Measurement setup for angular characterization in the Microwave and Optical Technologies Laboratory (MOTLab) in Industrial Engigneering Department at University of Salerno

Brewster angle.

Finally, by exploiting the inverse equation of the definition of the Brewster angle, it was possible to know the refractive index of the film under test provided that the substrate refractive index is known with a certain accuracy.

6.2 Calibration of the measurement setup

In order to calibrate the measurement setup described in the previous section, it has been tested the efficiency of the setup by measuring the angular reflectance spectrum on a known film made of a layer of TiO_2 200 nm thick deposited on a silicon substrate 2 mm thick, as illustrated in Figure 6.2. After retrieving the refractive index of the TiO_2 layer by means of the Abelès Method it has been compared against a reference value (*Refractiveindex.info website* n.d.).

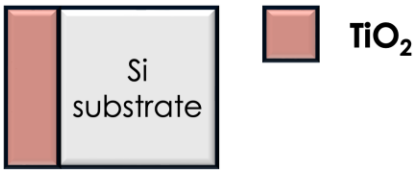

Figure 6.2: Schematic of TiO_2 layer on Si substrate.

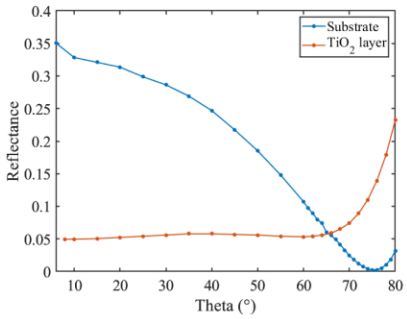

Figure 6.3: Measured reflectance of: TiO_2 layer on Si substrate (red curve) and substrate alone (blue curve).

6.2.1 Characterization of TiO_2 layer

The angular reflectance of the silicon substrate alone were measured along with the reflectance of TiO_2 layer deposited on the same silicon substrate (see Figure 6.3). Following the Abelès Method it has been found an intersection of the two curves at angle $\theta = 65.66°$, making an interpolation of the measurement data. Using the equation (5.6) the refractive index of the thin film titania layer has been found to be $n_{film} = 2.21 \pm 0.07$, which is consistent with the reference value (*Refractiveindex.info website* n.d.). The uncertainty in the value of n_{film} is due to the accuracy of the measurement setup which is $\pm 1°$.

The angular reflectance calculated with the n_{film} value has been superimposed to the measured one finding an excellent agreement, as depicted in Figure 6.4.

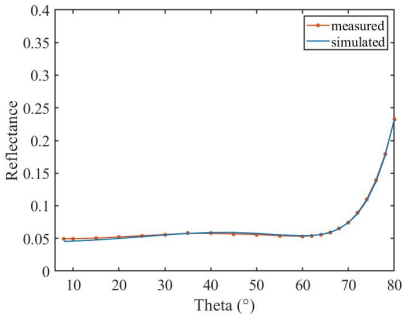

Figure 6.4: Comparison between the measured reflectance of TiO_2 layer on Si substrate (red curve) and the reflectance of the equivalent layer (blue curve).

6.3 Nanolayers: Extension of Abelés Method

As has already been discussed, both the high and low refractive index material present issues that need to be solved. In particular, the high refractive index one, especially in its as-grown form, is affected by high mechanical and optical losses as a consequence of an insufficient material densification. To reduce these losses, and thus improving the optical/mechanical performances, the new strategy of nanolayering for "creating" ad-hoc a material with both high refractive index and high crystallization temperature has been introduced. The nanolayered structures have been deposited on Si substrate by using IAD at the University of Sannio, and optically characterized at MOTLab. Applying the Abelès Method it has been obtained the refractive index of the equivalent layer following the homogenization procedure.

The reflectance of the equivalent layer is then calculated using the matrix method, par. 2.6, and then compared to the measured one.

The method will be applied to:

1. TiO_2/SiO_2 in NLs with two different degree of segmentation (76 and 82);

2. TiO_2 with various low refractive index oxides (Ta_2O_5, Al_2O_3,

or ZrO_2) in NLs each having its own segmentation degree.

6.3.1 Characterization of TiO_2/SiO_2 Nanolayers

TiO_2/SiO_2 NLs deposited on Si substrate by using IAD have been optically characterized by means of Abelés Method. The number of layers, the nominal thickness, d_{nom}, (i.e thickness set during the deposition phase) of the single layer and the total nominal thickness of the coating are shown in Table 6.1. The results of

N* Layer	**Thickness**		
	SiO_2	TiO_2	Coating
76-layers	13 $\mathring{A}$	20 $\mathring{A}$	125.4 nm
82-layers	10 $\mathring{A}$	20 $\mathring{A}$	123 nm

Table 6.1: Parameters of TiO_2/SiO_2 nanolayers: number of layers, nominal thickness, d_{nom}, (i.e thickness set during the deposition phase) of the single layer and total nominal thickness

these characterizations are summarized in the following Table 6.2 where θ_B is the Brewster's angle, n_{eq} the equivalent refractive in-

Layer	$\theta_\mathbf{B}$	$\mathbf{n_{eq}}$	$\mathbf{d_{fit}}$	**MSE**%
76-layers	64.7	2.1155	116.15 nm	4.20×10^{-3}
82-layers	64.8	2.1251	112.60 nm	1.49×10^{-3}

Table 6.2: Parameters of equivalent layer of TiO_2/SiO_2 nanolayers: Brewster's angle θ_B, equivalent refractive index, n_{eq}, depth of the Abelés equivalent layer d_{fit} and Percentage Mean Square Error, $MSE\%$, between the measured reflectivity and the simulated one with equivalent layer parameters.

dex, d_{fit} is the thickness of the equivalent layer falling under the range of uncertainty which best reproduce the measured reflectivity, $MSE\%$ is the Percentage Mean Square Error between the

measured reflectivity and the simulated one with equivalent layer parameters.

Figure 6.5: Schematic of TiO_2/SiO_2 nanolayer structure.

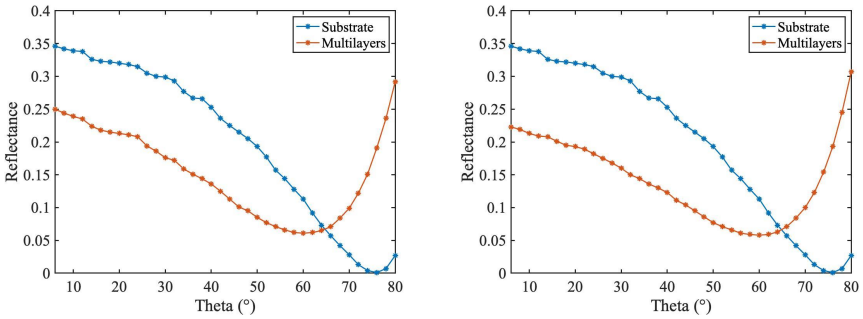

(a) (b)

Figure 6.6: Measured reflectance of: TiO_2/SiO_2 nanolayers (red curve) and substrate alone (blue curve). (a) 76 layers; (b) 82 layers.

Figure 6.5 shows the schematic of the structure under test, Figure 6.6a and Figure 6.6b the Angular reflectance spectrum and the application of Abelès Method of the 76-nanolayers and 82-nanolayers, respectively. Figure6.7a and Figure6.7b show the measured spectrum reflectivity and the one simulated by a Matlab routine of the nanolayer structure made of equivalent layer with n_{eq} and d_{fit} reported in Table 6.2.

It is important to point out that the control of thickness is crucial to reach the desired optical properties of the prototype. In fact, it is possible to see that small variations of thickness may cause remarkable differences in the refractive index of the nanolayer.

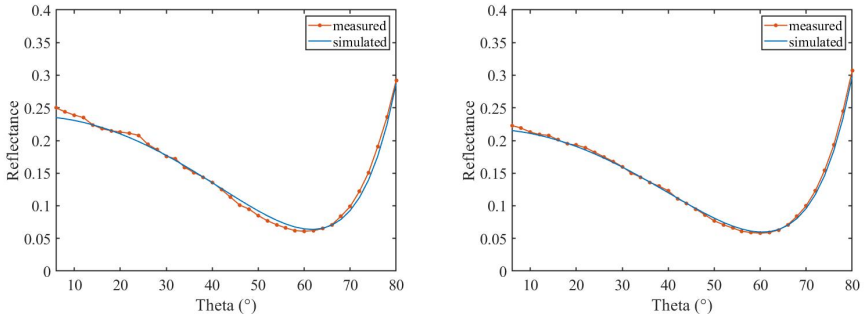

(a) (b)

Figure 6.7: Comparison between the measured reflectance of TiO_2/SiO_2 nanolayers (red curve) and the reflectance of the equivalent layer (blue curve). (a) 76 layers; (b) 82 layers.

6.3.2 Characterization of TiO_2-based Nanolayers

NLs formed by alternating TiO_2 with Ta_2O_5, Al_2O_3, and ZrO_2 are analyzed by adopting the same strategy as illustrated in the previous section. The oxides are characterized by a higher refractive index compared to SiO_2at wavelength of $1064nm$, wich is the operation wavelength of the laser actually used in GWs interferometer. Indeed, the refractive index are:

- $n_{TiO_2} = 2.3894$
- $n_{Ta_2O_5} = 2.1200$
- $n_{Al_2O_3} = 1.6773$
- $n_{ZrO_2} = 2.1517$
- $n_{SiO_2} = 1.4636$

The nominal thickness of low- and high-index material layers constituting the analyzed NLs are reported in the Table 6.3 along with the total thickness of the NL coating.

Measurements of the reflectance spectrum have been conducted on such NLs finding, for each of them, the value at which the

No. Layer	Thickness		
	L-index	H-index	Coating
62-layers	ZrO_2	TiO_2	
	17 Å	20 Å	114.7 nm
68-layers	Ta_2O_5	TiO_2	
	14 Å	20 Å	115.6 nm
78-layers	Al_2O_3	TiO_2	
	11 Å	20 Å	120.9 nm

Table 6.3: Parameters of TiO_2-based nanolayers: number of layers, nominal thickness, d_{nom}, (i.e thickness set during the deposition phase) of the single layer and total nominal thickness

reflectivity spectrum matches the one of the substrate alone, see Figures 6.9.

The values of the angles at which it occurs are reported in the third column of the Table 6.4. The calculated equivalent refractive index is reported therein.

L-index	**H-index**	θ_B	$\mathbf{n_{eq}}$	$\mathbf{d_{fit}}$	**MSE**%
ZrO_2	TiO_2	66.3	2.2781	102.15 nm	1.13×10^{-2}
Ta_2O_5	TiO_2	66.6	2.3109	105.40 nm	2.52×10^{-2}
Al_2O_3	TiO_2	64.3	2.0778	115.55 nm	6.40×10^{-2}

Table 6.4: Parameters of equivalent layer of TiO_2-based nanolayers: Brewster's angle θ_B, equivalent refractive index, n_{eq}, depth of the Abelés equivalent layer d_{fit} and Percentage Mean Square Error, $MSE\%$, between the measured reflectivity and the simulated one with equivalent layer parameters.

Once the refractive index of the equivalent layer has been calculated the reflectance spectrum is then compared with the measured one using a thickness d_{fit} which provides the curve the minimum MSE%. The value of d_{fit} – which always falls into the uncertainty

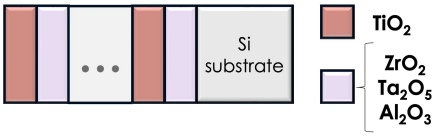

Figure 6.8: Schematic of TiO_2-based nanolayers.

range of the thickness of the NLs deposited – and the MSE% are reported in the Table 6.4.

As it can be seen from Figures 6.10 there is an excellent agreement between the simulated curves using the parameters obtained by the Abelès Method and the measured ones.

6.4 Additional Future Work

To better simulate the actual mirrors of the gravitational waves detector the prototypes realized at University of Sannio will be simulated using COMSOL Multiphysics® software taking into account surfaces deformation due to the thermal stress induced by the high power of the incident laser. An example of the actual mirrors is shown in Figure6.11.

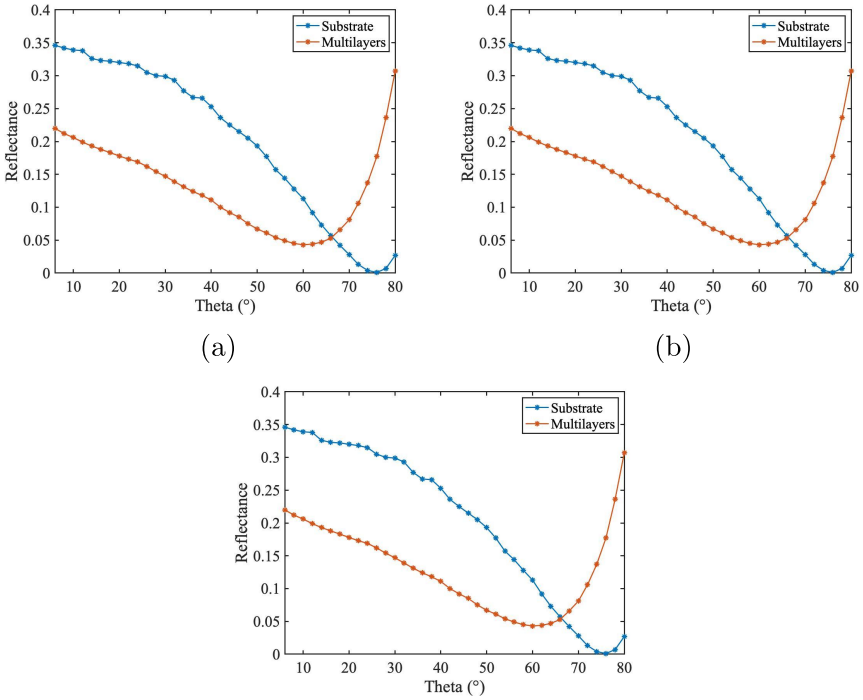

Figure 6.9: Measured reflectance of the nanolayers (red curve) and substrate alone (blue curve). (a) TiO_2/ZrO_2 NLs; (b) TiO_2/Ta_2O_5 NLs and (c) TiO_2/Al_2O_3 NLs.

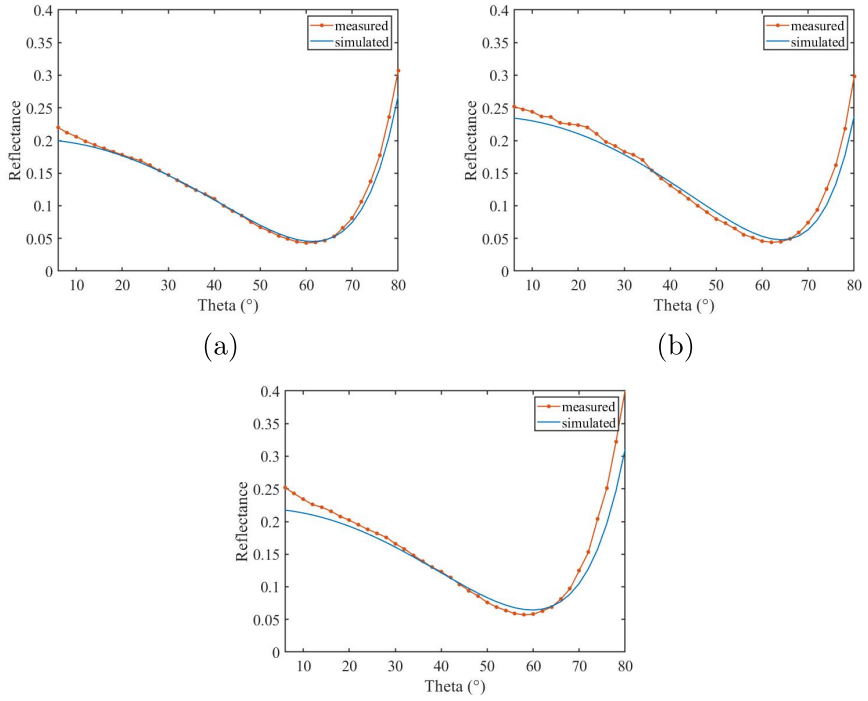

Figure 6.10: Comparison between the measured reflectance of the nanolayers (red curve) and the reflectance of the equivalent layer (blue curve). (a) TiO_2/ZrO_2 NLs; (a) TiO_2/ZrO_2 NLs; (b) TiO_2/Ta_2O_5NLs and (c) TiO_2/Al_2O_3 NLs.

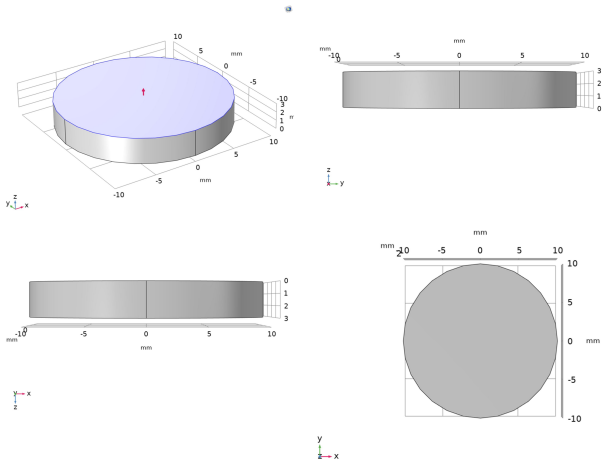

Figure 6.11: Default view, YZ, XZ and YX of the structure in the graphics section of COMSOL Multiphysics

Chapter 7

Quadrature Differential Phase Interferometer

The work done during this PhD thesis took place for the coating characterization of the gravitational wave interferometers' optics. Now, some approaches are being explored in order to build a very sensitive detection scheme of the mechanical loss angle and thermal noise, in addition extending the frequency spectrum analyzed. This combination of high precision and large input range of wavelength can be obtained using differential interferometry (Schönenberger & Alvarado 1989). For this purpose, a measurement bench with a QDPI, *Quadrature Differential Phase Interferometer*, is under construction. By combining measurements made on a microcantilever before and after the deposition of a thin film, it is possible to characterize the internal mechanical dissipation of this coating. This instrument is intented to eventually contribute to the optimisation of optical coatings of future gravitational wave detectors, aiming at minimizing the limitations due to thermal noise.

The QPDI is a kind of homodyne laser interferometer optimized for the measurement of a microcantilever deflection with very high resolution (down to $\sim 1fm/\sqrt{Hz}$) and low environmental susceptibility (Paolino et al. 2013). This setup is based on differential interferometry, Figure 7.1: two beams are produced using the double refraction of a birefringent element and are reflected by the base and the free end of the microcantilever. An

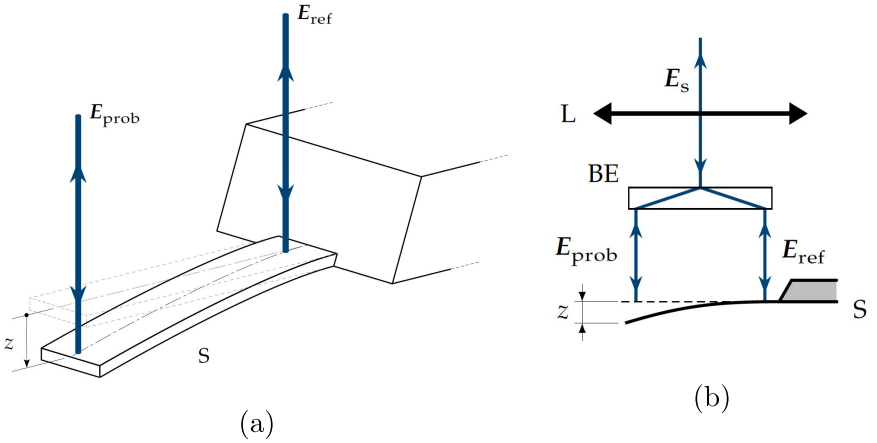

Figure 7.1: Differential interferometry principle. (a): two parallel laser beams are focused on the microcantilever sample S, Eref and Eprob, that are equivalents to the two arms of a conventional Michelson interferometer. Eref is the reference one, it is reflected by the static base, and Eprob is the sensing one by the free end of the cantilever. A deflection z of the cantilever increases the optical path difference, and so the interferences between the two beams, by $\delta L = 2z$. (b): The input laser beam Es is focused by a lens L and divided in the two beams by a birefringent element BE. The BE allows for a spatial separation of only a few hundred microns between the beams, compatible with the length of typical microcantilevers. After separation, the two converging beams thus produce two spots which are made much smaller than the cantilever width.

analysis of the interferences between the two beams leads to a direct, differential sensing of the cantilever deflection. This analysis is performed using a quadrature phase detection technique. This technique allows for a complete determination of the optical phase: after a calibration procedure, the optical phase can be precisely related to the cantilever deflection, while not being affected by the laser intensity fluctuation, and with a constant sensibility.

In this chapter the Jones calculus is briefly introduced, which will then be used to describe the transformation occurring to the laser beam on its path inside an ideal Quadrature Phase Differen-

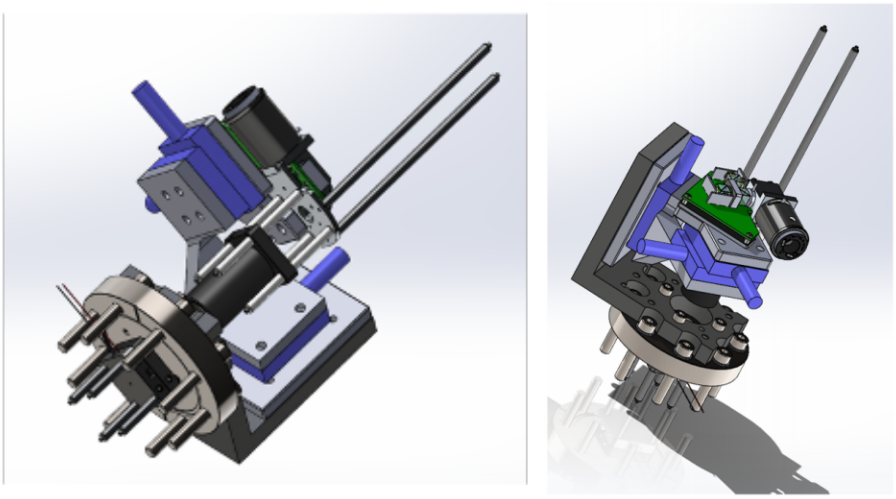

(a) (b)

Figure 7.2: QDPI Quadrature Phase Differential Interferometer project.

tial Interferometer. Also the mathematical relation between the deformation of the cantilever and the signals measured by the QPDI's four photodetectors is established in the ideal case. The processing of these signals is then described, along with a correction method accounting for the imperfections of a real interferometer. Figure 7.2 shows the SolidWorks design of the interfrerometer core developed in collaboration with the University of Lyon and the INFN National Institute of Nuclear Physics. While the Figure 7.3 shows the work done so far and the realization of which is the main goal of the next project in the collaboration.

7.1 Operating principle

7.1.1 Jones calculus

The Jones calculus (Gerrard & Burch 1994) is a matrix formalism which allows a compact mathematical treatment of polarized light and its transformations by means of polarizing optical components. It is suitable for describing a polarization interferometer

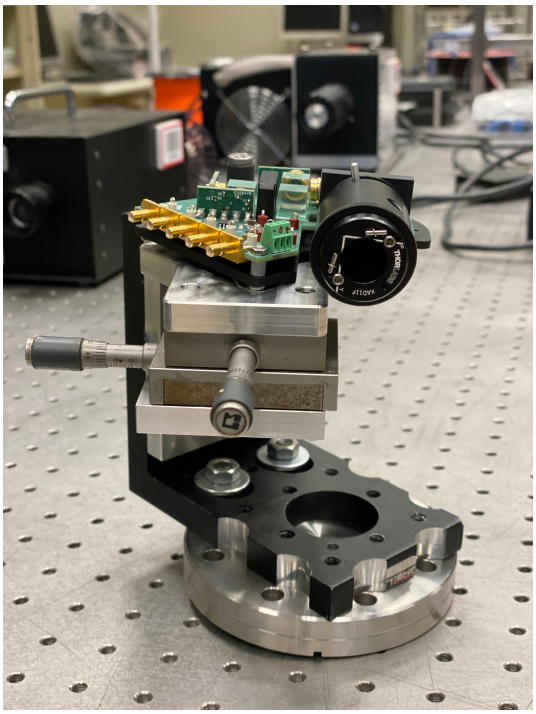

(a)

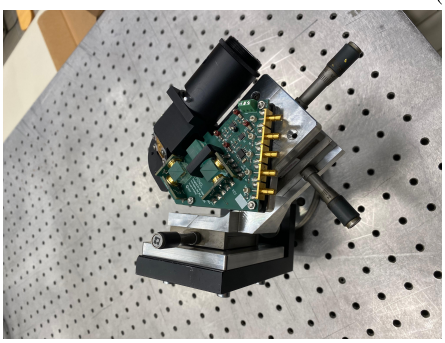

(b)

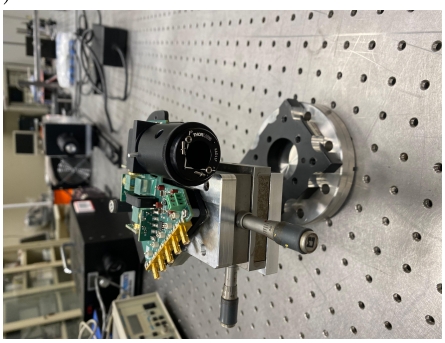

(c)

Figure 7.3: QDPI Quadrature Phase Differential Interferometer.

using a single-mode laser source, such as the QPDI. This formalism, in fact, is used for problems involving both polarization and interference phenomena, where the superposition of the luminous electric field must be considered. The light under examination must be monochromatic, coherent and completely polarized. As we have already seen in the Chapter 2, a light beam propagating along the z-axis is represented by the electric field component $\boldsymbol{E}$ of a uniform plane electromagnetic wave, given by

$$\boldsymbol{E} = \boldsymbol{E_x x} + \boldsymbol{E_y y} \tag{7.1}$$

with

$$\boldsymbol{E_x} = E_{0x}\cos(\omega t - kz + \delta_x) \tag{7.2}$$
$$\boldsymbol{E_y} = E_{0y}\cos(\omega t - kz + \delta_y) \tag{7.3}$$

where $\boldsymbol{E_x}$ and $\boldsymbol{E_y}$ are the field components along the x and y-axes. The electric field $\boldsymbol{E}$ can be seen as the real part of a complex wave:

$$\boldsymbol{E} = \mathrm{Re}(\boldsymbol{E_0} e^{\imath(\omega t - kz)}) \tag{7.4}$$

where $\boldsymbol{E_0}$ is the Jones vector that is given by

$$\boldsymbol{E_0} = \begin{pmatrix} E_x \\ E_y \end{pmatrix} = \begin{pmatrix} E_{0x} e^{\imath\delta_x} \\ E_{0y} e^{\imath\delta_y} \end{pmatrix} \equiv \begin{pmatrix} E_{0x} \\ E_{0y} e^{\imath(\delta_y - \delta_x)} \end{pmatrix} \tag{7.5}$$

Up to a multiplicative factor, the beam intensity I, so the irradiance, of the beam $\boldsymbol{E}$ is given by:

$$I = (\boldsymbol{E}^T \cdot \boldsymbol{E}) = (E_x E_x^* + E_y E_y^*) \tag{7.6}$$

where $\cdot, ()^*\mathrm{and}()^T$ indicate scalar product, complex conjugation and complex transposition respectively. The Jones vector contains all the information about the state of polarization of the associated light beam and it is also sufficient for intensity calculations. The change of polarization occuring to a beam passing through a linear optical element is represented by

$$\boldsymbol{E_1} = \boldsymbol{J}\boldsymbol{E_0} \tag{7.7}$$

where $\boldsymbol{E_0}$ is the state of the input beam, $\boldsymbol{E_1}$ the state of the output beam, and where $\boldsymbol{J}$ is the 2×2 Jones matrix of the optical element considered:

$$\boldsymbol{J} = \begin{pmatrix} J_{xx} & J_{xy} \\ J_{yx} & J_{yy} \end{pmatrix} \tag{7.8}$$

where the matrix elements J_{ij} are generally complex, and depend only of the optical component considered. The Jones matrix of a given component depends on its angular orientation with respect to the beam propagation axis, and therefore the coordinate system used to identify this orientation "follows" a light beam along its optical path.

The optical scheme of the QPDI is shown in the scheme of Figure 7.4, and the symbols used are described in Table 7.1.

Symbol	Description
$\boldsymbol{E_{in}}$	input beam
$\boldsymbol{E_s}$	beam entering the sensing area
$\boldsymbol{E_a}$	beam entering the analysis area
$\boldsymbol{E_{ref}}$, $\boldsymbol{E_{prob}}$	sensing beams (Michelson arms)
L	lens (objective)
BS_s, BS_a	50:50 non-polarizing beam splitter
PBS_x, PBS_y	polarizing beam splitter
P_{lin}	linear polarizer
$\lambda/2$	half wave plate
$\lambda/4$	quarter wave plate
BE	birefringent element
S	microcantilever sample
$PD_{1\rightarrow4}$	photodetectors
$I_{1\rightarrow4}$	quadrature signals

Table 7.1: Description of symbols used in the optical scheme of QDPI, Figure 7.4

The diagram is divided into three areas: input area, sensing area and analysis area. The state of polarization of the laser beam entering the interferometer is suitably tuned in the input area and then directed towards the sensing area where the deflection of the

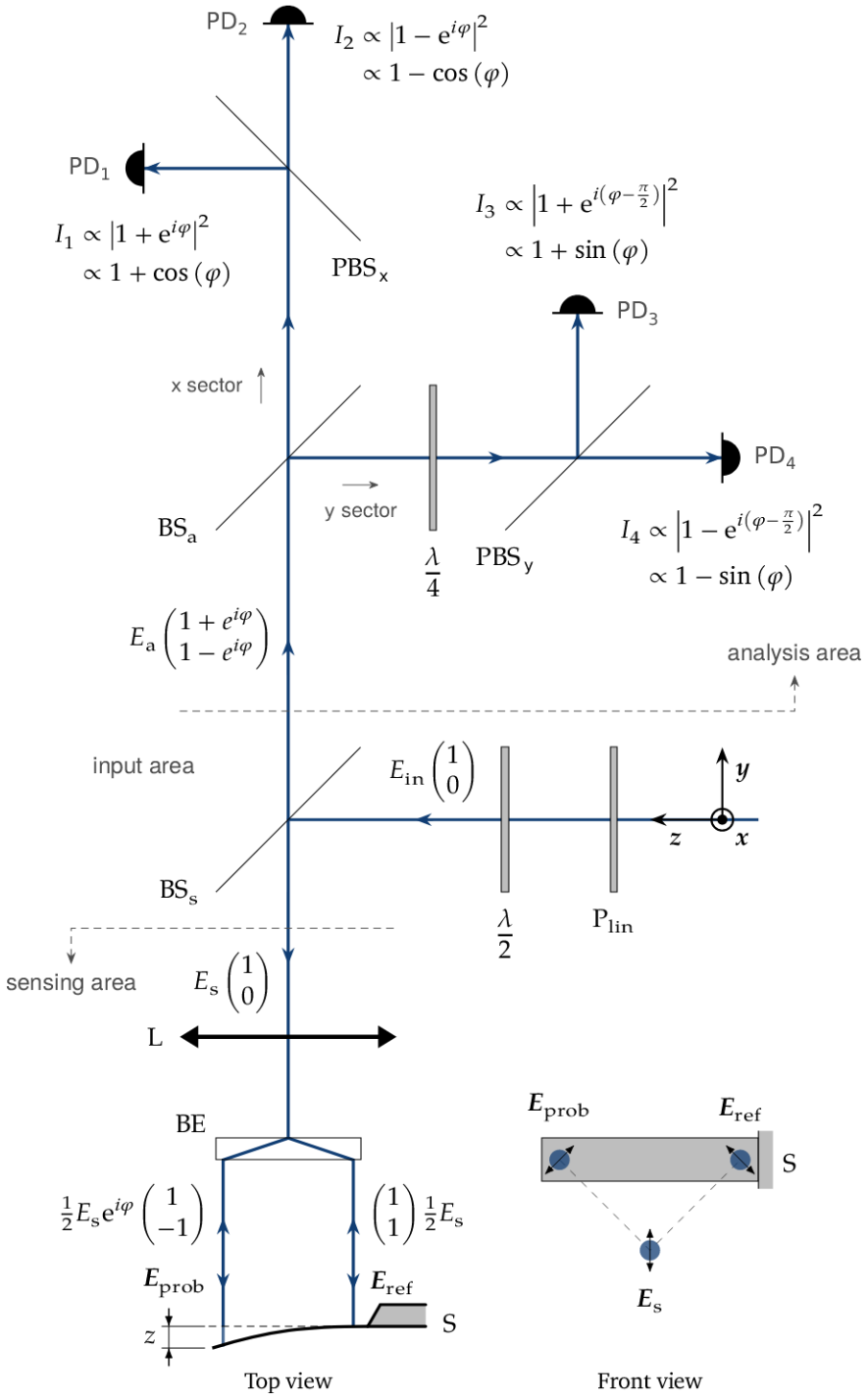

Figure 7.4: General diagram of an ideal Quadrature Phase Differential Interferometer (QPDI).

cantilever is detected. The beam then propagates into the analysis area where the interferometer signals are recorded. The Jones coordinate system for the laser beam entering the interferometer (to the right of the input area) is shown. The z axis is always oriented along the direction of propagation of the beam, while the x axis is always vertically out of the page, so only the y and z axes are reoriented with changes in the beam path. The relevant Jones matrices for the analyzes to be done are listed in Table 7.2.

	Optical component	**Jones matrix**
$\boldsymbol{P_x}$	vertical linear polarizer	$\begin{pmatrix} 1 & 0 \\ 0 & 0 \end{pmatrix}$
$\boldsymbol{P_y}$	horizontal linear polarizer	$\begin{pmatrix} 0 & 0 \\ 0 & 1 \end{pmatrix}$
$\boldsymbol{P_{x+y}}$	linear polarizer at 45°	$\frac{1}{2}\begin{pmatrix} 1 & 1 \\ 1 & 1 \end{pmatrix}$
$\boldsymbol{P_{x-y}}$	linear polarizer at -45°	$\frac{1}{2}\begin{pmatrix} 1 & -1 \\ -1 & 1 \end{pmatrix}$
$\boldsymbol{W^q_{x+y}}$	quarter wave plate, fast axis at 45°	$\frac{1}{2}\begin{pmatrix} 1-\imath & 1+\imath \\ 1+\imath & 1-\imath \end{pmatrix}$
$\boldsymbol{M}$	mirror	$\begin{pmatrix} 1 & 0 \\ 0 & -1 \end{pmatrix}$

Table 7.2: Jones matrices of the ideal optical components of interest for the QPDI.

7.1.2 QDPI optical scheme: input area

The collimated laser beam entering the interferometer is linearly polarized along the x direction by a polarizer $\mathrm{P_{lin}}$, a half wave plate $\frac{\lambda}{2}$, producing the input beam $\boldsymbol{E_{in}}$. The beam is then partly reflected toward the interferometer sensing area by a nonpolarizing beam splitter $\mathrm{BS_s}$, resulting in the beam $\boldsymbol{E_s}$. The input beam is given by:

$$\boldsymbol{E_{in}} = E_{in}\begin{pmatrix} 1 \\ 0 \end{pmatrix} \tag{7.9}$$

and the beam entering the sensing area is given by

$$\boldsymbol{E_s} = E_s \begin{pmatrix} 1 \\ 0 \end{pmatrix} \tag{7.10}$$

$E_s$andE_{in} are related by

$$E_s = rE_{in} \tag{7.11}$$

where r is the reflection coefficient of BS_s ($0 < r < 1$).

7.1.3 QDPI optical scheme: sensing area

The beam $\boldsymbol{E_S}$, focused by a lens L, is split by a birefringent element BE in two parallel beams with orthogonal polarizations $\boldsymbol{E_{ref}}$and$\boldsymbol{E_{prob}}$. The two beams are reflected by the base and the free end of the microcantilever S. The reflected component of $\boldsymbol{E_{prob}}$ acquire an additional optical path difference δL proportional to the cantilever deflection z. The two reflected beams are merged back together by BE, and the merged beam is collimated by L and partly transmitted by BS_s before to reach the QPDI analysis area. The birefringent element BE is modeled as a polarizing beam splitter whose axes are oriented along $x+y$ and $x-y$, so that the polarization state in each arm just after BE is rappresentated in the bottom right corner of figure 2.2 (front view), and is given by:

$$\begin{aligned} \boldsymbol{E^i_{ref}} &= \boldsymbol{P_{x-y}E_s} = \frac{1}{2}E_s \begin{pmatrix} 1 \\ -1 \end{pmatrix} \\ \boldsymbol{E^i_{prob}} &= \boldsymbol{P_{x+y}E_s} = \frac{1}{2}E_s \begin{pmatrix} 1 \\ 1 \end{pmatrix} \end{aligned} \tag{7.12}$$

The optical path difference δL is twice the deflection z of the cantilever:

$$\delta L = 2z \tag{7.13}$$

The corresponding phase shift φ between the two beams is

$$\varphi = \frac{4\pi}{\lambda} z \tag{7.14}$$

The beams reflected by the microcantilever is:

$$\begin{aligned} \boldsymbol{E}^{\boldsymbol{r}}_{\boldsymbol{ref}} &= \boldsymbol{M} \times \boldsymbol{E}^{\boldsymbol{i}}_{\boldsymbol{ref}} = \frac{1}{2} E_s \begin{pmatrix} 1 \\ 1 \end{pmatrix} \\ \boldsymbol{E}^{\boldsymbol{r}}_{\boldsymbol{prob}} &= \boldsymbol{M} \times \boldsymbol{E}^{\boldsymbol{i}}_{\boldsymbol{prob}} e^{\imath\varphi} = \frac{1}{2} E_s e^{\imath\varphi} \begin{pmatrix} 1 \\ -1 \end{pmatrix} \end{aligned} \tag{7.15}$$

The polarization state of the recombined beam is obtained by superimposing the fields of the two arms:

$$\boldsymbol{E}^{\boldsymbol{r}}_{\boldsymbol{ref}} + \boldsymbol{E}^{\boldsymbol{r}}_{\boldsymbol{prob}} = E_s \begin{pmatrix} 1 + e^{\imath\varphi} \\ 1 - e^{\imath\varphi} \end{pmatrix} \tag{7.16}$$

$E_a$andE_s are related by

$$E_a = tE_s \tag{7.17}$$

where t is the transmission coefficient of $\mathrm{BS_s}$ $(0 < t < 1)$. E_a results from the superposition of two beams having orthogonal polarizations, therefore no interference can be recorded directly from it. The intensity I_a shows no dependance on φ of E_a being found by:

$$I_a = 2E_a^2 \tag{7.18}$$

The phase shift caused by the cantilever deflection is encoded in the state of polarization of E_a, which is generally elliptical. To record interference, the beam E_a must be projected by at least a linear polarizer.

7.1.4 QDPI optical scheme: analysis area

The analysis area implements the quadrature phase detection technique [13]. This technique makes four quadrature intensity signals available simultaneously, that is four intensity signals with an incremental phase shift of $\frac{\pi}{2}$. The beam in this area is split evenly in two sectors x and y by a nonpolarizing beam splitter $\mathrm{BS_a}$. In each sector, the two polarization components of the beam are set to interfere after being projected by the polarizing beams splitters $\mathrm{PBS_x}$ and $\mathrm{PBS_y}$, whose axes are oriented along the $\boldsymbol{x}$ and $\boldsymbol{y}$ directions. In the $\boldsymbol{y}$ sector, a quarter wave plate $\frac{\lambda}{4}$ oriented along $(\boldsymbol{x} + \boldsymbol{y})$ add an additional delay of $\frac{\pi}{2}$ between the polarization

components, that is formally equivalent to adding a delay of $\frac{\pi}{2}$ to $\boldsymbol{E_{ref}}$, or a delay of $-\frac{\pi}{2}$ (phase lead) to $\boldsymbol{E_{prob}}$. Eventually, the four quadrature signals $I_1,\ I_2,\ I_3$ and I_4 are recorded using four photodiodes based photodetectors PD_1 to PD_4. The non-polarizing beam splitter BS_a contributes a factor of $\frac{1}{\sqrt{2}}$ to both the reflected and transmitted beams, corresponding to half the intensity of the $\boldsymbol{E_a}$ beam. The two fields produced in the x sector are then:

$$\begin{aligned} \boldsymbol{E_1} &= \frac{1}{\sqrt{2}}\boldsymbol{P_x} \times \boldsymbol{E_a} = \frac{1}{\sqrt{2}}E_a \begin{pmatrix} 1+e^{\imath\varphi} \\ 0 \end{pmatrix} \\ \boldsymbol{E_2} &= \frac{1}{\sqrt{2}}\boldsymbol{P_y} \times \boldsymbol{E_a} = \frac{1}{\sqrt{2}}E_a \begin{pmatrix} 0 \\ 1-e^{\imath\varphi} \end{pmatrix} \end{aligned} \tag{7.19}$$

and the two fields generated in the y sector are:

$$\begin{aligned} \boldsymbol{E_3} &= \frac{1}{\sqrt{2}}\boldsymbol{P_x} \times \boldsymbol{W^q_{x+y}} \times \boldsymbol{E_a} = \frac{1}{\sqrt{2}}E_a \begin{pmatrix} 1+e^{\imath(\varphi-\frac{\pi}{2})} \\ 0 \end{pmatrix} \\ \boldsymbol{E_4} &= \frac{1}{\sqrt{2}}\boldsymbol{P_y} \times \boldsymbol{W^q_{x+y}} \times \boldsymbol{E_a} = \frac{1}{\sqrt{2}}E_a \begin{pmatrix} 0 \\ 1-e^{\imath(\varphi-\frac{\pi}{2})} \end{pmatrix} \end{aligned} \tag{7.20}$$

The expression of the QPDI's four photodetectors signals are obtained as follow:

$$\begin{aligned} I_1 &= \frac{I_a}{4}(1+\cos(\varphi)) \quad I_3 = \frac{I_a}{4}(1+\sin(\varphi)) \\ I_2 &= \frac{I_a}{4}(1-\cos(\varphi)) \quad I_4 = \frac{I_a}{4}(1-\sin(\varphi)) \end{aligned} \tag{7.21}$$

The intensities I_1 to I_4 form a set of four quadrature signals as defined before. The crossed polarizations of the two interfering beam obtained by using a birefringent beam splitter allows for a direct implementation of this technique, since crossed polarizations is a key point of the processing made in the y sector (with the quarter wave plate).

7.2 Phase and deflection extraction

7.2.1 Ideal response

To obtain the phase φ it is necessary to calculate the contrast function of each sector:

$$C_x = \frac{I_1 - I_2}{I_1 + I_2} \quad C_y = \frac{I_3 - I_4}{I_3 + I_4} \tag{7.22}$$

replacing the equation 7.21, the two constrast take the forms:

$$C_x = \cos(\varphi) \quad C_y = \sin(\varphi) \tag{7.23}$$

It is convenient to define the following complex contrast:

$$C = C_x = \cos(\varphi) + \imath C_y = \sin(\varphi) = e^{\imath\varphi} \tag{7.24}$$

This formulation shows one the advantages of the quadrature detection technique: it permits a complete determination of φ (modulo 2π). In the complex plane, a measurement of C will be located on the unit circle, with a polar angle equal to the optical phase shift φ. In the measurement of a microcantilever thermal noise, the observed phase can be separated into two parts:

$$\varphi = \varphi^W + \delta\varphi \tag{7.25}$$

Here ψ^W represents a static or slowly varying phase shift, corresponding to an intrinsic optical path difference between the two arms of the interferometer, corresponding to the interferometer workpoint. $\delta\psi$ represents small variations of the cantilever deflection around the workpoint coming from thermal agitation. It is notable to underline that the system's sensitivity to $\delta\psi$ does not depends on the value of φ^W:

$$\left|\frac{\delta C}{\delta z}\right| = \frac{4\pi}{\lambda} \tag{7.26}$$

Consequently, to maximize the sensitivity of the interferometer it is not necessary to perform any adjustment of the working point and the measurements are not affected by drifts of the working point due to environmental changes (e.g. temperature variation).

7.2.2 Real response

In an experimental realisation of the Interferometer, the quadrature signals are affected by a set of errors related for example to residual misalignements of the system and the imperfection of real optical components. These errors can be taken into account by rewriting equations 7.21 as follows:

$$\begin{aligned} I_1 &= k(A_1 + B_1\cos(\varphi)) \quad I_3 = k(A_3 + B_3\cos(\varphi+\psi)) \\ I_2 &= k(A_2 - B_2\cos(\varphi)) \quad I_4 = k(A_4 - B_4\cos(\varphi+\psi)) \end{aligned} \tag{7.27}$$

where A_i is the signal mean value on the photodetector i, B_i is the signal modulation amplitude, $B_i \leq A_i$, ψ represents a deviation from perfect quadrature between sector x and sector y, and k is a common factor modeling the laser intensity fluctuations. For the contrast functions to take the ideal values of equation 2.23, the signals should exhibit perfect local contrast ($A_i = B_i$), perfect modulation balance inside each sector ($B_1 = B_2,\ B_3 = B_4$), and no deviation from a perfect $\frac{\pi}{2}$ quadrature ($\psi = 0$), which is not achievable in practice. The errors present in the quadrature signals are thus translated to a distortion of the interferometer response, that must be corrected to avoid an erroneous evaluation of the phase. The contrast expressions of equation 2.23 for the real signals become:

$$\begin{aligned} C_x &= \frac{A_1 - A_2 + (B_1 + B_2)\cos(\varphi)}{A_1 + A_2 + (B_1 - B_2)\cos(\varphi)} \\ C_y &= \frac{A_3 - A_4 + (B_3 + B_4)\sin(\varphi+\psi)}{A_3 + A_4 + (B_3 - B_4)\sin(\varphi+\psi)} \end{aligned} \tag{7.28}$$

Notable, the laser noise factor k is factored out of the contrast expressions, meaning that the extracted phase φ is not affected by the laser intensity fluctuations. In practice also the modulation balance inside each sector holds to a good approximation. The distorded contrast functions can hence be modeled by:

$$\begin{aligned} C_x &= x_0 + X\cos(\varphi) \\ C_y &= y_0 + Y\sin(\varphi+\psi) \end{aligned} \tag{7.29}$$

with

$$\begin{aligned} x_0 &= \frac{A_1 - A_2}{A_1 + A_2} \quad X = \frac{B_1 + B_2}{A_1 + A_2} = \frac{2B_1}{A_1 + A_2} \\ y_0 &= \frac{A_3 - A_4}{A_3 + A_4} \quad Y = \frac{B_3 + B_4}{A_3 + A_4} = \frac{2B_3}{A_3 + A_4} \end{aligned} \tag{7.30}$$

where x_0 and y_0 are the contrast offset in each sector, and X and Y the contrast amplitudes, while ψ is still the quadrature mismatch introduced before. If these five parameters are known, equation 7.29 can be inverted to extract the interferometer response and thus implement the contrast correction process that is a form of Heydemann correction. That is:

$$\begin{aligned} x = \cos(\varphi) &= k_1 C_x + k_2 \\ y = \sin(\varphi) &= k_3 C_x + k_4 C_y + k_5 \end{aligned} \tag{7.31}$$

with

$$\begin{aligned} k_1 &= \frac{1}{X} & k_2 &= -\frac{x_0}{X} \\ k_3 &= -\frac{\tan(\psi)}{X} & k_4 &= \frac{1}{Y\cos(\psi)} \\ k_5 &= \frac{x_0 \tan(\psi)}{X} - \frac{y_0}{Y\cos(\psi)} \end{aligned} \tag{7.32}$$

it is possible to write:

$$e^{\imath\varphi} = \cos(\varphi) + \imath \sin(\varphi) = x + \imath y \tag{7.33}$$

from which the optical phase φ is retrieved:

$$\varphi = arg(x + \imath y) = \arctan\left(\mathcal{Y}/\mathcal{X}\right) \tag{7.34}$$

Then, the microcantilever displacement z can be obtained using equation 7.13:

$$z = \frac{\lambda}{4\pi}\varphi \tag{7.35}$$

The contrast correction process, shown so far, is illustrated in the Figure: the distorted contrast (equation 7.29) take the shape of an ellipse laying in the square tangent to the unit circle, as

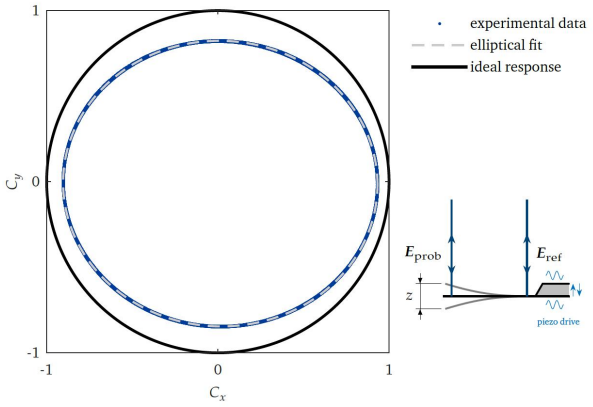

Figure 7.5: An exemple of Heydemann correction applied to the QPDI signal. The thermal noise amplitude of a microcantilever is typically under 1 nm, and is too low to explore the full response range of the interferometer. The cantilever is therefore driven by a piezo element to a deflection amplitude slightly above half the laser wavelength, only during the calibration process.

$-1 \leq C_x,\ C_y \leq 1$. The correction corresponds to a projection of this ellipse on the unit circle.

In practice, the QPDI Heydemann correction is implemented as an offline calibration procedure (Figure 7.5):

- The cantilever is excited close to its first resonant frequency by a piezoelectric ceramic, with a deflection amplitude larger but close to half the laser wavelength. On a plot of the experimental contrast, the dataset then take the form of a closed ellipse, which the 5 ellipse correction parameters are extracted.

- The system response is optimized by tuning the angular position of the interferometer's half wave and quarter wave plates. The contrast is thus settled closer to its ideal unit circle shape.

- After this optimization, the piezo excitation is turned off, and the cantilever can ring down to its thermal noise level of deflection.

The ellipse fit parameters are then used to correct the subsequent thermal noise measurements.

Bibliography

Abbott, R., ... and De Simone, R., *et al.* (LVK Collaboration) (2021), 'GWTC-3: compact binary coalescences observed by LIGO and Virgo during the second part of the third observing run', *arXiv preprint arXiv:2111.03606* .

Abbott, R. *et al.* (LVK Collaboration) (2016), 'Observation of Gravitational Waves from a Binary Black Hole Merger', *Phys. Rev. Lett.* **116**, 061102.

Abbott, R. *et al.* (LVK Collaboration) (2017), 'GW170817: Observation of Gravitational Waves from a Binary Neutron Star Inspiral', *Phys. Rev. Lett.* **119**, 161101.

Abbott, R. *et al.* (LVK Collaboration) (2019), 'GWTC-1: A Gravitational-Wave Transient Catalog of Compact Binary Mergers Observed by LIGO and Virgo during the First and Second Observing Runs', *Phys. Rev. X* **9**, 031040.

Abbott, R. *et al.* (LVK Collaboration) (2021*a*), 'GWTC-2: Compact Binary Coalescences Observed by LIGO and Virgo during the First Half of the Third Observing Run', *Phys. Rev. X* **11**, 021053.

Abbott, R. *et al.* (LVK Collaboration) (2021*b*), 'Population properties of compact objects from the second LIGO–Virgo Gravitational-Wave Transient Catalog', *The Astrophysical journal letters* **913**(1), L7.

Abbott, R. *et al.* (LVK Collaboration) (2021*c*), 'Tests of general relativity with binary black holes from the second LIGO-

Virgo gravitational-wave transient catalog', *Physical review D* **103**(12), 122002.

Abelès (1963), VI Methods for Determining Optical Parameters of Thin Films, Vol. 2 of *Progress in Optics*, Elsevier, pp. 249–288.

Acernese, F. *et al.* (2015*a*), 'Advanced Virgo: A second-generation interferometric gravitational wave detector', *Classical and Quantum Gravity* **32**(2).

Acernese, F. *et al.* (2015*b*), 'Advanced Virgo: a Second-Generation Interferometric Gravitational Wave Detector', *Classical and Quantum Gravity* **32**(2), 024001.

A Gravitational Wave Observatory Operating Beyond the Quantum Shot-Noise Limit (2011), *Nature Physics* **7**(12), 962–965.

Agresti, J. *et al.* (2006), Optimized Multilayer Dielectric Mirror Coatings for Gravitational Wave Interferometers, *in* 'SPIE Optics + Photonics'.

Amato, A. *et al.* (2019), 'Optical Properties of High-Quality Oxide Coating Materials used in Gravitational-Wave Advanced Detectors', *Journal of Physics: Materials* **2**(3), 035004.

Awai, I. & Ikenoue, J. (1984), 'Effect of Film Transition Layers on the Abelès Method', *Applied optics* **23**(11), 1890–1896.

Born, M. & Wolf, E. (2013), *Principles of optics: electromagnetic theory of propagation, interference and diffraction of light*, Elsevier.

Callen, H. B. & Welton, T. A. (1951), 'Irreversibility and Generalized Noise', *Phys. Rev.* **83**, 34–40.

Carniglia, C. K. & Apfel, J. H. (1980), 'Maximum Reflectance of Multilayer Dielectric Mirrors in the Presence of Slight Asorption', *JOSA* **70**(5), 523–534.

Caves, C. M. (1981), 'Quantum-Mechanical Noise in an Interferometer', *Phys. Rev. D* **23**, 1693–1708.

Cervantes-Cota *et al.*, J. L. (2016), 'A Brief History of Gravitational Waves', *Universe* **2**(3).

Chiadini, F., Fiumara, V., Gallina, I. & Scaglione, A. (2009), 'Omnidirectional bandgap in Cantor dielectric multilayers', *Optics Communications* **282**(19), 4009–4013.

Chiadini, F., Fiumara, V., Mackay, T. G., Scaglione, A. & Lakhtakia, A. (2017*a*), 'Temperature-mediated transition from Dyakonov–Tamm surface waves to surface-plasmon-polariton waves', *Journal of Optics* **19**(8). Art. no. 085002.

Chiadini, F., Fiumara, V., Mackay, T., Scaglione, A. & Lakhtakia, A. (2017*b*), 'Signatures of thermal hysteresis in Tamm-wave propagation', *Journal of the Optical Society of America B: Optical Physics* **34**(10), 2155–2160.

Chiadini, F., Fiumara, V., Mackay, T., Scaglione, A. & Lakhtakia, A. (2017*c*), 'Temperature-mediated transition from Dyakonov-Tamm surface waves to surface-plasmon-polariton waves', *Journal of Optics (UK)* **19**(8). Art. no. 085002.

Chiadini, F., Fiumara, V. & Scaglione, A. (2013), 'Synthesis method for N-band multilayer antireflection coatings', *Journal of Nanophotonics* **7**(1). Art. no. 12104.

Chiadini, F. *et al.* (2009), 'Cantor Dielectric Filters in Rectangular Waveguides', *Electromagnetics* **29**(8), 575–585.

Cormier, P. *et al.* (2017), 'Vanadium dioxide as a material to control light polarization in the visible and near infrared', *Optics Communications* **382**, 80–85.

De Simone, R., Chiadini, F., Scaglione, A. & Fiumara, V. (2020), 'Temperature-mediated excitation of defect modes in a periodic structure at terahertz frequencies', *Microwave and Optical Technology Letters* **62**(12), 3677–3681.

Emmerich, M. & Deutz, A. (2018), 'A Tutorial on Multiobjective Optimization: Fundamentals and Evolutionary Methods', *Natural computing* **17**(3), 585–609.

Fazio, M. A. *et al.* (2022), 'Comprehensive study of amorphous metal oxide and Ta_2O_5-based mixed oxide coatings for gravitational-wave detectors', *Phys. Rev. D* **105**, 102008.

Fink, Y. *et al.* (1998), 'A Dielectric Omnidirectional Reflector', *Science* **282**(5394), 1679–1682.

Flanagan, É. É. & Hughes, S. A. (1998), 'Measuring gravitational waves from binary black hole coalescences. i. signal to noise for inspiral, merger, and ringdown', *Physical Review D* **57**(8), 4535.

Gerrard, A. & Burch, J. M. (1994), *Introduction to Matrix Methods in Optics*, Courier Corporation.

Goell, J. & Standley, R. (1972), 'Effect of Refractive Index Gradients on Index Measurement by the Abelès Method', *Applied Optics* **11**(11), 2502–2505.

Grote, H. *at all* (2013), 'First Long-Term Application of Squeezed States of Light in a Gravitational-Wave Observatory', *Phys. Rev. Lett.* **110**, 181101.

Hadka, D. & Reed, P. (2013), 'Borg: An auto-adaptive many-objective evolutionary computing framework', *Evolutionary Computation* **21**(2), 231–259.

Hartley, W. (2017), 'Multi-messenger Observations of a Binary Neutron Star Merger', *The Astrophysical Journal Letters* **848**(2), L12.

Howells, S. C. & Schlie, L. A. (1996), 'Transient terahertz reflection spectroscopy of undoped InSb from 0.1 to 1.1 THz', *Applied Physics Letters* **69**(4), 550–552.

Hughes, S. A. & Thorne, K. S. (1998), 'Seismic gravity-gradient noise in interferometric gravitational-wave detectors', *Phys. Rev. D* **58**, 122002.

Hung, H., Wu, C.-J. & Chang, S.-J. (2011), 'Terahertz temperature-dependent defect mode in a semiconductor-dielectric photonic crystal', *Journal of Applied Physics* **110**(9). Art. no. 093110.

Kana, J.B. *et al.* (2011), 'Thermally tunable optical constants of vanadium dioxide thin films measured by spectroscopic ellipsometry', *Optics Communications* **284**(3), 807–812. Erratum: *Opt. Commun.*, vol. 284, no. 12, p. 3181, 2011.

Karim, F. & Seddiki, O. (2013), 'Analysis of defect layers' insertion effect on optical transmission properties of multilayer structures based on one-dimensional photonic crystals', *Applied Optics* **52**(3), 474–479.

Kimble, H. J. *et al.* (2001), 'Conversion of Conventional Gravitational-Wave Interferometers into Quantum Nondemolition Interferometers by Modifying their Input and/or Output Optics', *Phys. Rev. D* **65**, 022002.

King, T.-C. & Wu, C.-J. (2014), 'Design of Multichannel Filters Based on the Use of Periodic Cantor Dielectric Multilayers', *Applied Optics* **53**(29), 6749–6755.

Koppelmann, G. (1960), 'On the Theory of Multilayers Consisting of Weakly Absorbing Materials and their use as Interferometer Mirrors', *Ann. Phys.(Leipzig)* **7**, 388–396.

Lee, C. *et al.* (2005), 'Effect of Thermal Annealing on the Optical Properties and Residual Stress of TiO_2 FilmsProduced by Ion-AssistedDeposition', *Applied optics* **44**(15), 2996–3000.

LIGO Scientific Collaboration, t. (2015), 'Advanced LIGO', *Classical and Quantum Gravity* **32**(7), 074001.

LIGO website (n.d.), `https://www.ligo.caltech.edu/page/learn-more`. LIGO Laser Interferometer Gravitational-Wave Observatory.

Logofatu, P. *et al.* (2006), 'Abelès Method Revisited', *Applied Optics* **45**(6), 1120–1123.

Logue, J. *et al.* (2012), 'Inferring Core-Collapse Supernova Physics with Gravitational Waves', *Phys. Rev. D* **86**, 044023.

Maggiore, M. (2000), 'Gravitational Wave Experiments and Early Universe Cosmology', *Physics Reports* **331**(6), 283–367.

Magnozzi, M. *et al.* (2018), 'Optical Properties of Amorphous SiO_2-TiO_2 Multi-Nanolayered Coatings for 1064-nm Mirror Technology', *Optical Materials* **75**, 94–101.

Martin *et al.* (1983), 'Ion-Beam-Assisted Deposition of Thin Films', *Applied Optics* **22**(1), 178–184.

Matichard *et al.* (2015), 'Seismic Isolation of Advanced LIGO: Review of strategy, instrumentation and performance', *Classical and Quantum Gravity* **32**(18), 185003.

Nardecchia, I. (2022), 'Detecting Gravitational Waves with Advanced Virgo', *Galaxies* **10**(1).

Oelker, E. *et al.* (2014), 'Squeezed light for advanced gravitational wave detectors and beyond', *Opt. Express* **22**(17), 21106–21121.

Pan, H. *et al.* (2014), 'Thickness-Dependent Crystallization on Thermal Anneal for Titania/Silica nm-Layer Composites Deposited by Ion Beam Sputter Method', *Optics Express* **22**(24), 29847–29854.

Paolino, P., Aguilar Sandoval, F. A. & Bellon, L. (2013), 'Quadrature phase interferometer for high resolution force spectroscopy', *Review of Scientific Instruments* **84**(9), 095001.

Pierro, V. *et al.* (2019), 'On the Performance Limits of Coatings for Gravitational Wave Detectors Made of Alternating Layers of Two Materials', *Optical Materials* **96**, 109269.

Pierro, V. *et al.* (2021), 'Optimal Design of Coatings for Mirrors of Gravitational Wave Detectors: Analytic Turbo Solution via Herpin Equivalent Layers', *Applied Sciences* **11**(24), 11669.

Pierro, V. *et al.* (2021), 'Ternary Quarter Wavelength Coatings for Gravitational Wave Detector Mirrors: Design Optimization via Exhaustive Search', *Physical Review Research* **3**(2), 023172.

Pinard, L. *et al.* (2017), 'Mirrors Used in the LIGO Interferometers for First Detection of Gravitational Waves', *Applied Optics* **56**(4), C11–C15.

Principe, M. (2015), 'Reflective Coating Optimization for Interferometric Detectors of Gravitational Waves', *Opt. Express* **23**(9), 10938–10956.

Qiao, X. *et al.* (2016), 'Progresses on the Theory and Application of Quartz Crystal Microbalance', *Applied Physics Reviews* **3**(3), 031106.

Refractiveindex.info website (n.d.), `https://refractiveindex.info`. Refractive index datbase.

Reid, S. & Martin, I. W. (2016), 'Development of Mirror Coatings for Gravitational Wave Detectors', *Coatings* **6**(4).

Rogalin, V., Kaplunov, I. & Kropotov, G. (2018), 'Optical materials for the THz range', *Optics and Spectroscopy* **125**(6), 1053–1064.

Saulson, P. (1994), *Fundamentals of Interferometric Gravitational Wave Detectors*, World Scientific.

Schönenberger, C. & Alvarado, S. (1989), 'A Differential Interferometer for Force Microscopy', *Review of Scientific Instruments* **60**(10), 3131–3134.

Schubert, M., Poxson, D., Mont, F., Kim, J. & Schubert, E. (2010), 'Performance of antireflection coatings consisting of multiple discrete layers and comparison with continuously graded antireflection coatings', *Applied Physics Express* **3**(8). Art. no. 082502.

Scotognella, F. (2013), 'One-Dimensional Photonic Structure with Multilayer Random Defect', *Optical Materials* **36**(2), 380–383.

Steinlechner, J. (2018), 'Development of mirror coatings for gravitational-wave detectors', *Philosophical Transactions of the Royal Society of London Series A* **376**(2120), 20170282.

Strain, K. t. (1994), 'Thermal Lensing in Recycling Interferometric Gravitational Wave Detectors', *Physics Letters A* **194**(1), 124–132.

Thielsch, R. *et al.* (2002), 'A comparative study of the UV optical and structural properties of SiO_2, Al_2O_3, and HfO_2 single layers deposited by reactive evaporation, ion-assisted deposition and plasma ion-assisted deposition', *Thin Solid Films* **410**(1-2), 86–93.

Tompkins, H. & Irene, E. A. (2005), *Handbook of Ellipsometry*, William Andrew.

VIRGO website (n.d.), `https://www.virgo-gw.eu/science/detector/optical-layout/`.

Wood, B., Pendry, J. & Tsai, D. (2006), 'Directed subwavelength imaging using a layered metal-dielectric system', *Physical Review B* **74**(11), 115116.

Yeh, P. (2005), *Optical Waves in Layered Media*, Wiley, Hoboken, New Jersey.

Zhukovsky, S. V., Lavrinenko, A. V. & Gaponenko, S. V. (2013), Optical Filters Based on Fractal and Aperiodic Multilayers, *in* 'Optics of Aperiodic Structures - Fundamentals and Device Applications', Pan Stanford Publishing Pte. Ltd., pp. 91–142.

Symbols and Abbreviations

A	Absorptance, the ratio of the power absorbed in the structure to the power incident on it.
B	Normalized total tangential electric field at the front interface of an assembly of layers.
C	Normalized total tangential magnetic field at the front interface of an assembly of layers.
d_i	Physical thickness of the ith layer in a thin film coating.
$\boldsymbol{E}$	Electric vector in the electromagnetic field.
$\boldsymbol{\mathcal{E}}$	Total tangential electric field amplitude.
$\boldsymbol{E}_0$	Electric field amplitude.
$\boldsymbol{H}$	Magnetic vector in the electromagnetic field.
$\boldsymbol{\mathcal{H}}$	Total tangential magnetic field amplitude.
$\boldsymbol{H}_0$	Magnetic field amplitude.
H	Represents a layer of high index in shorthand notation.
I	Irradiance of the wave (power per unit area).
k	Extinction coefficient. The imaginary part of the complex refractive index $n - \imath k$.
L	Represents a layer of low index in shorthand notation.
MSE	Mean Square Error.
n	Refractive index. The real part of the complex refractive index $n - \imath k$.

p	p-Polarization, also known as TM for *transverse magnetic*, is the polarization where the electric field direction is in the plane of incidence.
R	Reflectance, the ratio at a boundary of the normal components of reflected and incident irradiance or, alternatively, the ratio of the total reflected beam power to the total incident beam power.
s	s-Polarization, also known as TE for *transverse electric*, is the polarization where the electric field direction is normal to the plane of incidence.
T	Transmittance, the ratio of the normal components of transmitted and incident irradiance or, alternatively, the ratio of the total transmitted beam power to the total incident beam power.
TE	See s for s-polarization.
TM	See p for p-polarization.
x, y, z	Coordinate axes. In the case of a thin film or surface the z-axis is usually taken positive into the surface in the direction of incidence. The x-axis is usually arranged in the plane of incidence and the x-, y-, and z-axes, in that order, make a right-handed set.
y	Characteristic admittance of a material given in SI units (siemens) by $(n - \imath k)Y_0$ and in units of the admittance of free space, Y_0, by $n - \imath k$.
$\mathcal{Y}$	Surface admittance, the ratio of the total tangential components of magnetic and electric field at any surface parallel to the film boundaries.
Y_0	Admittance of free space ($2.6544 \times 10^{-3} S$).
y_0	Characteristic admittance of the incident medium.
y_m	Characteristic admittance of the emergent medium
y_{sub}	Characteristic admittance of the substrate
α	Absorption coefficient, given by $4\pi k/\lambda$ usually in units of cm^{-1}.

α, β, γ	Three direction cosines, that is, the cosines of the angle the direction makes with the three coordinate axes.
β	Symbol for $2\pi kd/\lambda$ usually with reference to a metal.
γ	Equivalent phase thickness of a symmetrical arrangement of layers.
Δ	η_p/η_s where η is the modified tilted admittance. The quantity is used in the design of polarization-free coatings.
δ	Phase thickness of a coating, given by $2\pi(n - \imath k)d/\lambda$.
ε	Permittivity of a medium.
η	Tilted optical admittance.
θ	Angle of incidence.
λ_0	Reference wavelength. The optical thicknesses of the layers in a coating are defined with respect to the reference wavelength that is usually chosen to make the more important layers in the coating as close to quarter-waves as possible.
μ	Permeability.
ρ	Amplitude reflection coefficient. Used also as electric charge density in Maxwell's equation.
τ	Amplitude transmission coefficient.
ϕ	Phase difference, often in reflection or transmission.
ψ	Potential transmittance, $T/(1 - R)$ or the ratio of the quantities $Re(BC^*)$ evaluated at two different interfaces. It represents the power emerging from a system divided by the power entering and is unity if there is no loss.
QWL	Quarter Wavelength design.

Appendix A

Ion-assisted e-beam deposition *(IAD)*

The ion assisted e-beam deposition (IAD) is a physical vapor deposition (PVD) technique that combines the electron beam with an ion source (or plasma), directed on the substrate to assist the deposition process. A beam of ions, typically argon (Ar) ions with a wide range of energies, is directed to the substrate and arrives the material to be deposited during ion assisted e-beam evaporation. These ions provide the atoms that are evaporating energy, increasing their surface mobility. The adhesion, density, and grain structure of the deposited layer can be improved by increasing arrival energy and surface mobility.

These film advancements also result in a more repeatable refractive index for dielectric materials, such as those deposited in optical coating applications. Oxygen and nitrogen ions can be added to the beam while depositing oxides or nitrides, providing a dual "react-assist" process capability as in this case using a mixture gas of oxygen (O2) and argon (Ar).

Use of an end-hall type ion source, which offers uniform substrate coverage and control over the energy and current of the beam, is usual for ion aided e-beam evaporation. The beam must supply an ion-to-atom arrival ratio that fulfills the experimentally calculated dosage for a certain deposition material in order to guarantee a completely "assisted" process. This effectively implies that the ion source must be set up according to the material and rate

of deposition for a particular procedure. The capacity to pre-clean, etch, or oxidize the substrate before deposition is another advantage of an end-hall ion source in an electron beam evaporation system in order to improve the coating adhesion and produce higher molecular packing density during the material evaporation, enhancing the material uniformity and density (Thielsch, R. *et al.* 2002), (Lee, C. *et al.* 2005) as well as the mechanical and optical properties of the films (Martin *et al.* 1983).

The deposition process is described in Figure A.1.

- In A.1a electrons are emitted from a tungsten filament due to the thermionic effect. The generated electron beam is accelerated and permanent magnets bend the trajectory of the beam towards the crucible containing the material to be evaporated (metal oxides, in this case).

- In A.1b the target is heated by means of the electron beam so as to reach the melting temperature of the material to be evaporated. In this way, atoms travel toward the substrate thus creating the desired layer (or coating) on the substrate surface.

- In A.1c the substrate is continuously bombarded with the ion flow.

The coater machine used is shown in Figure A.2. In particular, Figure A.2a shows the outside of the coater, and its pumping system. In general, the pre-vacuum is achieved in the system by a two-stage combination of a rotary vane vacuum pump and an upstream roots pump. The turbo-molecular pump evacuates the vacuum chamber to achieve the high vacuum (Qiao, X. *et al.* 2016). Figure A.2b displays the vacuum chamber of the coater: the carousel (1) that accommodate the substrates rotates above the plumes of the electron and ion sources, being decentered with respect to it, so that the ionbombardment (2) works every time the evaporation adds one or few new atomic layers. A shutter (3), between the evaporation source (4) and the substrates, is open when the deposition starts and is closed when the deposited ends. Moreover, the infrared heater (7) can be used to warm up the

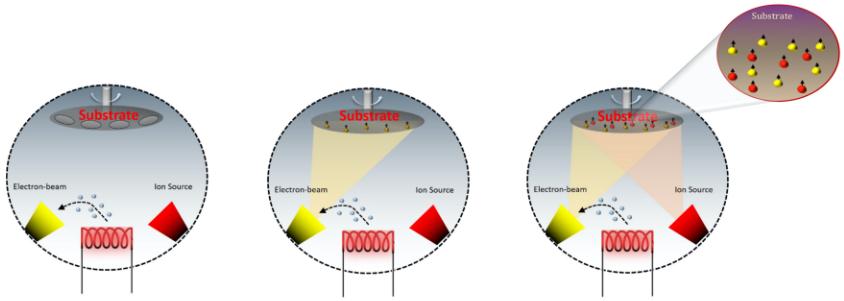

(a) (b) (c)

Figure A.1: The ion-plasma assisted e-beam deposition (IAD) process. (a) Electrons are emitted from a tungsten filament and directed towards the crucible. (b) The target reaches the melting temperature and emitted atoms travel toward the substrate. (c) The ion beam (plasma) bombards the substrate.

substrates (up to 100 °C) and ensures a constant temperature in the vacuum chamber, when required.

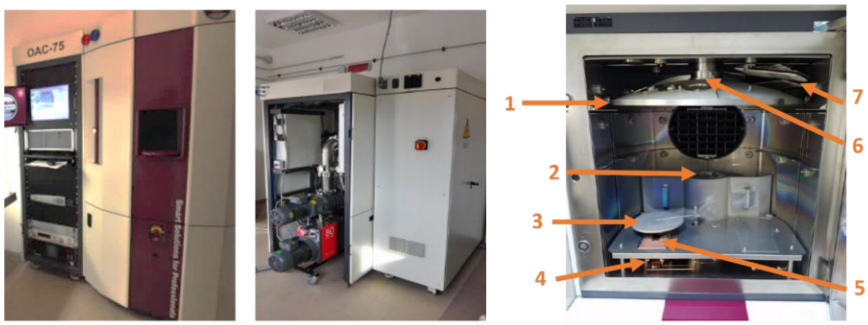

(a) (b)

Figure A.2: OptoTech OAC-75F coater, (a) outside and (b) inside, located at University of Benevento. The main components are: (1) Substrate carousel; (2) Ion gun; (3) Material Shutter; (4) E-gun; (5) Material crucibles; (6) Quartz Crystal Monitor; (7) Infrared Heater.

Appendix B

Multilayers Structure at Terahertz Regime - Temperature Dependent Defect Modes

Multilayer structures are widely used in technical devices operating at optical frequencies (Yeh 2005) for filtering applications (Chiadini, F. *et al.* 2009, Zhukovsky et al. 2013, King & Wu 2014), reflection (Fink, Y. *et al.* 1998, Chiadini et al. 2009, Steinlechner 2018) and antireflection coatings (Schubert et al. 2010, Chiadini et al. 2013).

The most common and simple multilayers are periodic structures made as a cascade of unit cells consisting of two layers with high (n_H) and low (n_L) refractive index, as reported in Figure B.1a.

This structures exhibit stop-bands where transmission of electromagnetic waves is very close to zero, an example of the spectrum is depicted in Figure B.1b. The characteristics of the forbidden bands of propagation depend on the thicknesses and refractive indices of the materials in the unit cell, and on the number of unit cells in the multilayer.

If the periodicity is perturbed by inserting in the stack a "defect layer", Figure B.2a consisting of a material different from the materials constituting the original structure, a defect mode ap-

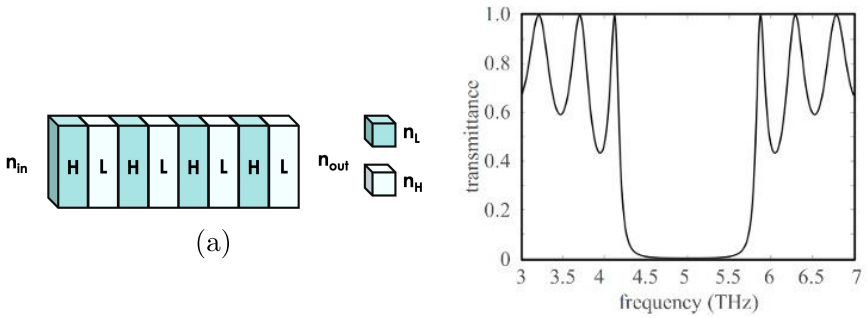

(a) (b)

Figure B.1: Periodic multilayer: (a) schematic, (b) transmittance spectrum as fuction of the frequency.

pears within the forbidden band, as reported in Figure B.2b . The defect mode is a narrowband transmission peak wich properties (center frequency, height and width of the transmission peak) depend on the defect layer characteristics (thickness, refractive index and position in the stack).

Hence, the spectral position of the defect mode depends on the optical length of the defect layer (Karim & Seddiki 2013, Scotognella 2013). Then, the defect mode center frequency can be controlled by changing the optical length of the defect layer.

As a consequence, materials exhibiting refractive index significantly depending on temperature can be used as defect layers in order to obtain temperature-dependent defect modes. Examples of this kind of materials are Vanadium Dioxide (VO_2) and Indium Antimonide (InSb) which exhibit refractive index strongly dependent on temperature in the optical and terahertz regime, respectively (Cormier, P. *et al.* 2017, Kana, J.B. *et al.* 2011, Chiadini et al. 2017*b*,*c*, Howells & Schlie 1996).

The multilayer structures made of the materials that have strong dispersion at terahertz have some critical issues including the difficulty of depositing layers with thicknesses appropriate to this frequencies, lack of knowledge of the physical characteristics of materials such as the refractive index and the extinction coefficient, and the need to have negligible absorption. Among the materials with a known law of dispersion and negligible ab-

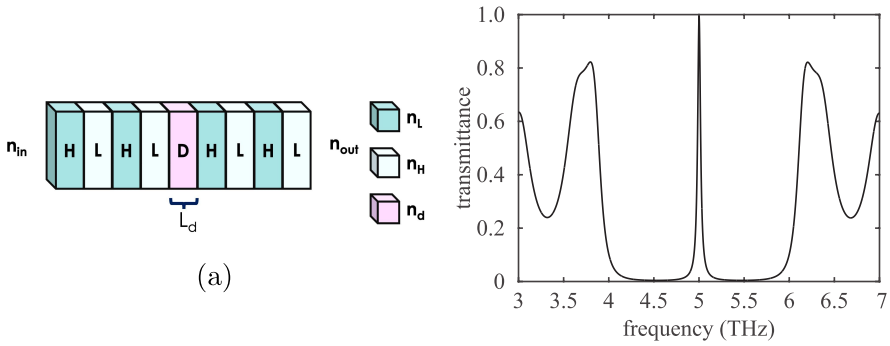

Figure B.2: Periodic multilayer with a perturbed structure: (a) schematic, (b) transmittance spectrum as fuction of the frequency.

sorption at terahertz can be counted the crystalline quartz (silica, SiO_2) (Hung et al. 2011) and some polymers that show excellent transparency at terahertz. In particular, polymethylpentene TPX (more precisely, poly-4-methylpentene-1) is a semi-crystalline polymer with negligible absorptance and with a refractive index which is practically constant in the range $[3, 7]$ THz. (Rogalin et al. 2018) In addition, the TPX refractive index is particularly low (≈ 1.5) making it suitable for use in multilayers as the low refraction index medium.

In Ref. (De Simone et al. 2020) it has been analyzed a multilayer of SiO_2/TPX with a defect consisting of a layer of indium antimonide ($InSb$). Let us consider a periodic multilayer consisting of M unit cells. The unit cell is constituted by two layers of the two different materials, SiO_2/TPX. The whole structure $(SiO_2/\text{TPX})^M$ sits between two half-spaces occupied by air, where it has been denoted $(SiO_2/\text{TPX})^M$ as the cascade of M cells of SiO_2/TPX. A layer of $InSb$is inserted after N unit cells. Thus, the entire structure can be represented as $(SiO_2/\text{TPX})^N$ $/InSb/$ $(SiO_2/\text{TPX})^{M-N}$. A schematic of the multilayer geometry is provided in Figure B.3. A monochromatic electromagnetic plane wave impinges normally on the multilayer from the uppermost half-space. The reflectance and transmittance can be calculated using the conventional characteristic matrix method 2.6. Materials constituting the unit cell can be assumed lossless and

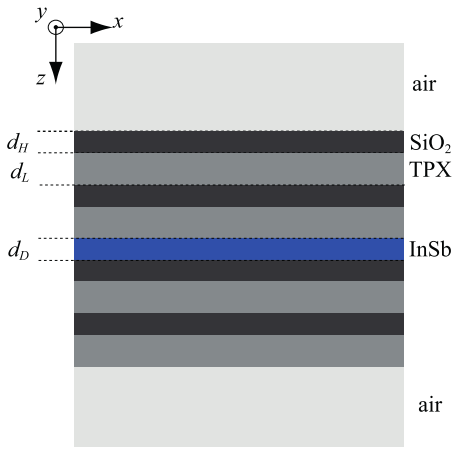

Figure B.3: Schematic of the analyzed structure: $(SiO_2/\text{TPX})^N$ $/InSb/$ $(SiO_2/\text{TPX})^{M-N}$

the dispersion can be neglected in the considered frequency band, so the refractive indexes are $n_H = 2.25$ (SiO_2) (Hung et al. 2011) and $n_L = 1.46$ (TPX) (Rogalin et al. 2018). In order to have the defect mode at the center of the forbidden band, all $SiO_2$and TPX layers have the same optical thickness, that is, a quarter of the (vacuum) wavelength $\lambda_0 = 59.96$ μm, corresponding to the frequency $f_0 = 5$ THz, viz,

$$\delta = n_H d_H = n_L d_L = \frac{\lambda_0}{4},$$

By means of the equation above, the thicknesses are $d_H = 6.66$ μm and $d_L = 10.27$ μm.

The defect layer is made of $InSb$, whose relative permittivity in the terahertz regime is given by the Drude model (Chiadini et al. 2017*a*).

In Figure B.4a and Figure B.4b, the real and imaginary parts of the relative permittivity, $Re(\varepsilon D)$ and $Im(\varepsilon D)$, respectively, are displayed as functions of both temperature $T[-100, 100]$°C and frequency $f = 2\pi\omega[3, 7]$ THz.

As a result, $n_D = 1.99$ which provides a thickness of the defect $d_D = 3.79$ μm. The multilayer is made of M = 9 unit cells and the defect has been placed right after N = 3 unit cells.

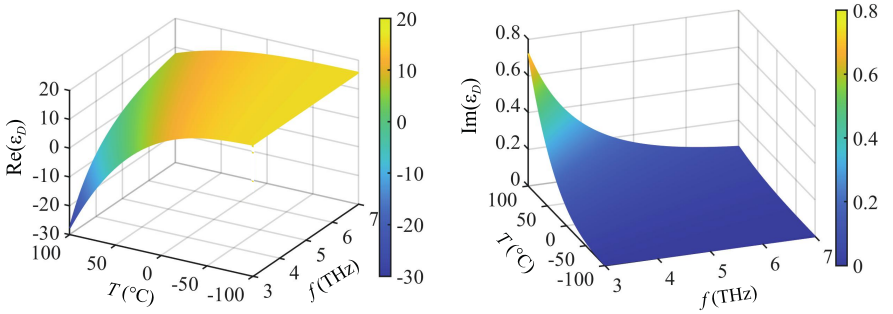

(a) (b)

Figure B.4: Permittivity of indium antimonide (InSb): (a) Real part $Re(\varepsilon D)$, (b) Imagimary part $Im(\varepsilon D)$.

Figure B.5 shows the transmittance for normal incidence as a function of both frequency and temperature. At $T = -100$°C, the defect mode clearly appears in the center of the forbidden band as it was designed. This can be seen in more detail in Figure B.6, where the transmittance is plotted for $T = -100$°C. Figure B.5 shows that the spectral position of the defect mode is very slightly affected by temperature changes when $T \in [-100, 0]$°C while shows greater sensitivity to temperature for $T > 0$.

This is highlighted in Figure B.7a where the spectral position of the defect mode is shown as a function of temperature (solid black curve). The defect mode shifts from a frequency of $5.00THz(T = -100)$°C up to $5.55THz(T = 100$°C).

The shift of the defect mode toward higher frequencies as the temperature rises is not the only effect because a lowering of peak transmittance is also observed. To illustrate this to a greater extent, Figure B.7b shows the maximum transmittance Tp of the defect mode (peak transmittance) as a function of the temperature.

It can be observed that Tp decreases considerably with high temperatures spanning from a maximum of 0.9929 when $T = -100$°C to a minimum of 0.5518 when $T = 100$°C making the defect mode barely excitable.

This behavior can be explained in terms of the variations of $Re(\varepsilon_D)$ and $Im(\varepsilon_D)$ with the temperature. As can be seen in

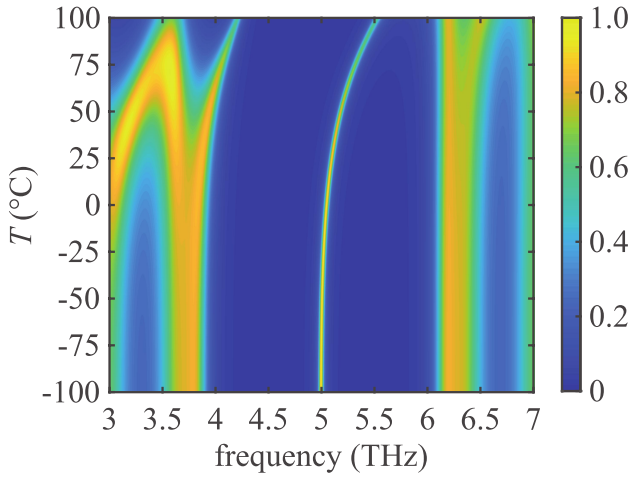

Figure B.5: Transmittance spectrum of the multilayer as a function of the frequency and of the temperature for a normal incident planewave when $d_D = 3.79\ \mu m$.

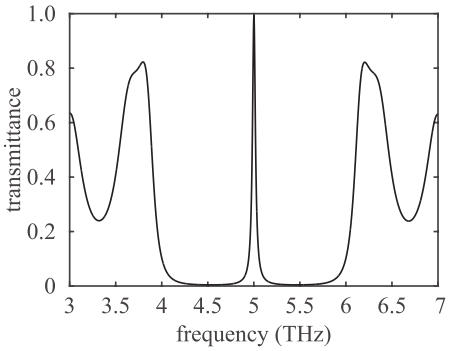

Figure B.6: Transmittance at the temperature $T = -100$°C for a multilayer structure with $d_D = 3.79\ \mu m$. The value of nD at the frequency of the defect mode peak is $n_D = 1.99$

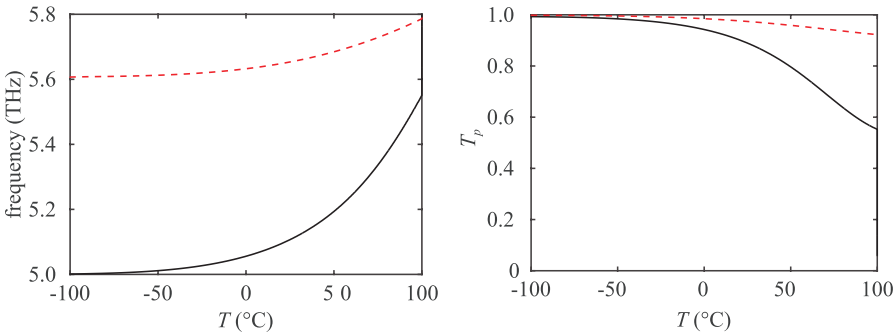

(a) Spectral position of the defect mode as a function of the temperature.

(b) Maximum transmittance Tp of defect mode as a function of the temperature.

Figure B.7: Solid black line: defect layer with physical thickness $d_D = 3.79\ \mu m$. Red dashed line: defect layer with physical thickness $d_D = 1.0\ \mu m$

Figure B.4a, $Re(\varepsilon_D)$ is almost constant with the temperature for $T < 0$ while significantly decreases with temperature for $T > 0$ leading to a decrease of the optical length. As it has been already observed at optical frequencies,33 this causes the blueshift observed in Figure B.5.

On the other hand, $Im(\varepsilon_D)$ increases with temperature for $T > 0$, causing the lowering of the peak transmittance. Since the decrement of T_p at high temperatures is basically due to the power dissipation in the defect, in order to reduce this effect, it was optimized its thickness getting it thinner and thinner with the goal to keep T_p the highest possible and the constraint that the spectral position of the defect mode would always be within the forbidden band. To this end the optimization procedure searches (by inspection) for the thickness of the defect maximizing the area subtended by the maximum transmittance curve as a function of the temperature. The optimal value resulted to be $d_D = 1.00\ \mu m$.

The result of this optimization can be seen from the red dotted curves, relative to the structure with $d_D = 1.00\ \mu m$, depicted in Figure B.7. Compared with the solid black curves plotted in the same figures, obtained in the case in which the defect had thickness $d_D = 3.79\ \mu m$, it can be deduced that:

- varying the temperature the defect mode shifts of a smaller range of frequencies ($\sim$ 160 MHz) going indeed from 5.63 to 5.79 GHz;
- the transmittance of the peak of the defect mode is noticeably above the T_p values of nonoptimized case.

In fact, it has a minimum value of 0.9298 (at $T = 100$°C), and a maximum value that is as high as 0.9984 (at $T = -100$°C).